EXPERIMENTAL STUDY OF SCATTERING IN ATOM-SURFACE COLLISIONS WITH ATOM ENERGIES OF THE ORDER OF 1 ev.

Jack Alcalay

Report No. 67-20

June, 1967

EXPERIMENTAL STUDY OF SCATTERING IN ATOM-SURFACE
COLLISIONS WITH ATOM ENERGIES OF THE ORDER OF 1 EV

Jack Alcalay

Department of Engineering
University of California
Los Angeles, California

1967

FOREWORD

TABLE OF CONTENTS

LIST OF SYMBOLS

A	maximum area of beam admitted by slit at any time
A_b	beam cross-sectional area
A_{do}	cross-sectional area of detector orifice
A(t)	instantaneous value of beam area admitted by chopper slit at time t. Gate function
a_n^j	series expansion coefficients (see Equations A3.6 and A3.7)
C_n	normalization factor of $F_n(s)$ (see Equation 3.14)
d	diameter (subscripts provide specific meaning)
$F_n(s)$	non-normalized speed distribution (Equation A1.1)
$f_n(s)$	normalized speed distribution (Equation A1.2)
$f(\vec{v})$	velocity distribution function
g	linear operator (see Appendix B)
g(t)	time-domain representation of g. Characteristic function of dynamic process.
g(p)	complex (Laplace) plane representation of g
I^-	current of ionizing electrons
$I^+(t)$	instantaneous value of ion current
J(s)ds	flux of molecules with speed ratios in range (s, s+ds)
J(t)	instantaneous flux of molecules
$J(t, \vec{r})$	instantaneous flux of molecules at $\vec{r}$.
k	constant
k	Coltzmann's constant

v

K	through-flow ionization detector sensitivity (defined by Equation 4.6)
K_1	defined by Equation (4.9)
L	length (subscripts provide specific meaning)
ℓ	mean path travelled by ionizing electrons
L{ }	Laplace transform operator
m	mass of atom or molecule
n	density of molecules
n(t)	instantaneous density
$n(t, \vec{r})$	instantaneous density at $\vec{r}$
N	number of atoms or molecules
dN(t)/dt	instantaneous value of molecular flow rate
dN(t)/dx	instantaneous value of gradient of number of atoms along flight path
p	Laplace transform (complex plane) variable
r	defined in Table 3.1; also radius vector with polar coordinates R, θ, ϕ
R	radial coordinate
s	speed ratio ($=u/\gamma$)
S	hydrodynamic speed ratio ($=U/\gamma$)
t	time
T	temperature; also open time of chopper (see Equation 3.28)

LIST OF SYMBOLS (Cont.)

Δt_{tr}	time interval between triggering signal and t=0 (see Equation 4.32b)
u	molecular speed
U	hydrodynamic molecular speed
$\bar{U}$	molecular speed (defined by Equation 3.36)
$\vec{v}$	velocity vector
V	volume
V(t)	instantaneous signal potential
x	linear dimension
X	vector describing flow field

Greek Letters

$\overset{\circ}{\alpha}$	chopper slit open angle
γ	most probable random speed
$\delta(t)$	impulsive (Dirac) function
$\overset{\circ}{\epsilon}$	see Table 4.2 for definition
$\mu\{\ \}$	j'th moment operator (Equation A2.3)
$\eta\{\ \}$	j'th normalized-moment operator (Equation A2.4)
$\nu\{\ \}$	j'th central-moment operator (Equation A2.5)
λ	time
π	pi (transcendental constant)
$\rho(t)$	time-domain analogue of speed distribution (Equation 3.6)
ϕ	time-domain analogue of flux distribution (Equation 3.7)

ϕ	polar angle
Φ	defined by Equation (A4.6)
ξ	defined by Equation (A3.6)
ψ	defined by Equation (A4.6)
$\overset{o}{\psi}$	angle traversed by radial line on chopper across detector orifice
τ	characteristic time
σ	total effective ionization cross section
ϵ	arbitrary small number
Δ	difference operator
$\Delta\eta_1$	defined by Equation (5.5)
$\Delta\nu_2$	defined by Equation (5.6)
η	specular angle less the angle of the maximum of the quasi-specular lobe
$\Theta(S)$	defined by Equation (3.24)
$\kappa(t)$	unit step function (Equation 3.35)
$\Omega(S)$	defined by Equation (3.26)
ω	chopper angular speed
θ	colatitude angle

Subscripts

b	beam
c	capacitance

LIST OF SYMBOLS (Cont.)

cd	chopper to detector
d	detector
des	desorption
e	effusive
i	incident; also integer in recursion formulas
j, k	integers in recursion formulas
L	load resistor
m	modulation
n	refers to power n of speed in $F_n(s)$
ntrf	non-through-flow
od	source orifice to detector
r	recording
s	signal processing; also source
sc	scattering
surf	surface
so	source orifice
tf	time-of-flight
trf	through-flow

LIST OF FIGURES

LIST OF TABLES

ACKNOWLEDGMENT

ABSTRACT

Scattering of modulated Argon atomic beams (with energies of the order of 1 ev and hydrodynamic speed ratios of the order of 7) from cleaved mica and from vacuum-deposited silver on cleaved mica consistently showed a multilobular pattern on a polar flux diagram. The scattering distributions are believed to be the first measured for beams with energies between 1 and 10 ev. Parameters varied during the experiments were (a) surface temperature and (b) time from deposition. The observed quasi-specular lobe bear a close resemblance to the distribution observed by other investigators who have scattered thermal energy beams from various surfaces and behave in some respects as predicted by one simplified collision model. Analyses of the data indicate that the detected molecules may have consisted of both scattered Argon atoms and flash desorbed unknown species from the surface. This suggestion might be tested by mass-spectrometric differentiation of the scattered molecules.

In addition to the aforementioned results, contributions in experimental and analytical techniques to scattering measurements are included. Basic concepts from the theory of linear operators

are used to derive analytical relations between the TOF (time-of-flight) signals, the time-domain analogue of the steady-state beam speed distribution function and a gate function characterizing the modulation process. Sums and products of dynamic operators represent the sequence of dynamic perturbations imposed upon a molecular beam in the course of a scattering experiment. Central moment expansions of these sums and products in the time-domain provide a powerful simple and physically meaningful framework for determining the densities and the pertinent parameters of speed distribution functions of the incident and scattered flow fields. These concepts are applied also to a novel classification and characterization of ionization detectors (based on their dynamic effect in an experiment). A novel concept of calibration is developed and applied to the design, characterization and use of an Orbitron type detector.

CHAPTER I

INTRODUCTION

The study described here represents another application of supersonic molecular beams at the UCLA Molecular-Beam Laboratory and the first phase of a continuing study of interactions of neutral-particle beams with solid surfaces. The intermediate-energy arc-heated supersonic beam developed in this laboratory (References 23, 24) facilitates investigations of the dynamic process occurring at the surface in an energy range not investigated previously.

The purpose of neutral particle-surface collision studies varies depending on the interest and viewpoint of the investigator. The gas dynamicist focuses his attention on the change in the velocity distribution function of a gaseous flow field caused by the presence of a condensed phase. From this point of view, the particle-surface interaction problem is reduced to the definition of the boundary conditions for the equations characterizing the gas-phase flow field.

The chemical physicist (or physical chemist, depending on which permutation is currently in vogue) is interested primarily in the surface as a perturbing field environment for interesting interactions between the electron-orbital fields of different species. His investigations center around the perturbation operator of the surface and its effect on the interaction of the species.

The solid-state physicist sits on the other side of the fence from the gas dynamicist. He views the surface as an interface at which lattice disturbances most often originate. His problem is to relate the perturbation at the surface to its effects on the lattice.

This classical division of emphasis still was pronounced in 1963 when the work reported here was initiated. Since then, investigators have focused more on the alternative views of the same problem. This was evident in December of 1966 at the "interdisciplinary" Symposium on Fundamentals of Gas-Surface Interactions held in San Diego (GR IX), which appropriately had sessions on a) the surface and its characteristics, b) adsorption and reaction of gases on or with surfaces, and c) scattering processes, including energy and momentum transfer.

The gas dynamicist is concerned more and more with lattice dynamics and its effects on the interaction of the surface with the flow field. This concern has paralleled the increased interest in high-speed flows relative to the surfaces of space vehicles and satellites. The surface can be viewed no longer as a) an elastic reflector of particles, or b) a temporary reservoir from which incident particles are reemitted with energies and momenta bearing no correlation with their initial state. This evolution of outlook is displayed in the contents and cited references of the proceedings of successive symposia on Rarefied Gas Dynamics (GR I-V).

Physical chemists are realizing that a kinetic temperature derived from equilibrium velocity distribution functions does not describe adequately the complete range of energy and momentum transport phenomena at the surface. Particle-surface interactions often involve non-equilibrium excitations and the measured responses then cannot be described in terms of equilibrium approximations.

A recent review of atomic processes at solid surfaces (Reference 7) gives increased attention to the modern experimental techniques and results from scattering experiments with molecular beams. It is disconcerting, however, to find statements which relate

a characteristic time of the energy transport to a so-called thermo-
dynamic requirement that the velocity distribution of scattered
particles be Maxwellian and obey the cosine law. As early as 1936,
Eucken[8] related a thermal accommodation coefficient, based on a
very simplified model, to two relaxation times: one reflecting a
first-order energy-transfer model and the other corresponding to a
first-order desorption model. Today it is accepted generally that
single thermal and tangential and normal momentum accommodation
coefficients describe inadequately particle-surface transport
phenomena.

Recent quantitative models of the collision process consider the
induced motion of the lattice atoms within a classical-mechanics
context.[3, 4, 10-16, 26-28, 30, 31, 37-39, 43] The gas-surface inter-
atomic potentials and the potential fields characterizing the lattice
are coupled in these models. Serious mathematical complications
have motivated a large number of simplifying assumptions, some of
which may be serious. Furthermore, even for some of the more
successful models, parameters describing the interatomic potentials
and the lattice potential fields are fitted to experimental results. The
most recent review of the current state of theoretical developments
is given in Reference 38.

The fact that more experimental work is required to provide
the data upon which a successful theoretical structure can be built is
accepted generally. Scattering experiments of molecular beams
from engineering surfaces were first performed by Hurlbut and
co-workers.[20] Paralleling this effort, experiments designed to
measure the energy accommodation coefficients, under conditions
approaching equilibrium, were being perfected in various labora-
tories.[40] Recent particle-surface scattering experiments, using

molecular beams have been described mainly in papers presented at the Rarefied Gas Dynamics Symposia (GR I- GR V).

Some experiments[17-19] have provided valuable guidelines and verification of predictions by a simplified scattering model[26,27,37] based on the assumption that the tangential momentum is conserved during the scattering process. Others[33-36] have been meticulously concerned with the definition of the surface in the gas-surface interaction. One of the most difficult outstanding problems in meaningful experimental programs is the definite characterization of the surface, requiring a) control and measurement of the laboratory-created vacuum environment and b) creation of well-defined crystallographic surface structures. The vacuum deposition of silver on cleaved mica, used in many of the experiments reported here, is inspired by publications of and private communications from Smith and Saltsburg.[33-36] Other experiments valuable in this respect are reviewed in Reference 32.

Even though the status of development of intense molecular beams[9,22-25] shows great progress, the scattering results reported here are the first obtained from a modulated beam in the difficult energy range of 1-10 ev. Extensions to higher intensities, other energies, and other molecular species will advance the frontier of collision and reactive kinetic measurements.

The scope of the experiments reported here is limited to the measurement of flux distributions of the scattered molecular flow field when a 1-ev supersonic argon beam impinges on various surfaces. In the following chapters, the experimental methods and results are described with emphasis on the dynamics of the incident and scattered molecular flow fields.

The modulation and time-of-flight methods are examined in this light in Chapter III. Important within this context are the relationships (developed in Appendices A through C) between the moments of a class of speed distribution functions and those of their time-domain analogues.

Chapter IV examines the detection process. The design and operation of a new type of ionization detector developed specially for these experiments is described. A novel dynamic calibration concept is applied in characterizing the role of the detector in the experiment.

The scattering results presented in Chapter V are of a surprising and unexpected nature. Flash desorption of adsorbed layers by the incident beam may have been important.

Finally Chapter VI summarizes the conclusions and outlines recommendations for future studies which might provide, among other things, an answer to some of the many questions engendered by the results reported here.

CHAPTER II

EXPERIMENTAL TECHNIQUE

Introduction

Consider the following experiment designed to characterize the scattering of a well-defined neutral-particle beam from a surface.

A beam of particles is generated and collimated so that it approaches a state of space coherence associated ideally with a single ray. The beam is chopped in order to determine its density and speed distribution by time-of-flight spectroscopy. The speed distribution is resolved in the time domain by measuring the instantaneous rate at which molecules cross a plane placed at a fixed distance from the chopper. The resolving power is determined by the chopper gate function, the flight length and the speed distribution. The instantaneous density (or the related instantaneous flux) is sensed by a detector, completing the experimental characterization of the incident beam.

Two alternative methods exist for characterizing the scattered flow field. In the first, a modulated beam strikes the scattering surface. In the second, a steady-state beam (whose velocity distribution and density are known from earlier measurements) continuously impinges on the surface, and the scattered molecular flow is modulated and resolved by time-of-flight methods.

In either case, the instantaneous density is measured sequentially in well-defined differential volumes in the unsteady scattered-beam field. In the case when the scattered-particle field is modulated, the time dependence of these densities is determined uniquely by the time-of-flight process. Then this series of time-dependent density measurements, in a tight mesh of differential

volumes, constitutes a complete characterization of the scattered-particle field.

In the case when the incident field is modulated, the measurement of the time-dependent scattered pulse also reflects the dynamics of the processes occurring at the surface. If the characteristic times of these processes are much smaller than the times of flight, they can be neglected. In either case, the described sequential characterization of the incident beam and the scattered particles defines an operator g_{sc} which describes the scattering processes at the surface.

Figure 2.1 is a signal-flow representation of the series of operations on a molecular flow field in a scattering experiment. Modulation, time-of-flight, and detection are introduced in order to characterize the incident and scattered molecular flow fields. Scattering at the surface is the perturbation to be determined by the experiment. The perturbation operator g_{sc}, which characterizes the interaction at the surface, is defined by the following operator equation:

$$X_{out} \doteq g_{sc} X_{in} \tag{2.1}$$

which is read in the usual operator fashion: "The field vector X_{out} (describing the scattered molecular flow field) is obtained when the incident field vector X_{in} (describing the incident molecular flow field) is acted upon by (left-multiplied by) the operator g_{sc} (describing the surface interactions)".

Vectors describing molecular flow fields are characterized by a velocity distribution function and the density at any given point in space. The velocity distribution and the density determine the number and energy fluxes at a given point. Both the velocity distribution function and the density can be intrinsically time-dependent.

PRODUCTION OF INCIDENT BEAM   CHARACTERIZATION OF INCIDENT BEAM

GENERATION — COLLIMATION ⚠1 ⚠2 MODULATION ⚠3 TIME OF FLIGHT ⚠4 DETECTION

POSITIONING OF DETECTOR

θ
ϕ

SURFACE SCATTERING ⚠5 TIME OF FLIGHT ⚠6 DETECTION $I^+(t, R_a, \theta, \phi)$ ⚠7

CHARACTERIZATION OF SCATTERED BEAM

POSITIONING OF DETECTOR

θ
ϕ

SURFACE SCATTERING ⚠8 MODULATION ⚠9 TIME OF FLIGHT ⚠10 DETECTION $I^+(t, R_b, \theta, \phi)$ ⚠11
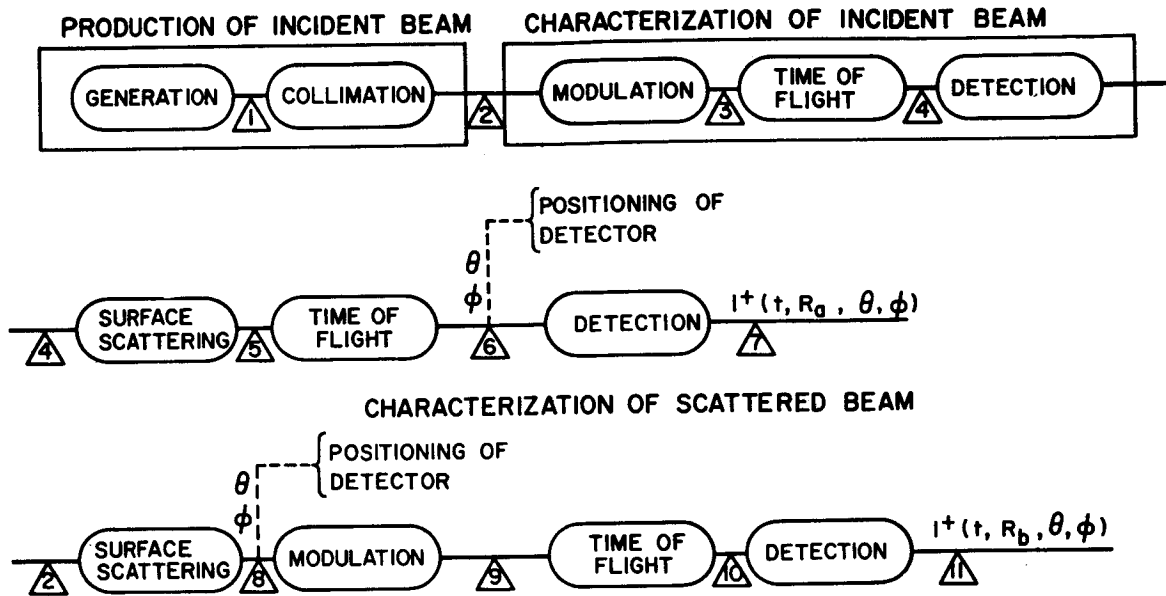
ALTERNATIVE TO CHARACTERIZATION OF SCATTERED BEAM

SIGNAL-FLOW REPRESENTATION OF A MOLECULE-SURFACE SCATTERING EXPERIMENT

FIGURE 2.1

SIGNAL	FIELD VECTOR	FUNCTIONS AND PARAMETERS CHARACTERIZING THE OPERATOR $g_{(\ )}$
1		
2	X_2	
3	$X_3 = g_{1m}X_2$	$A_1(t) \doteq$ Modulator admittance (gate) function
4	$X_4 = g_{1tf}X_3$	$L_1 \doteq$ Flight distance from modulator to surface
		$f(u) =$ Speed distribution of collimated beam

ALTERNATIVE (a): Incident-Beam Modulation

5	$X_5 = g_{sca}X_4$	Unknown (object of investigation); probably surface temperature, structure, and composition and lattice dynamics.
6	$X_6 = g_{2tfa}X_5$	$R_a \doteq$ Radial coordinate of r_a in spherical coordinate system describing flight distance
		$F_{sc}(R_a, \theta, \phi, t) \doteq$ Time-dependent distribution of velocity magnitude @ $\vec{r}_a(R_a, \theta, \phi)$
7	$X_7 = g_d X_6$	Detector design parameters

ALTERNATIVE (b): Scattered-Beam Modulation

8	$X_8 = g_{scb}X_2$	Unknown (object of investigation)
9	$X_9 = g_{2m}X_8$	$A_2(t) \doteq$ Modulator admittance (gate) function
10	$X_{10} = g_{tfb}X_9$	$R_b =$ Radial coordinate of r_b in spherical coordinate system describing flight distance
		$F_{sc}(R_b, \theta, \phi, t) =$ Time-dependent distribution of velocity magnitude @ $\vec{r}_b(R_b, \theta, \phi)$
11	$X_{11} = g_d X_{10}$	Detector design parameters.

Transient molecular fields are often created by modulation of steady-state fields at well-defined points in space. In the experiments described here, the incident beam is modulated. One single detector can be positioned sequentially to detect first the incident beam and then the scattered molecules (at selected values of spatial coordinates).

The ion current (I^+) corresponding to the scattered beam pulse measured at pre-selected coordinates can be expressed in terms of the pulsed incident beam (X_4):

$$I^+(t, R_a, \theta, \phi) = g_d \, g_{2tf} \, g_{sc} \, X_4 \tag{2.2}$$

where

$$X_4 = g_{1tf} \, g_{1m} \, X_4 \tag{2.3}$$

The symbols are defined in Figure 2.1. Equation (2.3) relates the pulsed incident beam (X_4) to the steady-state beam (X_2). The time-of-flight operator g_{tf} depends on the speed distribution of the incident beam. It is therefore nonlinear and does not commute with other operators. Hence, chopping the scattered beam instead of the incident beam, while keeping the total flight distance constant, does not yield the same current signal (I^+).

By the same token, g_{sc}, which describes the interaction with the surface, also may be nonlinear. It may depend on the time characteristics of the incident pulse. If that were the case, g_{sc} obtained from a steady-state-beam excitation would differ (in certain frequency ranges) from that obtained from a modulated-beam excitation.

This operator also may depend upon the parameters characterizing the steady-state speed distribution of the incident beam. For instance, g_{sc} determined from experiments in which the incident

molecules are from a gas phase in equilibrium with the surface might differ from that obtained when supersonic beams excite the surface, even if the total mean energy in both fields are the same.

Apparatus

The arc-heated supersonic molecular-beam apparatus (Figure 2.2) used in these experiments was essentially the same as described in References 23 and 24, which report the activity at the UCLA Molecular-Beam Laboratory and discuss the performance of this apparatus. A summarized description of the equipment follows.

The vacuum system resembles the majority of supersonic molecular beam vacuum systems in that it is divided into three chambers, a source chamber, a collimating chamber and a detection chamber. Since the maximum allowable pressure for the three chambers differ significantly from each other, three different pumping systems were used.

The supersonic jet is produced by expanding, with pressure ratios of the order of 10^4 to 10^5, the beam gas from a stagnation chamber (located in the movable holder) through a source orifice into the source chamber. Beam energies of the order of 1 ev are realized as a consequence of heating the beam gas in the electric arc and then converting the energy of thermal motion into energy of directed motion in the jet. High beam intensities are realized as a consequence of converting the thermal motion into directed motion in the jet. At the operating conditions used to date, it is believed that the beam-gas contamination (due to electrode erosion) is small. For typical operating conditions, the fraction of the excited atoms and ions was found to be $(3.86 \pm 0.58) \times 10^{-4}$ and $(1.16 \pm 0.66) \times 10^{-6}$ respectively (Reference 42). Their effect upon the results reported here should be negligible.

THROUGH-FLOW IONIZATION DETECTOR

TARGET

CHOPPER AND FILTER

10-INCH DIFFUSION PUMP

AIR TURBINE

ORIFICE

ORIFICE

ORIFICE

10-INCH DIFFUSION PUMP

16-INCH DIFFUSION PUMP

NOZZLE LOCATION

MOVABLE HOLDER FOR SOURCE
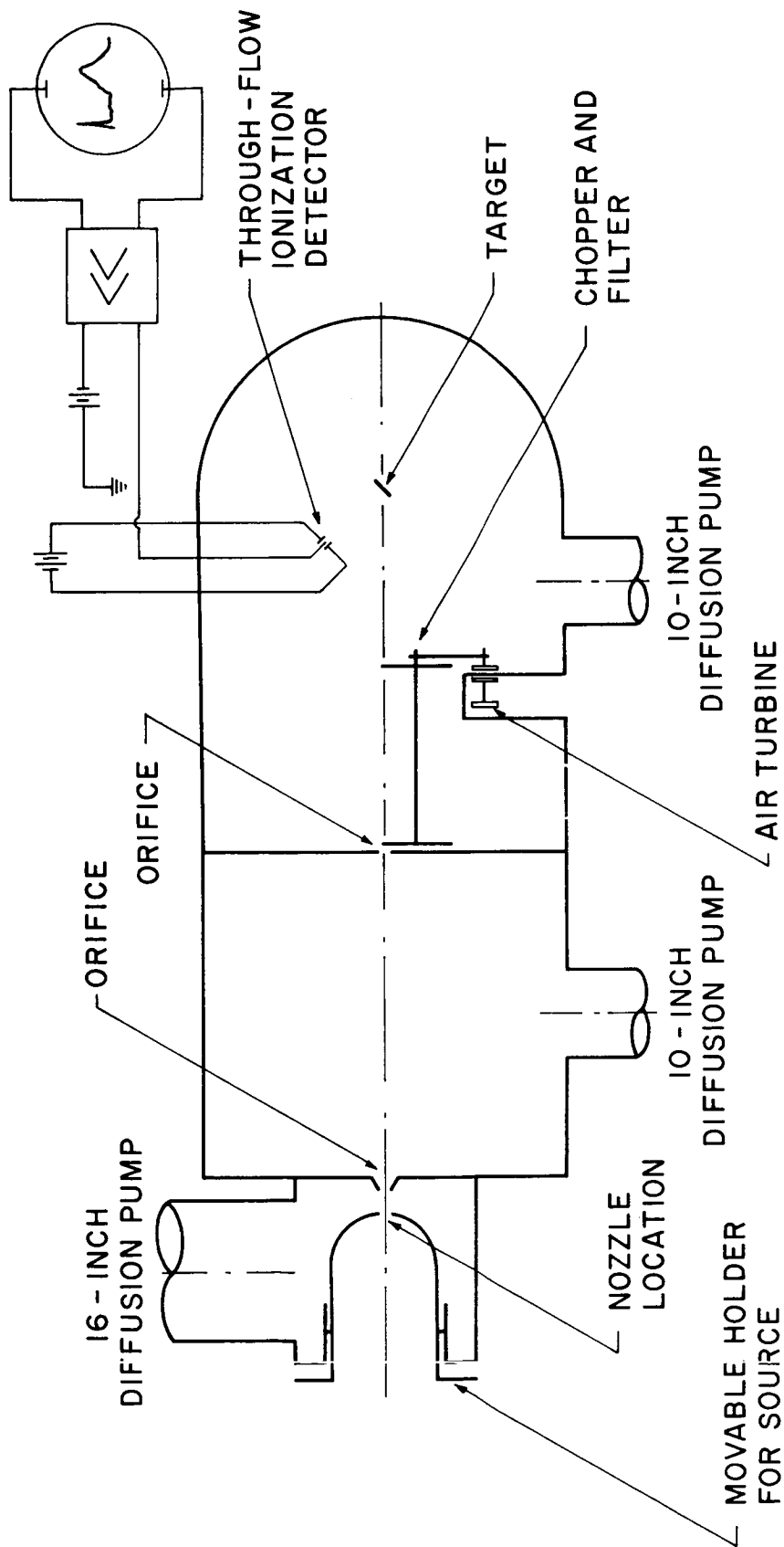
SCHEMATIC DIAGRAM OF UCLA SUPERSONIC MOLECULAR-BEAM APPARATUS

FIGURE 2.2

The beam is collimated by two circular orifices, the first orifice located in a conical skimmer placed in the free jet and the second orifice located in the wall separating the collimating and detection chambers. The predicted beam diameter (at half intensity) is about 1.25 cm. at the target location used in these tests. Maximum beam intensity is realized (for the pumping systems used presently) at the skimmer particle-flow rate for which the beam is attenuated by a factor of $1/e$ in the collimating chamber.

The speed distribution of the incident beam is measured using a single-disk beam chopper, located in the collimating chamber. The time-of-flight pulse was analyzed by methods described in Chapter III. A description of the chopper and its characteristics is given in References 23 and 24. Orbitron-type detectors were designed and used in sensing the time-of-flight signals of both the incident beam and the scattered atoms. The principle of detection and the design and calibration of the Orbitron detector are described in full in Chapter IV.

The detector positioning device is shown in Figure 2.3. It is, with minor modifications, the same as described in Reference 3a. The modifications include the addition of solenoid-operated brakes which prevent movement of the detector during measurements.

Within the framework of the signal-flow diagram of Figure 2.1, the detector positioning device selects the space coordinates at which the transient pulse characterizing the magnitude of the velocity vector is sensed. The solid angle monitored by the detector at any selected position is determined by the area of the detector inlet orifice and the distance R. It is therefore a constant for any series of experiments. This implies that the ion-current pulse measured at a given setting is equal to the ion-current pulse which would be
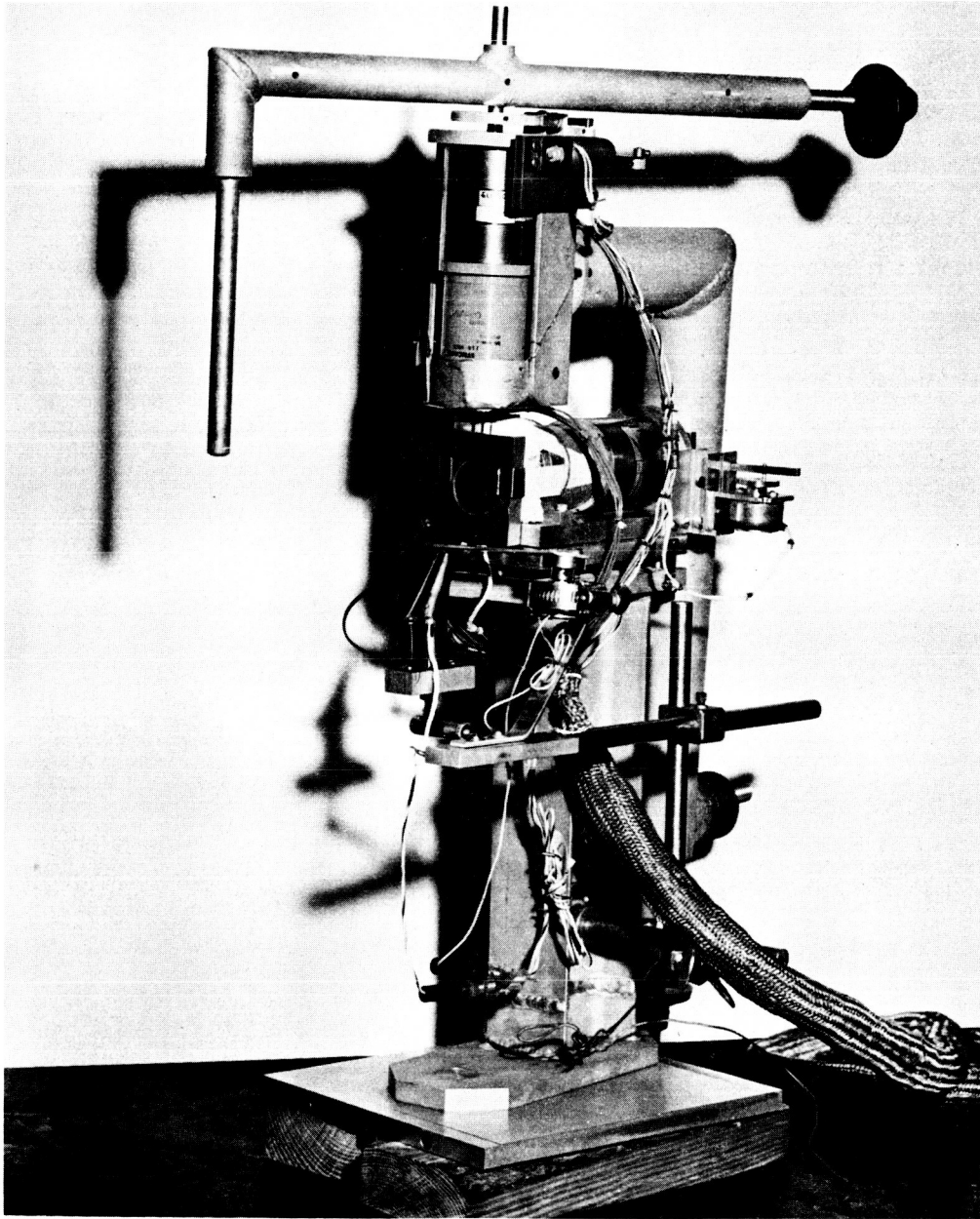
DETECTOR POSITIONING MECHANISM

FIGURE 2.3

measured if the detector orifice of infinitesimal size were used, multiplied by the amplification factor A_d/R. Therefore the detector signal is a direct measure of either a) the time-dependent magnitude of the flux vector $J(t,\vec{r})$, b) the time-dependent density $n(t,\vec{r})$ within the finite volume determined by the active portion of the ionizing region, or c) both a) and b) depending upon whether the detector is of either a) the non-through-flow, b) the through-flow, or c) the mixed-flow type. As determined by calibration (see Chapter IV), the Orbitron detector used in the present studies behaved as a non-through-flow detector.

The Surface

The surface in most of the studies of particle-surface collisions described here was formed by depositing silver on mica immediately prior to the beginning of the observation period. Saltsburg and Smith (Reference 33) determined, from back-reflection x-ray diffraction studies, that if the mica substrate is held at 550 ± 30 K during the deposition period, then the (111) plane of the resulting silver crystal is parallel to the mica surface. The mica in both the Saltsburg and Smith experiments and the experiments reported here were cleaved in air and located then in the chamber which was evacuated. In a very recent paper (Reference 21), Jaeger, et al., report on their careful experimental studies of the structure of silver films deposited on mica substrates in ultra-high vacuum. They observed important differences in the structure of the deposited silver films depending upon a) whether the mica was cleaved in UHV (ultra-high vacuum) or in air and b) the amount of water adsorbed on the mica. They further conclude that "There is no epitaxial temperature per se for silver on mica". In view of these results, it is felt that no definite statement related to the structure of the deposited silver film in the experiments

reported here can be made, with the exception of conclusions drawn from the results themselves. This is discussed further in Chapter V in conjunction with interpretation of the results. Other surfaces used in these collision studies include mica, glass and brass surfaces, all of which were contaminated by background and beam gases.

Procedure

The sequence of events followed in preparing and executing an experiment involving scattering from freshly deposited silver surfaces is as follows:

1. Align the detector positioning device. This was done by means of a light beam originating from a light source substituted for the molecular-beam source. The target holder was oriented perpendicular to the beam direction by ensuring that the light reflected from the (shiny) brass target holder fell on the collimating orifice through which the incident light beam traveled. The target then was oriented manually to the desired beam incidence angle. The beam incidence angle for all the experiments reported here was $\theta_i = 60^{\circ}$ (see Figure 2.4).

2. Attach and align the detector. The detector was attached to the arm of the positioning mechanism at the desired radial distance R from the center of the target holder. It was aligned then so that when the positioning arms were rotated externally by means of servo motors to angular coordinates corresponding to those of the incident beam, the detector axis would coincide with the beam axis. This also was done by means of a light beam collimated along the same path that would be followed by a molecular beam. When the image of the collimating orifice on the target holder could be seen distinctly as a complete ellipse, the axis of the detector was considered to be aligned.
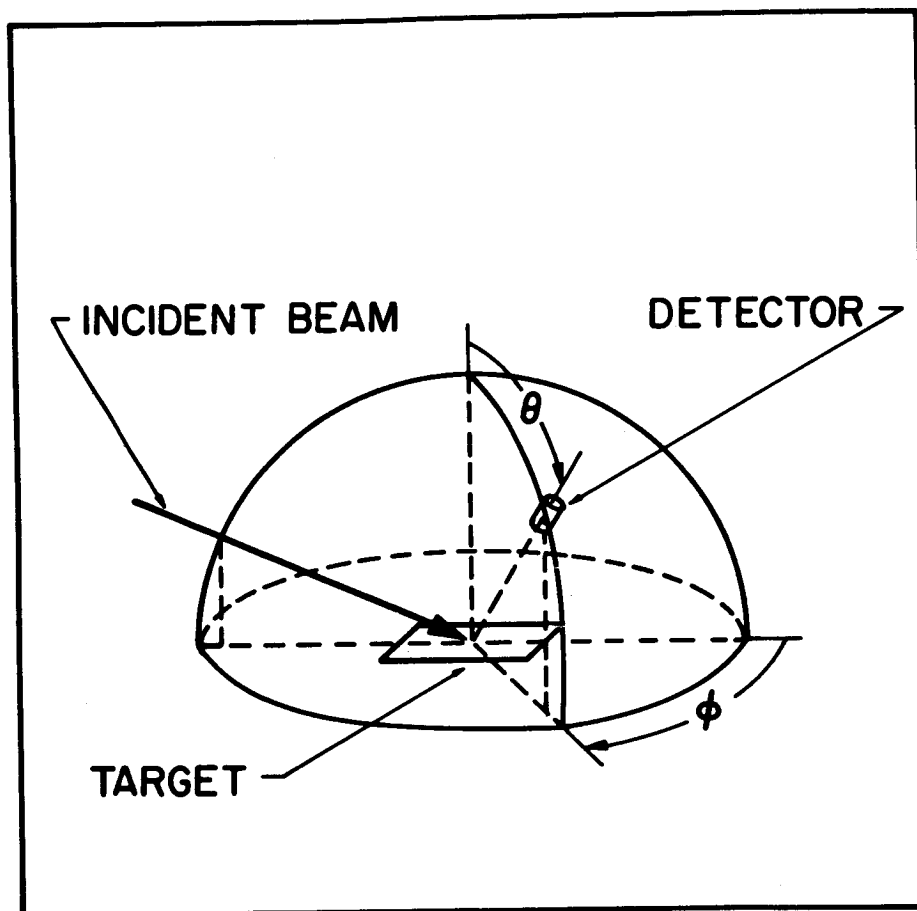
COORDINATE SYSTEM USED TO DESCRIBE ANGULAR
POSITION OF DETECTOR RELATIVE TO INCIDENT
BEAM AND TARGET

FIGURE 2.4

The total alignment of the detector positioning system was checked by rotating the detector holding arms (using the external controls to the servo motors) to angular-coordinates settings that would correspond to the specular-reflection direction. If the whole system is aligned, the image of the collimating orifice on a surface perpendicular to the path of the reflected beam:

a) is visible (proving that the detector axis is aligned and that the surface of the target holder contains the point of intersection of the two axes of rotation),

b) has the same shape as the collimating orifice (i.e., circular) in the case when $\theta_i = 60^o$ (proving the accuracy of the incidence angle setting).

3. Evacuate the molecular-beam system and initiate flow of liquid nitrogen through a coil in the detection chamber and a baffle upstream from the detection chamber diffusion pump. The measured background pressure in the detection chamber was in the vicinity of 10^{-6} torr during the experiments.

4. Heat the mica sheet.

5. When the mica has reached the desired temperature, shut off the target heaters and turn on the heater imbedded in a ceramic crucible which contains the silver to be deposited on the target.

6. Turn on the molecular beam, the chopper, and the beam detector.

7. At the end of the deposition period, shut off the crucible heater and close the shutter in the path of the evaporating silver.

8. Record detector signals for several values of angular coordinates and for several values of time since the end of silver

deposition. The steps omitted in experiments involving the mica, glass and brass surfaces are obvious.

CHAPTER III
BEAM MODULATION AND TIME-OF-FLIGHT SPECTROSCOPY

Introduction

The purpose of beam modulation and time-of-flight spectroscopy is to determine the velocity distribution and density of a molecular flow field. The principle is straightforward. If a known dynamic (time-dependent) perturbation is introduced at a well-defined point in the molecular flow field, its propagation in space is determined by the velocity distribution of the flow field. This propagation can be measured in the time domain by sensing either the instantaneous density or flux of molecules at a given point in space, removed from the point of modulation by a known distance L. The time sequence of instantaneous densities or fluxes is referred to as the time-of-flight (TOF) signal and is determined by the characteristics of the time-dependent perturbation, the speed distribution of the molecular field (along the radius vector joining the perturbation and sensing points) and the distance L. The perturbation introduced is called frequently modulation or chopping. Time-of-flight spectroscopy refers to the procedure by which a measured TOF signal is interpreted to yield the speed distribution of the steady-state beam. This choice of terminology is suggested by other spectroscopic methods (light spectroscopy, mass spectroscopy) which also operate on the analogous principle of sensing in a Fourier transformed domain the propagation of a known perturbation in a frequency field whose spectrum is to be determined.

In the experiments described here, the well-collimated incident beam was modulated by means of rotating a disk (the chopper disk) with two diametrically opposed slits in the path of propagation of the

steady state beam. During a finite time interval (determined by the angular opening of the slit, the cross sectional area of the beam, and the angular speed of the disk) a pulse of the steady state beam is allowed to propagate downstream of the disk, and the atoms are sensed sequentially as they arrive at a distance L downstream.

If, in some experiments, it is necessary to select only those molecules which lie within a narrow speed range, a second disk (the "filter" disk) is added at a fixed distance from the chopper disk. The slits of the filter disk are displaced by a fixed phase angle from those of the first disk. The two rotating disks are referred to as the "chopper-filter" or as the "velocity selector". In the experiments described below, the selection of the speed bands was not essential. The chopper-filter was used, however, because it filtered out the light originating from the arc-jet. Whenever only the chopper disk was used, the light signal provided a reference point on the time axis of the recorded signal.

The design characteristics of the chopper and chopper-filter and their respective driving motors are described in detail in References 23 and 24. The remainder of this chapter is devoted to the analytical description of the modulation and TOF spectroscopy method.

The method, developed for the first time here, uses relationships between the central moments of a general family of speed distribution functions and those of the corresponding time-of-flight analogues. These relationships are used then in deriving moment equations relating the central moments of measured TOF pulses to the corresponding moments of the chopper gate (admittance) function and parameters of the speed distribution function. In particular, the zeroth-moment relationship relates the area under the measured signal to the density of the steady-state beam.

The analysis developed in this chapter is used in the next two chapters to characterize dynamically a detector and a surface in a scattering experiment.

Analysis of a Modulated Beam Signal

Consider a collimated beam of atoms having parallel trajectories with a steady-state speed distribution $f(u)\,du$. The cross-section of the beam is assumed to be well defined, i.e., the atom density n in the beam is assumed to be constant within the boundaries of this cross-section and negligible outside. The speed distribution is taken to be uniform across the cross-section of the beam. A chopper disk, with its axis parallel to the trajectory of the beam particles, rotates at an angular speed ω. A slit in the disk with angular opening $\overset{\bullet}{\alpha}$ admits beam particles downstream of the disk whenever it sweeps across the beam. An ionization detector is placed at a distance L_{CD} downstream from the chopper disk. The background pressure is assumed to be sufficiently low so that scattering of beam atoms by background molecules along the distance L_{CD} is negligible. The ionizing region is considered to be a plane perpendicular to the axis of the beam, and the distance L_{CD} is measured between the chopper disk and the ionizing plane. The dynamic characteristics of the detector are examined in detail in Chapter IV.

Let $A(t)$ be the instantaneous cross-sectional area of the beam admitted by the slit at time t, i.e., the instantaneous parallel projection of the slit area along the atom trajectory upon the beam cross-sectional area. Let $t = 0$ represent the time when the first particle is admitted by the slit. At time λ, the rate at which atoms in the speed-ratio range (s, ds) are admitted by the slit is:

$$J(s)\,ds A(\lambda)$$

where:

$J(s)\,ds = nsf(s)\,ds$ is flux of atoms in range $(s, s+ds)$

$s = u/\gamma$ is speed ratio

$\gamma = (2kT/m)^{\frac{1}{2}}$ is most probable random speed

T = beam temperature, degrees K

$f(s)\,ds$ = fraction of atoms in beam with speed ratio in range (s, ds)

k = Boltzmann's constant

m = mass of atom

The number of atoms in the speed ratio range (s, ds) admitted by the slit in the time interval (s, ds) is

$$dN(\lambda, s) = J(s)\,ds\,A(\lambda)\,d\lambda \qquad (3.1)$$

An atom admitted at time λ will arrive at $x = L_{CD}$ at time $t \geq \lambda$ if its speed ratio is:

$$s(\lambda, t) = \frac{L_{CD}}{(t-\lambda)\gamma} \qquad (3.2)$$

Divide both sides of Equation (3.1) by dt,

$$\frac{dN(\lambda, t)}{dt} = J(s)\,\frac{ds}{dt}\,A(\lambda)\,d\lambda \qquad (3.3)$$

Equation (3.3) represents the instantaneous rate at which atoms selected from those admitted in the interval $(\lambda, d\lambda)$ cross the ionizing region at time t.

The integral of Equation (3.3) represents the rate at which atoms cross the ionizing plane at time t.

$$\frac{dN(t)}{dt} = \int_0^t J(s)\,\frac{ds}{dt}\,A(\lambda)\,d\lambda \qquad (3.4)$$

Dividing both sides of Equation (3.3) by $u = \gamma s$ and integrating, to account for the atoms admitted over the finite time interval from 0 to t, one obtains:

$$\frac{dN(t)}{dx} = n \int_0^t f(s) \frac{ds}{dt} A(\lambda) \, d\lambda \tag{3.5}$$

where $dN(t)/dx$ is the instantaneous number of atoms per unit path length.

Define the time-domain analogues of the speed distribution function $f(s)$ and the flux $J(s)$

$$\rho(t) \triangleq f(s) \frac{ds}{dt} \tag{3.6}$$

$$\phi(t) \triangleq sf(s) \frac{ds}{dt} \tag{3.7}$$

and rewrite (3.4) and (3.5):

$$\frac{dN(t)}{dt} = \gamma \, n \int_0^t \phi(t-\lambda) \, A(\lambda) \, d\lambda \tag{3.8}$$

$$\frac{dN(t)}{dx} = n \int_0^t \rho(t-\lambda) A(\lambda) \, d\lambda \tag{3.9}$$

The right-hand side of Equations (3.8) and (3.9) represents the convolution of two functions of time which, when Laplace transformed, yields the product of the Laplace transforms of each function

$$L\left\{\frac{dN(t)}{dt}\right\} = \gamma \, n \, L\left\{\rho(t)\right\} L\left\{A(t)\right\} \tag{3.10}$$

$$L\left\{\frac{dN(t)}{dx}\right\} = n \, L\left\{\phi(t)\right\} L\left\{A(t)\right\} \tag{3.11}$$

Equations (3.10) and (3.11) represent the formal solution to the single-disk-modulation problem. They facilitate solving Equations (3.8) and (3.9) to determine the speed distribution function $f(s)$ from a measurement of $dN(t)/dx$ or of $dN(t)/dt$ and knowledge of the admittance (gate) function $A(t)$.

$dN(t)/dx$ is proportional directly to the instantaneous beam density as measured by a through-flow detector:

$$\frac{dN(t)}{dx} = A_b \, n_b(t) \tag{3.12}$$

where

A_b = effective cross sectional area of beam

$n_b(t)$ = instantaneous beam density, number/volume, as measured in detector

$dN(t)/dt$ is related directly to the instantaneous density in the ionizing section of a non-through-flow detector. This is discussed in greater detail in Chapter IV.

The computational difficulty in solving (3.8) or (3.9) is simplified considerably if the functional form of $f(s)$ is known. The problem then is reduced to determining the unknown parameters of $f(s)$. This simplified problem is treated now in greater detail.

Let the speed distribution be of the form:

$$f_n(s) \, ds = C_n \, s^n \exp - (s-S)^2 \, ds$$

$$= C_n \, F_n(s) \, ds \tag{3.13}$$

with the normalization factor C_n given by:

$$C_n = \mu_o^{-1} \{ F_n(s) \} \tag{3.14}$$

In view of Equations (B.7) and (B.13) in Appendix B, the zeroth, first and second moments of $dN(t)/dx$ and $dN(t)/dt$ may be related to the corresponding moments of $\rho(t)$ and $\phi(t)$ respectively:

$$\mu_o \left\{ \frac{dN(t)}{dx} \right\} = n \, \mu_o \{ \rho(t) \} \, \mu_o \{ A(t) \} \tag{3.15}$$

$$\mu_o \left\{ \frac{dN(t)}{dt} \right\} = \gamma \, n \, \mu_o \{ \phi(t) \} \, \mu_o \{ A(t) \} \tag{3.16}$$

$$\eta_1 \left\{ \frac{dN(t)}{dx} \right\} = \eta_1 \{ \rho(t) \} + \eta_1 \{ A(t) \} \tag{3.17}$$

$$\eta_1 \left\{ \frac{dN(t)}{dt} \right\} = \eta_1 \left\{ \phi(t) \right\} + \eta_1 \left\{ A(t) \right\} \tag{3.18}$$

$$\nu_2 \left\{ \frac{dN(t)}{dx} \right\} = \nu_2 \left\{ \rho(t) \right\} + \nu_2 \left\{ A(t) \right\} \tag{3.19}$$

$$\nu_2 \left\{ \frac{dN(t)}{dt} \right\} = \nu_2 \left\{ \phi(t) \right\} + \nu_2 \left\{ A(t) \right\} \tag{3.20}$$

The moments of $\rho_n(t)$ and $\phi_n(t)$ are related in turn to the moments of $f_n(s)$ as shown in Appendix A $\Big($Equations (A6.1) to (A6.9)$\Big)$.

Substituting for the moments of $\rho_n(t)$ and $\phi_n(t)$ in Equations (3.15) to (3.20) and rearranging, one obtains the following relationships:

$$\frac{\mu_0 \left\{ \frac{dN(t)}{dx} \right\}}{\mu_0 \left\{ A(t) \right\}} = n \tag{3.21}$$

$$\frac{\mu_0 \left\{ \frac{dN(t)}{dt} \right\}}{\mu_0 \left\{ A(t) \right\}} = \gamma n \, \eta_1 \left\{ f_n(s) \right\} \tag{3.22}$$

$$\eta_1 \left\{ \frac{dN(t)}{dx} \right\} - \eta_1 \left\{ A(t) \right\} = \frac{L_{cD}}{\gamma} \eta_{-1} \left\{ f_n(s) \right\} \doteq \frac{L_{cD}}{\gamma} \Theta_{n-1}(S) \tag{3.23}$$

$$\eta_1 \left\{ \frac{dN(t)}{dt} \right\} - \eta_1 \left\{ A(t) \right\} = \frac{L_{cD}}{\gamma} \eta_{-1} \left\{ f_{n+1}(s) \right\} \doteq \frac{L_{cD}}{\gamma} \Theta_n(S) \tag{3.24}$$

$$\frac{\nu_2 \left\{ \frac{dN(t)}{dx} \right\} - \nu_2 \left\{ A(t) \right\}}{\left[\eta_1 \left\{ \frac{dN(t)}{dx} \right\} - \eta_1 \left\{ A(t) \right\} \right]^2} = \frac{\eta_1 \left\{ f_{n-1}(s) \right\}}{\eta_1 \left\{ f_{n-2}(s) \right\}} - 1 \doteq \Omega_{n-1}(S) \tag{3.25}$$

$$\frac{\nu_2 \left\{ \frac{dN(t)}{dt} \right\} - \nu_2 \left\{ A(t) \right\}}{\left[\eta_1 \left\{ \frac{dN(t)}{dt} \right\} - \eta_1 \left\{ A(t) \right\} \right]^2} = \frac{\eta_1 \left\{ f_n(s) \right\}}{\eta_1 \left\{ f_{n-1}(s) \right\}} - 1 \doteq \Omega_n(S) \tag{3.26}$$

Note that the left-hand sides of these equations represent directly measurable quantities. The right-hand side of Equations (3.25) and (3.26) are functions of S alone. Thus, it is possible to determine

S, L_{CD}/γ and n_b from Equations (3.21), (3.23) and (3.25) if a through-flow detector is used, or from Equations (3.22), (3.24) and (3.26) if a non-through-flow detector is used. Values of $\Omega_n(s)$ are displayed graphically in Figure 3.1, as a function of S, for values of n = 1, 2, 3, 4. The speed distribution of a well collimated nozzle beam with parallel atom trajectories is given by a value of n = 2, i.e.,

$$f_2(s) = C_2 s^2 \exp - (s - S)^2 \qquad (3.27)$$

Table 3.1 lists $\Theta_i(S)$ and $\Omega_i(S)$ explicitly in terms of S. Note that for large values of S it is not possible to distinguish between distribution functions with different values of n.

Table 3.2 lists the values of the moments of some typical gate functions. Here

$$T = \frac{\overset{o}{\alpha} + \overset{o}{\psi}}{\omega} \qquad (3.28)$$

with $\overset{o}{\alpha}$ = slit aperture angle

$\overset{o}{\psi}$ = angle through which rotor must turn in order to sweep a radial line on a rotor disk across the beam.

ω = angular speed

is the "open time" of the gate functions. The impulse gate function corresponds to the case where T is an arbitrarily small number. The trapezoidal gate function represents a beam of quasi-rectangular shape, with an arbitrary spanning angle $\overset{o}{\psi}$ (see Figure 3.2). The case $\overset{o}{\alpha} = \overset{o}{\psi}$ corresponds to a triangular pulse.

The rectangular gate function corresponds to either of the physical models:

$$\overset{o}{\alpha} \gg \overset{o}{\psi}$$

or

$$\overset{o}{\psi} \gg \overset{o}{\alpha} \qquad (3.29)$$
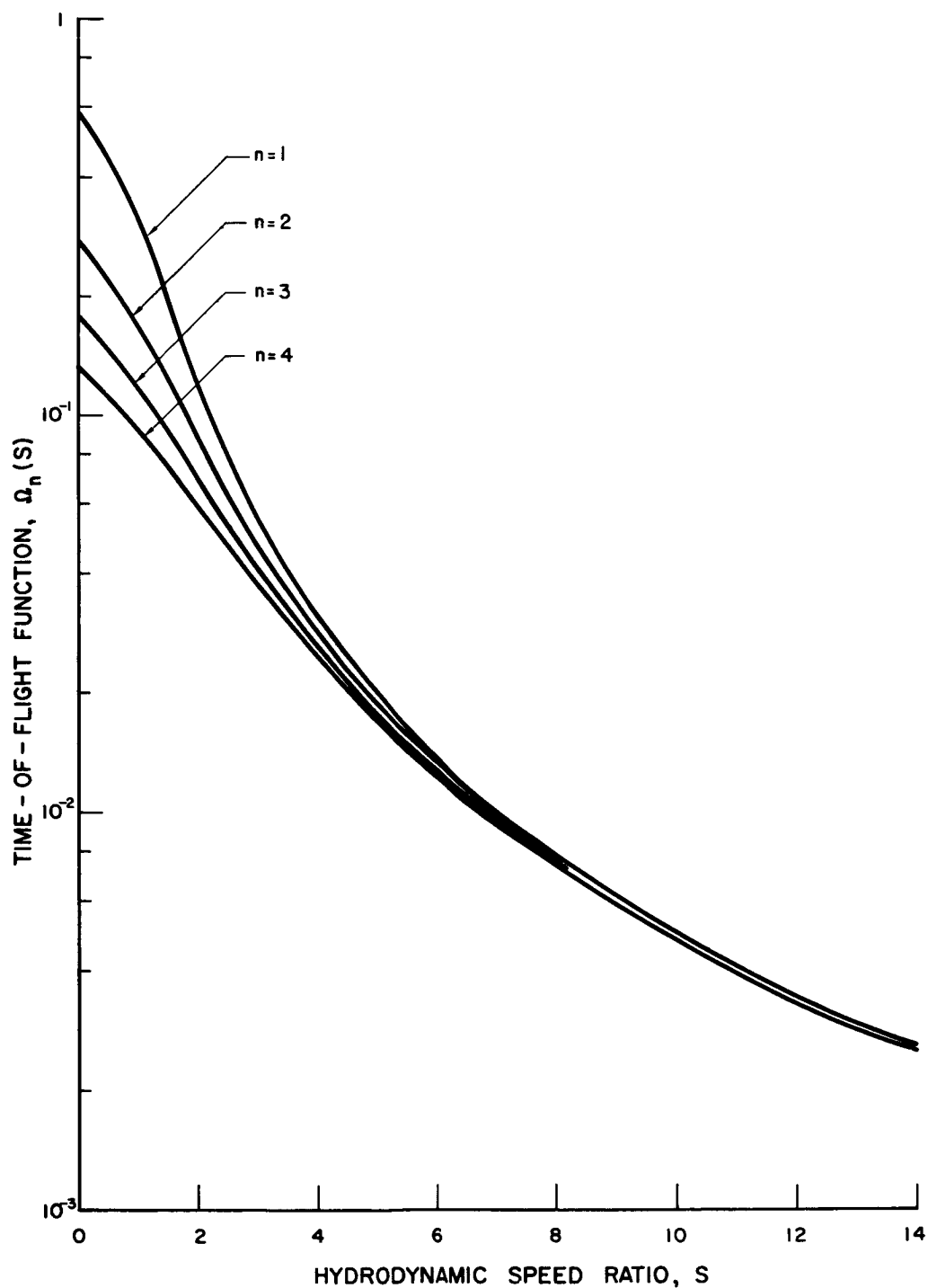
THE DERIVED TIME-OF-FLIGHT FUNCTION $\Omega_n(S)$ AS A
FUNCTION OF THE HYDRODYNAMIC SPEED RATIO
S FOR SEVERAL VALUES OF n

FIGURE 3.1

TABLE 3.1

ANALYTICAL EXPRESSIONS FOR THE TIME-OF-FLIGHT FUNCTIONS $\Theta_i(S)$ AND $\Omega_i(S)$

	$\Theta_i(S)$		$\Theta\Omega_i(S)$	
	$i=1$	$i=2$	$i=1$	$i=2$
General	$\dfrac{1}{S+r}$	$\dfrac{(S^2+1/2)+rS}{(S^3+3/2\,S)+r(S^2+1)}$	$\dfrac{1-2r(r+S)}{2(S+r)^2}$	$\dfrac{2(S+2r)(S+r)-1}{[2S(S+r)+1]^2}$
$S \gg r$	$\dfrac{1}{S}$	$\dfrac{2S^2+1}{2S^3+3S}$	$\dfrac{1}{2S^2}$	$\dfrac{2S^2-1}{(2S^2+1)^2}$
$S \gg 1$	$\dfrac{1}{S}$	$\dfrac{1}{S}$	$\dfrac{1}{2S^2}$	$\dfrac{1}{2S^2}$
$S \to 0$	$\dfrac{2}{\sqrt{\pi}}$	$\dfrac{\sqrt{\pi}}{2}$	$\dfrac{\pi}{2}-1$	$\dfrac{4}{\pi}-1$

$r = [\sqrt{\pi}\,(1+\text{erf}\,S)\,e^{S^2}-1]$

The expressions listed here are for a speed distribution of the form $s^2 e^{-(s-S)^2}$ (i.e., n=2). The subscript i is 1 or 2 depending on whether the functions are related to $\rho(t)$ or $\phi(t)$. (See Equations 3.23 through 3.26.)

TABLE 3.2

MOMENTS OF SOME TYPICAL GATE FUNCTIONS

$A(t)$	$\mu_o\{A(t)\}$	$\eta_1\{A(t)\}$	$\nu_2\{A(t)\}$
Trapezoidal	$\dfrac{A_b\,\overset{\circ}{\alpha}}{\omega} = AT$	$\dfrac{T}{2}$	$\dfrac{\overset{\circ}{\alpha}{}^2 + \overset{\circ}{\psi}{}^2}{12\,\omega^2} = \dfrac{T^2}{12} - \dfrac{\overset{\circ}{\alpha}\,\overset{\circ}{\psi}}{6\omega^2}$
Rectangular $\overset{\circ}{\alpha} \ll \overset{\circ}{\psi}$ or $\overset{\circ}{\psi} \ll \overset{\circ}{\alpha}$	$\dfrac{A_b\,\overset{\circ}{\alpha}}{\omega} = AT$	$\dfrac{T}{2}$	$\dfrac{T^2}{12}$
Triangular $\overset{\circ}{\alpha} = \overset{\circ}{\psi}$	$\dfrac{A_b\,\overset{\circ}{\alpha}}{\omega} = AT$	$\dfrac{\overset{\circ}{\alpha}}{\omega}$	$\dfrac{\overset{\circ}{\alpha}{}^2}{6\omega}$
Impulse (Dirac) $T \to \epsilon$ (ϵ arbitrarily small)	1	0	0
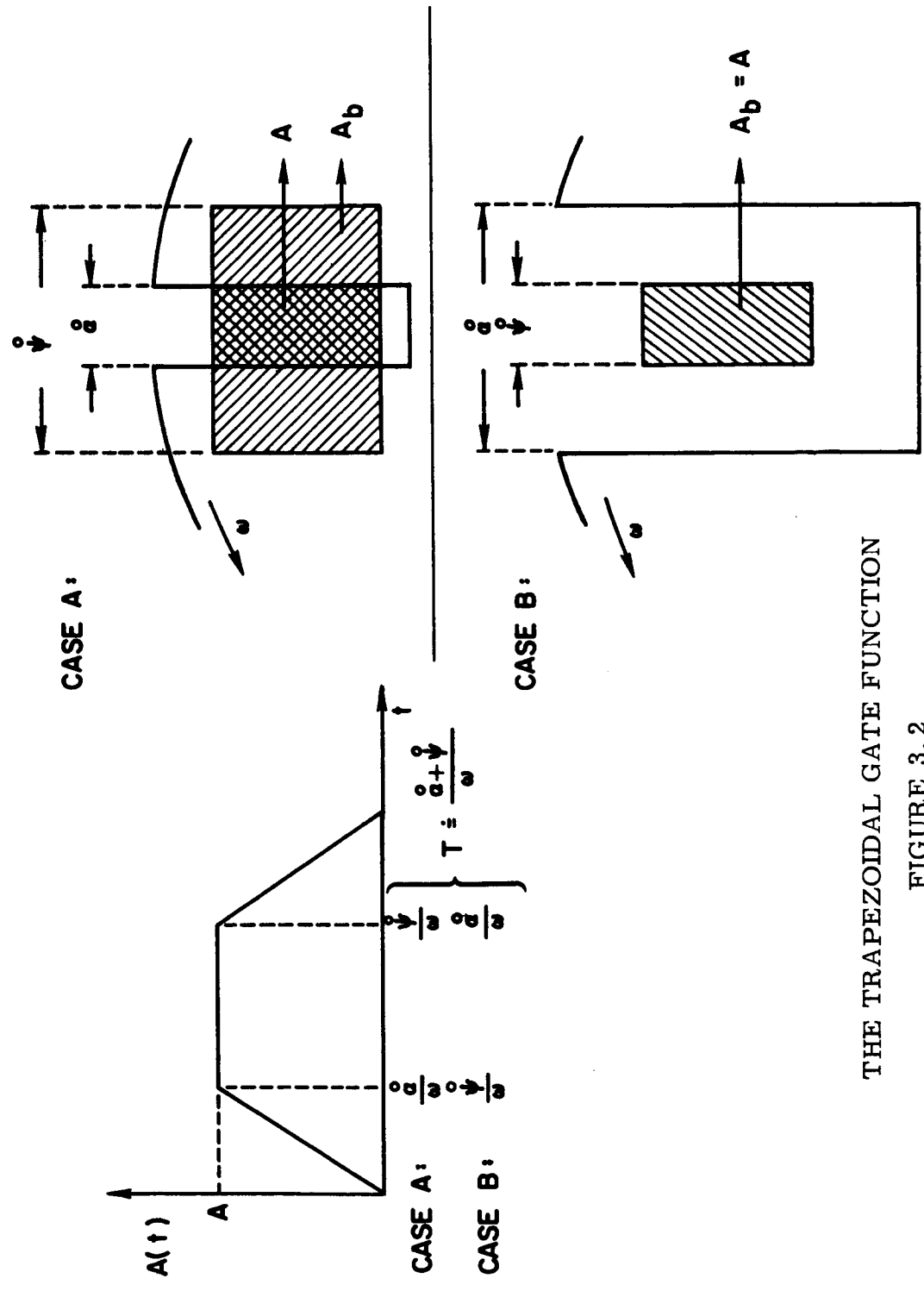
THE TRAPEZOIDAL GATE FUNCTION

FIGURE 3.2

The convolution integrals of Equations (3.8) and (3.9) have particularly simple solutions when $A(t)$ is an impulse function, i.e., when:

$$A(t) = \mu_0\{A(t)\}\, \delta(t) \qquad (3.30)$$

we can express $dN(t)/dx$ and $dN(t)/dt$ as follows:

$$\frac{dN(t)}{dx} = \mu_0\{A(t)\}\, n\, \rho(t) \qquad (3.31)$$

$$\frac{dN(t)}{dt} = \mu_0\{A(t)\}\, \gamma\, n\, \phi(t) \qquad (3.32)$$

Equations (3.8) and (3.9) have been solved analytically also for the case of a rectangular gate function:

$$A(t) = A\{\kappa(t) - \kappa(t-T)\} \qquad (3.33)$$

where

$$A = \frac{A_b^{\,o}\,\alpha}{\overset{o}{\psi}} \qquad (3.34)$$

and $\kappa(t)$ is the unit step function defined by

$$\kappa(t) = \begin{cases} 1 & \text{for } t > 0 \\ 0 & \text{for } t > 0 \end{cases} \qquad (3.35)$$

The exact solutions are given by Equations (C.6) and (C.7) in Appendix C. It is shown also that when the criteria

$$(T/t) \ll 1 \qquad (C.10)$$

$$T \ll (\gamma^2 t^3 / 2L_{CD}) / \left| \left(1 - (S\gamma t/L)\right) \right| \qquad (C.11)$$

are both satisfied, the instantaneous beam density $n_b(t)$ and beam flux $1/A_b\{dN(t)/dt\}$ are given by

$$n_b(t) = nT\rho(t) \tag{C.17}$$

$$(1/A)\ \frac{dN(t)}{dt} = \gamma\, nT\, \phi(t) \tag{C.18}$$

Note that a plot of $dN(t)/dx$ as given by Equation 3.5) versus $\overline{U}$ defined by

$$\overline{U} = \left(dN(t)/dt\right)/\left(dN(t)/dx\right) \tag{3.36}$$

represents the non-normalized speed distribution of atoms in the modulated pulse at a distance L_{CD} from the chopper. In general this distribution depends on the gate function $A(t)$. Only if $A(t)$ is impulsive does this speed distribution coincide with that of the steady-state beam. When $A(t)$ is impulsive we also have

$$\overline{U} = u \doteq L_{CD}/t \tag{3.37}$$

Conclusions

In this chapter it is shown that

a) The TOF signal is obtained analytically in the form of a convolution integral between the time-domain analogue of the steady-state beam speed distribution function and a gate function characterizing the modulation process. The operator g_{tf} (see Figure 2.1) is therefore nonlinear.

b) A central-moment expansion of this convolution integral provides a powerful, accurate, simple and physically meaningful method for determining the pertinent parameters of a speed distribution function as well as the density of the steady-state beam.

c) It is only when one wishes to assess the relative fit of alternate analytical forms of the distribution function to

experimental data (providing the data is sufficiently accurate for this purpose) that the complete inverse convolution is required. Otherwise one needs to determine only as many of the moments of the TOF signal as there are free parameters in the speed distribution to be determined.

d) For the general class of speed distribution functions discussed in Appendix A (out of which one in particular has physical significance and is considered here) the second central moment (the variance) is the highest central moment required in order to obtain the density, the most probable random speed γ, and the hydrodynamic speed ratio S.

The methods developed here are applied in the next chapter in obtaining the detector characteristic function $g_d(t)$ from calibration experimental runs. An extension of the same method is used in Chapter V to interpret the particle-surface scattering results.

CHAPTER IV

BEAM DETECTION

Introduction

Sensitive detection remains the nemesis of atomic- and molecular-beam experiments. Specifically, in scattering experiments, the sensitivity of the detector determines to a large extent the amount of information which can be extracted from an individual measurement.

The most widely used detectors ionize a small fraction of the neutral particles by electron bombardment and sense the resulting ion current. In this chapter, the dynamic processes involved in the detection process are analyzed and equations relating the ion current to the instantaneous flux and density characterizing the input are derived. This analysis should be applicable equally to the design, calibration and use of ion vacuum pumps which are based on the same dynamic principles.

The concept "linear detector" is introduced as a special case of the general class of ionization detectors. The concept "through-flow detector" is defined within this framework and in juxtaposition to the other newly defined subclasses such as "mixed flow," "Maxwellian" and "equilibrium" detectors.

A new type of molecular-beam detector was designed and built to fulfill the specific requirements of the experiments described in this report. Since the goal of the experiments was measuring the relative flux distribution of the scattered particles as a function of solid angle, high sensitivity was emphasized.

Sensitivity here is defined as the zeroth moment of the detector characteristic function. In the case of a through-flow detector,

the sensitivity is equal to the derivative of the ion current with respect to the density of the beam. In the case of a non-through-flow detector, the sensitivity is equal to the derivative of the ion current with respect to the incident flux of the beam.

High sensitivity was achieved in the Orbitron detectors (the detectors were given the same name given to the pressure gauges designed on the same principle)[29] by increasing the path length of the ionizing electrons and by relaxing the through-flow requirements (thus introducing a nonzero value of the detector characteristic time). A detector whose purpose is to measure speed distributions in addition to flux would require both a reduced characteristic time and a high sensitivity. The goal of the required compromise would be high accuracy in interpretation of the time-of-flight signal.

The detector was calibrated by a novel method suggested by the equations derived here. The characteristic dynamic function and the values of its parameters were obtained by means of this calibration. It is believed that this procedure and analysis would be valuable in designing and calibrating ionization detectors useful in measurements of the density and composition of the upper atmosphere by means of orbiting satellites. Using the technique developed here, one should be able to uncouple in an unambiguous fashion the dynamic parameters characterizing the motion of the satellite from the density and mean kinetic energy of the atmosphere in which the satellite travels.

Description and Analysis of the Detection Process

Consider a pulse of neutral, chemically stable molecular or atomic particles admitted into a detector. The pulse is characterized by the instantaneous values of the flux $J(t)$ and density $n(t)$ of the particles. As is shown in Chapter II, if the particles in the pulse

originate from a single plane at a distance L from the detector, (where they were characterized by a velocity distribution $f_b(v)$ and a density n_b) both J(t) and n(t) can be determined from these quantities and from a time-of-departure distribution function A(t).

In this section we derive the characteristic function or operator of an ionization detector which relates the instantaneous ion current produced by the detector to J(t) and n(t). Formally one can write

$$I^+(t) = g_d X \left(J(t), \; n(t) \right) \tag{4.1}$$

Here g_d is an operator and Equation (4.1) is to be read as follows: "the operator g_d operates on the input functional X to produce the output function $I^+(t)$." In general g_d need not be a linear operator. It is linear if it depends only on the design and operational parameters of the detector and not on X or I^+.

Figure 4.1 is a signal-flow diagram representing dynamically the detection process. A fraction c of the incident flux passes through the ionizing region, unimpeded except for the ionizing collisions with the electrons. When pure (i.e., when $c \rightarrow 1$), this mode of operation is defined as the through-flow mode. The remaining fraction (1-c) of the incident flux undergoes collisions with the walls of the ionization cavity while being ionized. This transient process continues until the excess particle density within the cavity, $n_d(t)$, is depleted by net effusion to the steady state environment outside the detector.

Note that $n_d(t)$, the instantaneous density in the cavity, is not equal to the instantaneous density of particles in the incident pulse, n(t), unless c = 1. The density $n_d(t)$ is determined by the velocity distribution function of the neutral particles inside the cavity $f_d(\vec{v})$,
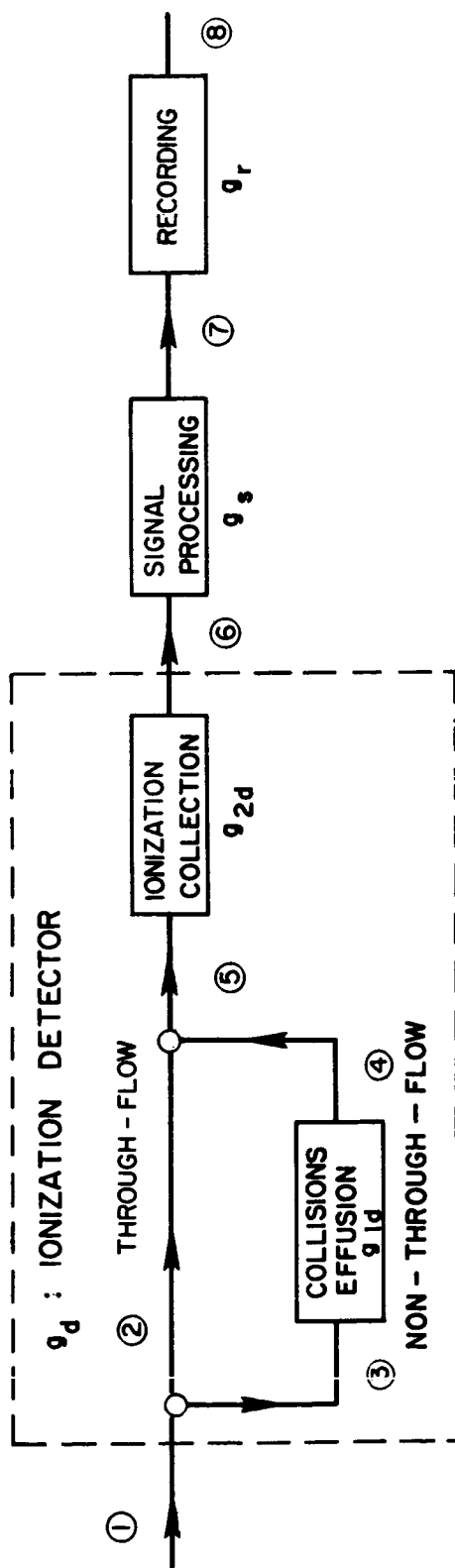
SIGNAL-FLOW REPRESENTATION OF MOLECULAR
BEAM DETECTION USING AN IONIZATION DETECTOR

FIGURE 4.1

which is determined partially by the kinetics of the wall collision and effusion processes. The mode of operation of the detector realized when c=0 is called the <u>non-through-flow mode</u>.

Let g_{1d} be the operator describing the wall-collision and effusion dynamics, and let g_{2d} be the operator describing the dynamics of the ionization and ion-collection processes. It can be shown from information theory and without assuming linearity of the differential equations describing these processes that

$$g_d = g_{2d} [c + (1-c) g_{1d}] \tag{4.2}$$

If g_{2d} and g_{1d} are known, Equations (4.1) and (4.2) represent the solution to the problem.

Certain models of practical importance are examined now. If the operator g_d is linear, then the detector is called a <u>linear detector</u>. If g_d is linear, the representations of this operator in different domains are related by linear transformations. Specifically, let its representation in the time domain $g_d(t)$ be Laplace transformable. Under these conditions (as shown in Appendix B) the following relations exist between $I^+(t)$ and $X(t)$ and between their respective moments:

$$I^+(t) = \int_0^t g_d(t-\lambda)\, X\{J(\lambda),\ n(\lambda)\}\, d\lambda \tag{4.3a}$$

$$\mu_o\{I^+(t)\} = \mu_o\{g_d(t)\}\, \mu_o\{X(t)\} \tag{4.3b}$$

$$\eta_1\{I^+(t)\} = \eta_1\{g_d(t)\} + \eta_1\{X(t)\} \tag{4.3c}$$

$$\nu_j\{I^+(t)\} = \nu_j\{g_d(t)\} + \nu_j\{X(t)\} \tag{4.3d}$$

$$J = 2, 3, \ldots$$

The operator $g_d(t)$ can be looked upon as the calibration function of the detector. In fact the calibration procedure would involve measurement of the $I^+(t)$ function when a known pulse (whose $J(t)$ and $n(t)$ are known) is admitted into the detector. Equations (4.3) could be used then to determine $g_d(t)$. If the detector is required just for the purpose of measuring densities, only the zeroth moment $\mu_o\{g_d(t)\}$ is sufficient. $\mu_o\{g_d(t)\}$ is called the calibration constant of the detector. Higher moments are required only if the detector is used in time-of-flight measurements to determine the velocity distribution of a neutral-particle flow field. In that case the number of moments of $g_d(t)$ which have to be known is determined by the number of parameters required to determine the distribution function of the magnitude of the velocity vector in a given direction.

It is shown in Appendix B that, in view of Equation (4.2), the moments of $g_d(t)$ can be related to those of $g_{1d}(t)$ and $g_{2d}(t)$ by the following relations:

$$\mu_o\{g_d(t)\} = \mu_o\{g_{d2}(t)\} \left[C + (1-C) \, \mu_o\{g_{d1}(t)\} \right] \qquad (4.4a)$$

$$\eta_1\{g_d(t)\} = \eta_1\{g_{d2}(t)\} + \frac{\mu_1\{g_{d1}(t)\}}{\mu_o\{g_{d1}(t)\} + \frac{c}{1-c}} \qquad (4.4b)$$

For the purpose of obtaining a feeling about the physical implications of the linearity constraint, we now examine the physical processes described by each of the operators g_{1d} and g_{2d}.

The operator g_{2d} describes the ionization and ion-collection process. The characteristic times describing these electron-molecule collision processes are, in all present applications, smaller by a few orders of magnitude than the characteristic times involved in the wall collisions and effusion of gas particles.

Therefore without loss of any generality we can write

$$g_{2d}(t) = K\left(\delta(t)\right) \qquad (4.5)$$

In fact, if the mean free path of the electrons is large in comparison with the dimensions of the ionizing region, the ion current produced is given by

$$I^+(t) = I^- \sigma \ell \, n_d(t) \qquad (4.6)$$

so that $K = I^- \sigma \ell$.

The operator g_{1d} represents the unsteady effusive flow across the plane separating the detector from the steady-state inactive environment. It is linear if the velocity distribution function of the neutral particles in the cavity, $f_{1d}(\vec{v}, t)$ is independent of the instantaneous mean speed, $\overline{U}(t)$, of the incident particles. $\overline{U}(t)$ is defined as follows:

$$\overline{U}(t) \doteq J(t)/n(t) \qquad (4.7)$$

Note that the linearity constraint does not require that $f_{1d}(\vec{v}, t)$ be time-independent. If it is, then the time-dependent flux, $J_{1d}(t)$, is given by the product of the time-dependent density and a time-independent mean speed, $\overline{U}_{1d}$, calculated from $f_{1d}(\vec{v})$. Under these conditions, it is possible to define a simplified operator, g'_{1d},

$$X_4\{n_{1d}(t)\} \doteq g'_{1d} X\left(J_3(t)\right) \qquad (4.8)$$

whose time domain representation is given by

$$g'_{1d}(t) \doteq K_1 \exp(-t/\tau_1) \qquad (4.9)$$

where τ_1 is the characteristic time for the effusion process in this model and is given by

$$\tau_1 = L_e / \overline{u}_{1d} \tag{4.10}$$

If $f_{1d}(\vec{v})$ is in addition Maxwellian (but not necessarily in thermal equilibrium with the walls of the detector) then K_1 and L_e are given by

$$K_1 = A/V \tag{4.11}$$

$$L_e = 4V/A \tag{4.12}$$

where A is the area of the orifice through which the molecules communicate with the environment and V is the volume of the detector cavity. The following equations summarize the description of the different types of linear ionization detectors.

A. Through-Flow

$$I^+(t) = K\, n(t) \tag{4.13}$$

$$\text{Moment}\left(I^+(t)\right) = K\, \text{Moment}\left(n(t)\right) \tag{4.14}$$

B. Non-Through-Flow

$$I^+(t) = K \int_0^t g_{1d}(t-\lambda)\, J(\lambda)\, d\lambda \tag{4.15}$$

$$g_{1d}(t) = K_1 \exp(-t/\tau) \tag{4.16}$$

$$\mu_0\{I^+(t)\} = K\, k_1 \tau_1 \mu_0\{J(t)\} \tag{4.17}$$

$$\eta_1\{I^+(t)\} = \tau_1 + \eta_1\{J(t)\} \tag{4.18}$$

$$\nu_j\{I^+(t)\} = \nu_j\{\exp -t/\tau_1\} + \nu_j\{J(t)\}$$
$$j = 2, 3, \ldots \tag{4.19}$$

C. Mixed-Flow

$$I^+(t) = \left[cI^+_{tvf}(t) + (1-c) I^+_{ntvf}(t) \right] \qquad (4.20)$$

$$\mu_o\{I^+(t)\} = K\left[c\mu_o\{n(t)\} + (1-c) k_1 \tau_1 \mu_o\{J(t)\} \right] \qquad (4.21)$$

$$\mu_j\{I^+(t)\} = c\, \mu_j\{I^+_{tvf}(t)\} + (1-c) \mu_j\{I^+_{ntvf}(t)\} \qquad (4.22)$$

The through-flow (c=1) and the non-through-flow (c=0) modes are special cases of the mixed-flow modes.

D. Non-Through-Flow Approximation to Mixed-Flow

This approximation involves two successive stages. In the first stage the instantaneous current is approximated by a linear operation on the input-flux (or rate) parameter alone, and does not depend on the instantaneous incident density.

$$I^+(t) = K \int_o^t g_d(t-\lambda) J(\lambda)\, d\lambda$$

or

$$\qquad (4.23)$$

$$I^+(t) = K \int_o^t g_d(t-\lambda) \left[dN(\lambda)/dt \right] d\lambda$$

This approximation is useful for calibration purposes; if during calibration, it turns out that one finds

$$\eta_1\{g_d(t)\} = \nu_2^{\frac{1}{2}} \{g_d(t)\} \qquad (4.24)$$

then the second stage of this approximation

$$g_d(t) = k_d \exp(-t/\tau) \qquad (4.25)$$

is applicable to a second-moment order. (Note that, if Equation (4.25) is applicable, then each side of Equation (4.24) equals τ).

In practice the effect of nonlinearity is minimized if any combination of the following design or experimental conditions is optimized:

1. The detector is designed such that a large fraction of the atoms pass through the detector region unimpeded, i.e., the detector approaches the through-flow mode. Under these conditions the only possible source of nonlinearity (the collisions with the walls) does not exist. This condition has to be maintained both during calibration and during application.

2. If τ_d is determined from a calibration by means of a beam of known velocity distribution and if the detector is used then to measure the density and mean speed of the beam of unknown but different velocity distribution, then any nonlinearity of the detector can be expressed quantitatively in the form of a $\Delta\tau_e$. This effect will be negligible if

$$\Delta\tau_e \ll \eta_1\{J(t)\} \tag{4.26}$$

3. If the particles undergo many collisions with the walls before being ionized, then their energy and momentum identity tends to be lost. The more collisions, the smaller the effect of their initial velocity distribution when crossing over into the active region, and hence the smaller the chance of nonlinearity. The number of collisions can be increased by proper baffling of the channel leading to the ionizing region. A detector in which the molecules achieve thermal equilibrium with the walls before being ionized is called an equilibrium detector. Note that this constraint does not eliminate its usefulness in determining the velocity distribution if it is used as the transducer element in a time-of-flight modulated-beam arrangement. The disadvantage of such a detector lies in the fact that τ_d has a

large value and, therefore, much larger flight times are required to obtain meaningful results. The advantage lies in the fact that an amplification is obtained which is useful in determining the total flux in a pulse.

Design of the Orbitron Detector

Design Considerations

The following requirements were imposed on the detector used in the scattering experiments.

1. A high signal-to-noise ratio.
2. The capability of detecting a transient pulse of atoms with density of 10^{-6} molecules/cc or lower.
3. The capability of monitoring both the incident beam and the scattered beam. This capability facilitates aligning the target and zeroing the positioning device.

4. A relatively low value of characteristic time so that the transient nature of the pulse can be determined with precision.

These requirements were met by a series of detectors designed and built specially for the scattering experiments reported here and characterized by increased path lengths of the ionizing electrons. As indicated by Equation (4.6), the through-flow sensitivity K is proportional directly to the path length of the electrons. Two alternate methods of achieving increased path lengths had been reported in the literature. In the magnetron, a magnetic field orbits the electrons. This principle has been applied successfully in the design of commercially available pressure gauges. The disadvantages of this approach for the present application included a) the

bulkiness of the detector would block a large portion of the incident beam and b) the magnetic field close to rotating chopper disks could create bothersome currents in the collector circuit.

An alternate principle for orbiting the electrons was described by Mourad, Pauly and Herb.[29] Ionizing electrons are injected into an electrostatic field between two concentric cylinders with energies and angular momenta such that the electron path lengths are large in comparison with the radii of the cylinders. The relatively large electron path lengths yield high detector sensitivities at relatively low electron current.

Pressure gauges built by Mourad and co-workers[29] have reportedly electron path lengths of the order of 1000 cm at electron ionizing currents of the order of tens of microamps. (Low electron currents would be of special value for density measuring instruments in satellites and space vehicles where electric power is at a premium). For the present application, the through-flow sensitivity factor K (not the path length) was maximized. An optimum value of the electron ionizing current (maximizing the value of K) was observed. This value (a function of the configurational design of the detector) varied from 0.5 to 1.5 milliamperes.

A photograph of one of the later models of the detector is shown in Figure 4.2. An earlier version is shown in Figure 18 of Reference 23. The active components included a 3 mil tungsten wire located at the axis of a thin-walled metallic cylinder and a coiled filament serving as the heated cathode. The 3 mil central wire served as the electron anode while the cylinder acted as the ion collector. In later models, a grounded concentric shield of slightly larger diameter than the collector diameter improved significantly the signal-to-noise ratio.
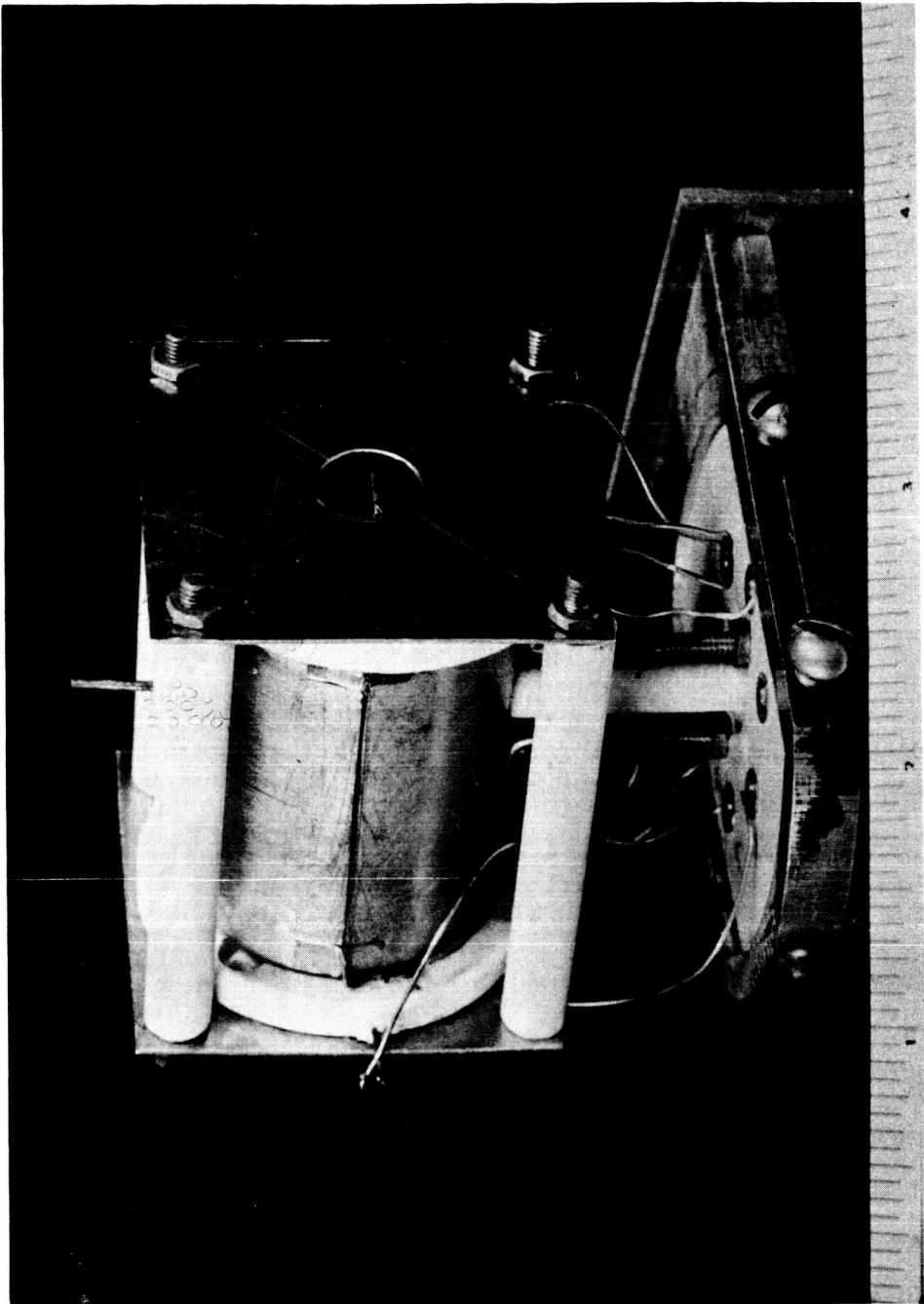
IONIZATION DETECTOR, A MODIFICATION OF THE
ORBITRON PRESSURE GAUGE

FIGURE 4.2

As indicated in Figure 4-3, the anode was maintained at potentials in the range of 500-650 volts. It was observed generally that the performance was relatively insensitive to the anode voltage. However, for a given cathode temperature (i.e., for a given heating current), the ion current increased significantly with the bias potential up to a certain value and then decreased sharply. The detector was operated with a bias potential slightly lower than the value at which this ion current peaked. The potential of the collector cylinder was fixed by the potential drop across the load resistor.

Signal Processing

The transient ion-current signal produced at the collector cylinder of the Orbitron detector is processed as follows:

a) The ion current is transmitted by the central lead of a triaxial signal cable to a load resistor of 15 Megohms. The ends of the load resistor are connected to the input and ground connectors of a Keithley 102B decade isolation amplifier with a maximum amplification of 10^3. In order to reduce the effective capacitance between the signal lead and the grounded outer shield, the inner shield is driven from the amplifier output at the same phase as the signal. Since the same length of signal wire is used during calibration and during measurements, the effective capacitance between the collector and ground is expected to be small and constant. Since any remaining capacitance acts dynamically as a characteristic time appearing in the dynamic operator function

$$g_s = (1/\tau_c) \exp - (t/\tau_c) \tag{4.27}$$

$$\tau_c = R_L C_L \tag{4.28}$$
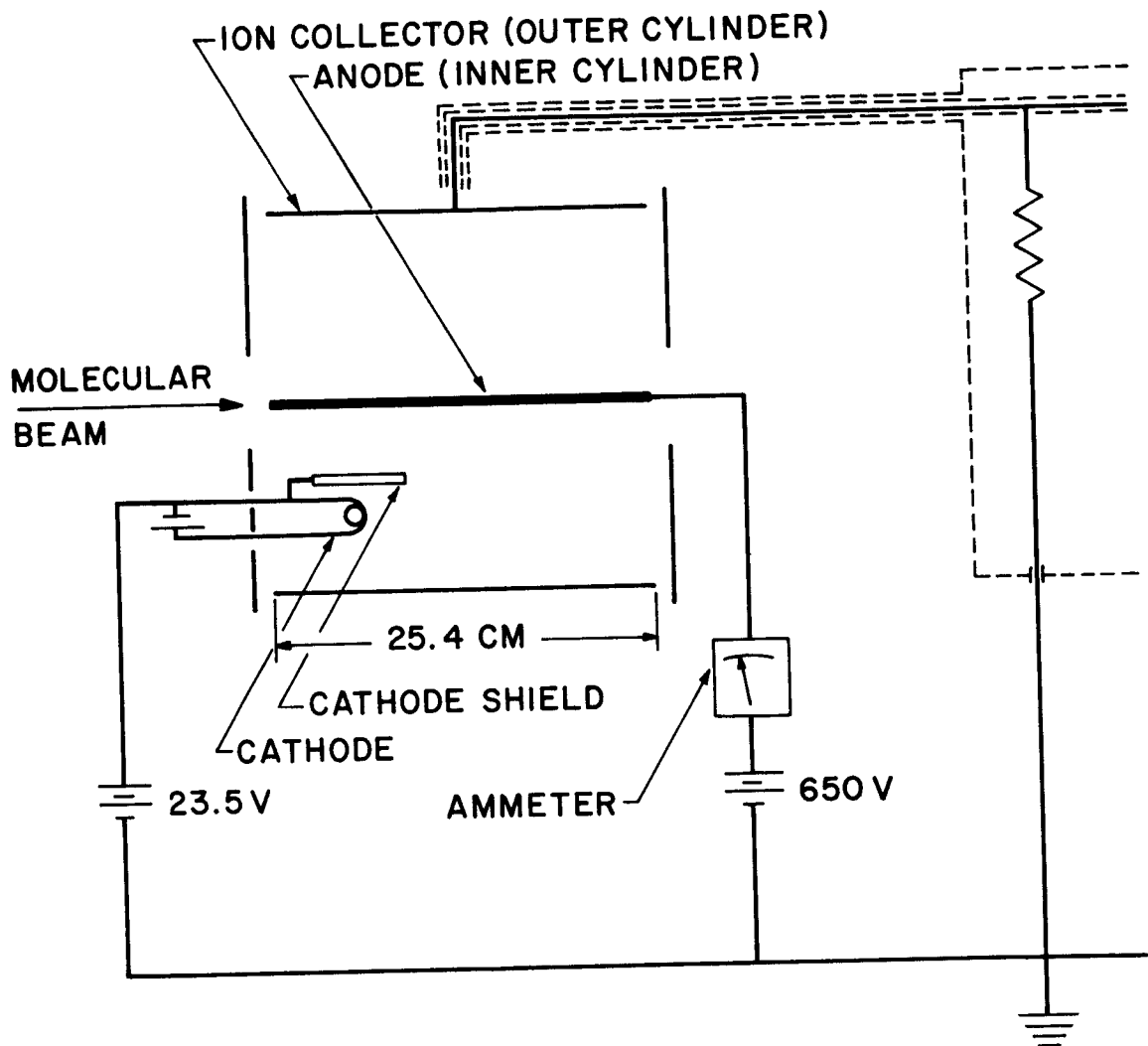
SCHEMATIC DIAGRAM OF MODIFICATION OF THE
ORBITRON PRESSURE GAUGE

FIGURE 4.3

its effect would be included in the detector characteristic function $g_d(t)$ determined during calibration.

In any event, the effective capacitance does not affect the interpretation of results which involve only the zeroth moment of the ion current $I^+(t)$ since the zeroth moment of the signal processing operator, g_s, is unity. Therefore

$$\mu_o\{V(t)\} = \mu_o\{g_s\}\ \mu_o\{I^+(t)\} = \mu_o\{I^+(t)\} \qquad (4.29)$$

Physically, this means that capacitance is not a <u>source</u> of electrostatic charge and does not contribute, therefore, to the total charge carried by a pulse. Note, however, that the peak height of the signal is affected by capacitance.

b) The steady current, a measure of the density of the background molecules, is indicated by a Keithley 610 A electrometer. This instrument is connected between the low-potential end of the load resistor and ground.

The use of the Northern Scientific NS-513 digital memory oscilloscope, the generation of a triggering signal for the various oscilloscopes and the Hewlett Packard pulse counter, and the use of the x-y recorder have been described elsewhere.[23-24] These components either are passive or have a rise time much smaller than characteristic times of concern here.

Calibration of the Orbitron Detector

Calibration of a detector means the determination of the transfer function, $g_d(t)$, of the detector. The method is suggested by Equations (4.3). An effusive oven beam is modulated by a chopper whose admittance function is known. The speed distribution of the beam is assumed to be Maxwellian at the measured temperature of

the oven. Hence the instantaneous rate $dN(t)/dt$ and density $n(t)$ at the entrance of the detector can be determined. (See Chapter III and Appendix C). The transfer function is by definition the function relating the measured ion current to $dN(t)/dt$ and $n(t)$.

To simplify the analysis of the data, the purely non-through-flow approximation of a linear detector is adopted. The approximation is tested by applying the criterion expressed by Equation (4.24). In the calibration, described in detail here, accuracy of the data warranted calculation of the zeroth, first and second moments of $g_d(t)$. The first three moments of the recorded signal traces were determined by means of a special planimeter designed to measure all three moments simultaneously. The corresponding moments of $I^+(t)$ were extracted by multiplying by the appropriate amplification and scaling factors of the current-to-voltage trans-ducer (load resistor), voltage amplifier, signal averager and x-y recorder. Table 4.1 lists the moments of $I^+(t)$ for a series of calibration runs for the Orbitron detector shown in Figure 4.2. Calibration of one of the earlier versions of the Orbitron detectors was reported in Reference 23. Figure 4.4 illustrates the arrange-ment of the detector with respect to the chopper, while Table 4-2 lists some of the measured constant parameters related to the modulation process and the beam.

The following equations were used to analyze the data.

a) The steady state density of a beam effusing from an oven through an orifice of Area A at a distance L_{CD} measured along the axis of the orifice is given by

$$n_b = A_{so} \, n_s / 4 \pi L_{od}^2 \tag{4.30}$$

where n_s is the density of the gas in the oven.

TABLE 4.1

CALIBRATION OF ORBITRON DETECTOR

1. Measurements at constant beam density.

Run No.	n_b (atoms/cm^3) x10^{-8}	$\mu_o[I^+(t)]$ (coulomb) x10^{13}	$\eta_1[I^+(t)]$ (second) x10^3	$\nu_2[I^+(t)]$ (sec^2) x10^7	$1/\omega$ (second) x10^2
11	7.28	17.6	1.665	1.81	5.00
12	"	14.02	1.45	1.50	4.08
13	"	11.74	1.30	1.45	3.38
14	"	10.18	1.17	1.45	2.86
15	"	8.25	1.075	1.28	2.36
16	"	8.68	1.01	1.26	2.08
17	"	6.43	0.96	1.22	1.82
18	"	5.71	0.90	1.17	1.58
19	"	5.02	0.864	1.11	1.42
20	"	17.6	1.67	1.98	5.00

2. Measurements at constant chopper speed.

Run No.	n_b	$\mu_o[I^+(t)]$	$\eta_1[I^+(t)]$	$\nu_2[I^+(t)]$	$1/\omega$
20	7.28	17.6	1.67	1.98	5.00
21	10.35	26.8	1.65	2.07	"
22	7.65	19.8	1.82	2.22	"
23	4.39	10.6	1.54	1.80	"
24	2.42	6.5	1.68	1.87	"
25	1.67	4.1	1.62	2.06	"
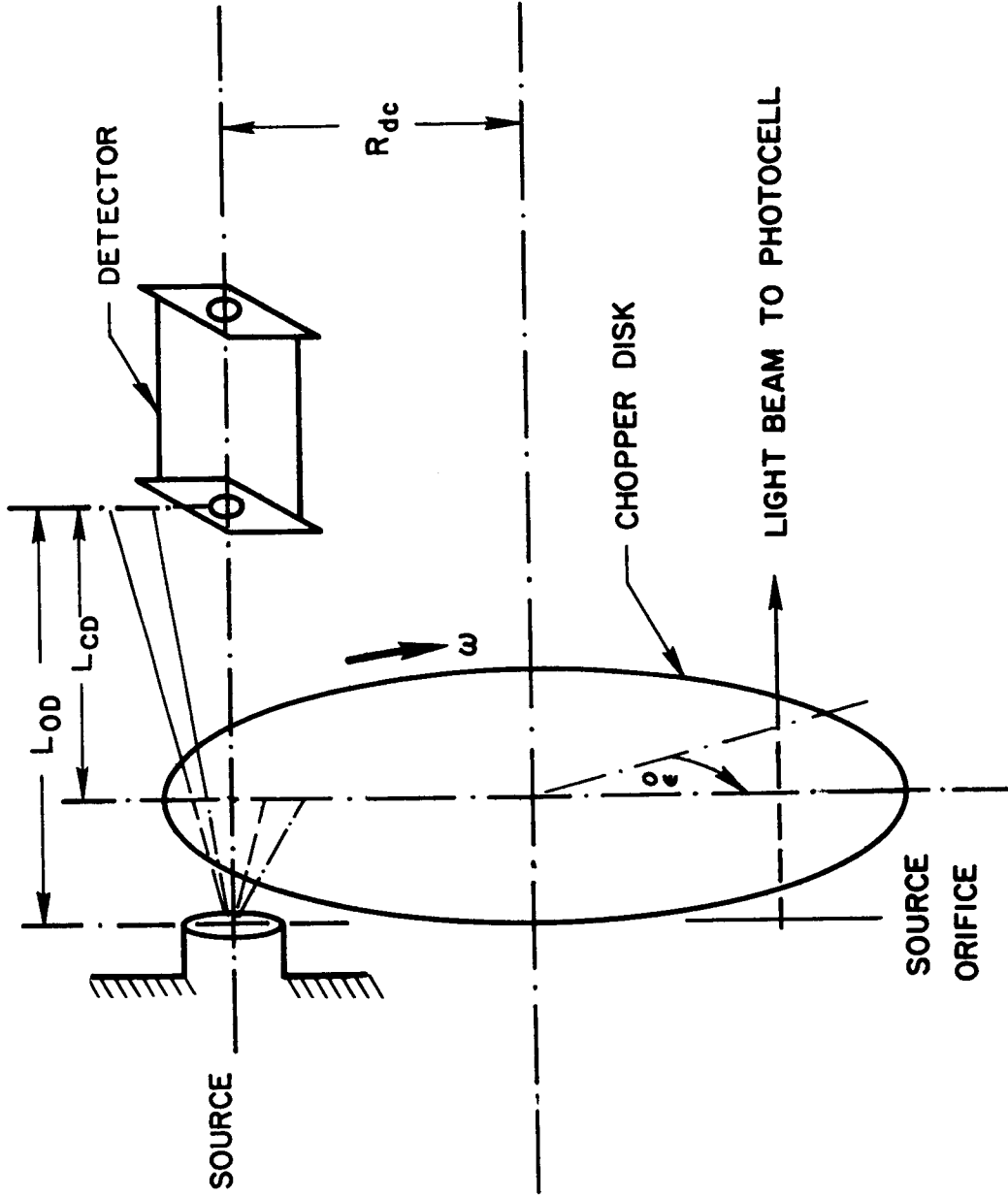
SCHEMATIC DIAGRAM OF THE RELATIVE POSITION OF THE
CHOPPER AND THE DETECTOR DURING CALIBRATION

FIGURE 4.4

TABLE 4.2

MEASURED AND DERIVED PARAMETERS, CALIBRATION
OF ORBITRON DETECTOR

Date: May 12, 1966

Diameter of detector orifice, d_{do}	0.952 cm
Area of detector orifice, A_{do}	0.71 cm^2
Distance between detector and chopper axes, R_{dc}	8.0 cm
Distance between detector and source orifices, L_{od}	10.0 cm
Distance of detector orifice from chopper disk, L_{cd}	8.0 cm
Source-orifice diameter, d_{so}	0.405 cm
Source-orifice area, A_{so}	0.129 cm^2
Chopper-slit aperture angle, $\overset{o}{\alpha}$	2°
Angle traversed by radial line on chopper disk across detector orifice, $\psi = d_{do}/R_{dc}$	0.119 rad
Angle traversed by radial line on chopper disk sweeping from photocell to detector orifice, $\overset{o}{\epsilon}$	4°
Most probable speed of Argon atoms in source chamber, $\gamma = (2kT/m)^{\frac{1}{2}}$	3.5x10^4 cm/ sec

The relation between $I^+(t)$ and $dN(t)/dt$ is given by Equation (4.23). The relation between $dN(t)/dt$ and $\phi(t)$ is given by Equation (4.8). Taking the moments of these two equations and combining them, one obtains

$$\mu_o\{I^+(t)\} = \gamma n_b \mu_o\{g_d(t)\} \, \mu_o\{A(t)\} \, \mu_o\{\phi(t)\} \tag{4.31a}$$

$$\eta_1\{I^+(t)\} = \eta_1\{g_d(t)\} + \eta_1\{A(t)\} + \eta_1\{\phi(t)\} \tag{4.31b}$$

$$\nu_2\{I^+(t)\} = \nu_2\{g_d(t)\} + \nu_2\{A(t)\} + \nu_2\{\phi(t)\} \tag{4.31c}$$

For a trapezoidal gate function the moments of $A(t)$ are given in Table 3.2. The moments of $\phi(t)$ are related to the speed distribution function $f_2(s)$ by Equations (A6.2) and (A6.5). The moments of the corresponding non-normalized $F_2(s)$ are tabulated for the case of interest ($S=0$) in Tables A1 - A4. Making all the necessary substitutions in Equations (4.31), one obtains

$$\mu_o\{I^+(t)\} = [2\gamma/(\pi)^{\frac{1}{2}}] \; n_b \; \overset{o}{\alpha} \; A_d/\omega \; \mu_o\{g_d(t)\} \tag{4.32a}$$

$$\eta_1\{I^+(t)\} = \eta_1\{g_d(t)\} + (L_{CD} \; \sqrt{\pi}/2\gamma) + (\overset{o}{\alpha} + \overset{o}{\psi})/2\omega + \Delta t_{tr} \tag{4.32b}$$

$$\nu_2\{I^+(t)\} = \nu_2\{g_d(t)\} + (L_{CD}/\gamma)^2(1-\pi/4) + (\overset{o}{\alpha}{}^2 + \overset{o}{\psi}{}^2)/12\omega^2 \tag{4.32c}$$

where

$$\Delta t_{tr} = \overset{o}{\epsilon}/\omega \tag{4.33}$$

is the time elapsed between the photocell trigger signal and $t = t_o$

The calibration runs, tabulated in Table 4.1, consist of two sets. In the first the steady beam density was held constant while the chopper angular speed was varied. The second set consists of runs at constant chopper angular speed and variable beam density.

Values of the zeroth, first and second moments of the ion current, obtained from the constant beam density runs, are plotted in Figures 4.5, 4.6, and 4.7 against the inverse of the rotor angular speed in the first two figures and against the square of that quantity in Figure 4.7. Values of the zeroth moment of the ion current, obtained from the runs at constant chopper speed, are plotted against the beam density in Figure 4.8.

As predicted by Equations (4.32), straight lines were drawn through the data points in all four figures. Table 4.3 lists the slope and intercept of the straight line in each figure. The intercepts of the straight lines in Figures 4.5 and 4.8 are zero as predicted by Equation (4.31a). By equating the experimental slopes and intercepts to the corresponding analytical expressions given by Equations (4.32), values of the first three moments of the function $g_d(t)$ were obtained. These also are listed in Table 4.3. An additional value of the second central moment of $g_d(t)$ was obtained by averaging the values from the runs at constant chopper speed. The average value thus obtained was $10.4 \times 10^{-8} (\sec^2)$.

The adopted values for the moments of $g_d(t)$ are :

zeroth: $(3.2 \pm 0.2) \times 10^{-22}$ coulomb/molecule

first: 3.1×10^{-4} second

second: $10.2 \times 10^{-8} (\text{second})^2$

Note that the criterion, expressed by Equation (4.24), for validity of an exponential form of $g_d(t)$ is fulfilled remarkably well. The characteristic dynamic function $g_d(t)$ of this Orbitron detector is given therefore by

$$g_d(t) = \mu_o \{g_d(t)\} \exp(-t/\tau)$$
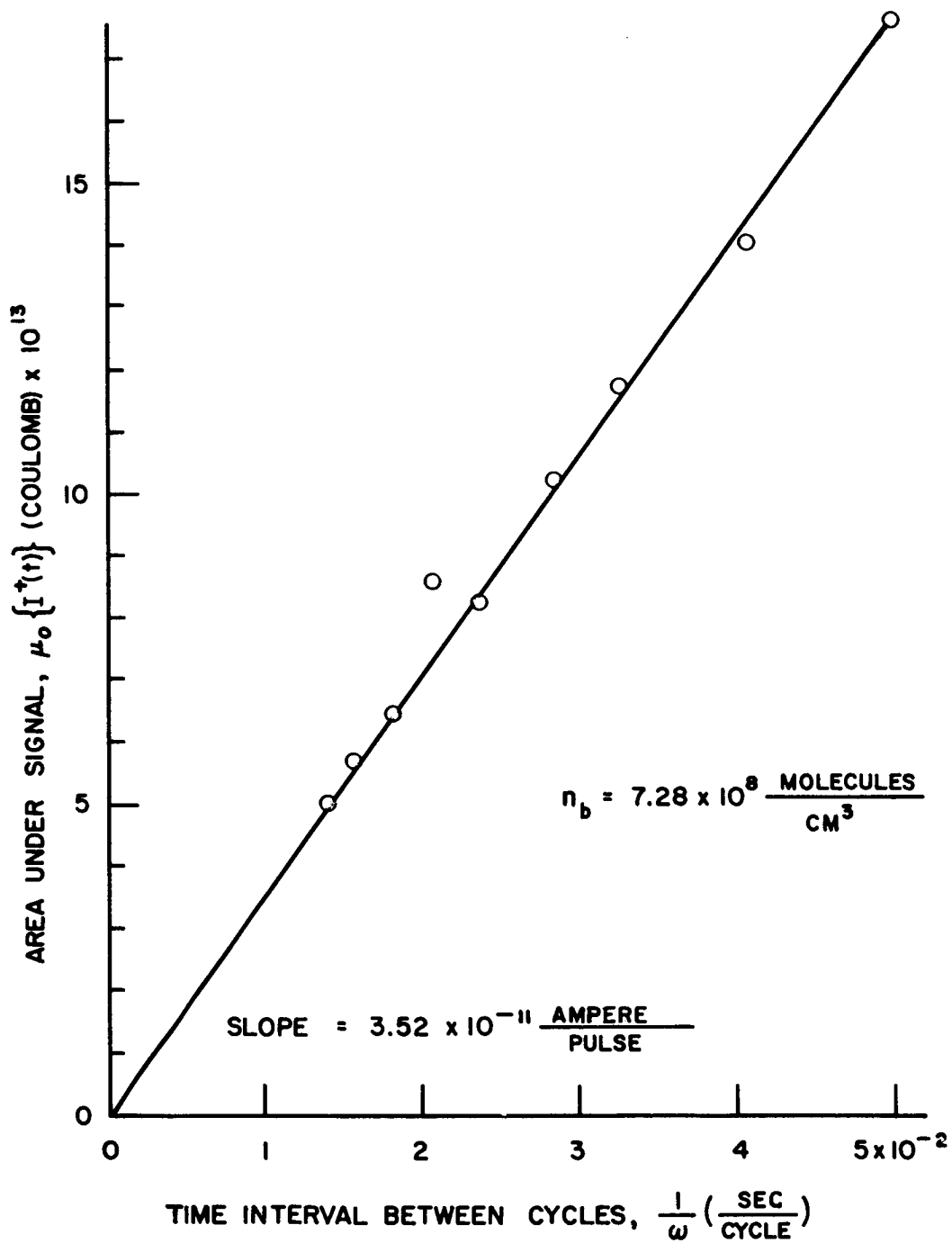
INTEGRAL OF ION-CURRENT SIGNAL AS A FUNCTION OF
INVERSE CHOPPER FREQUENCY

FIGURE 4.5
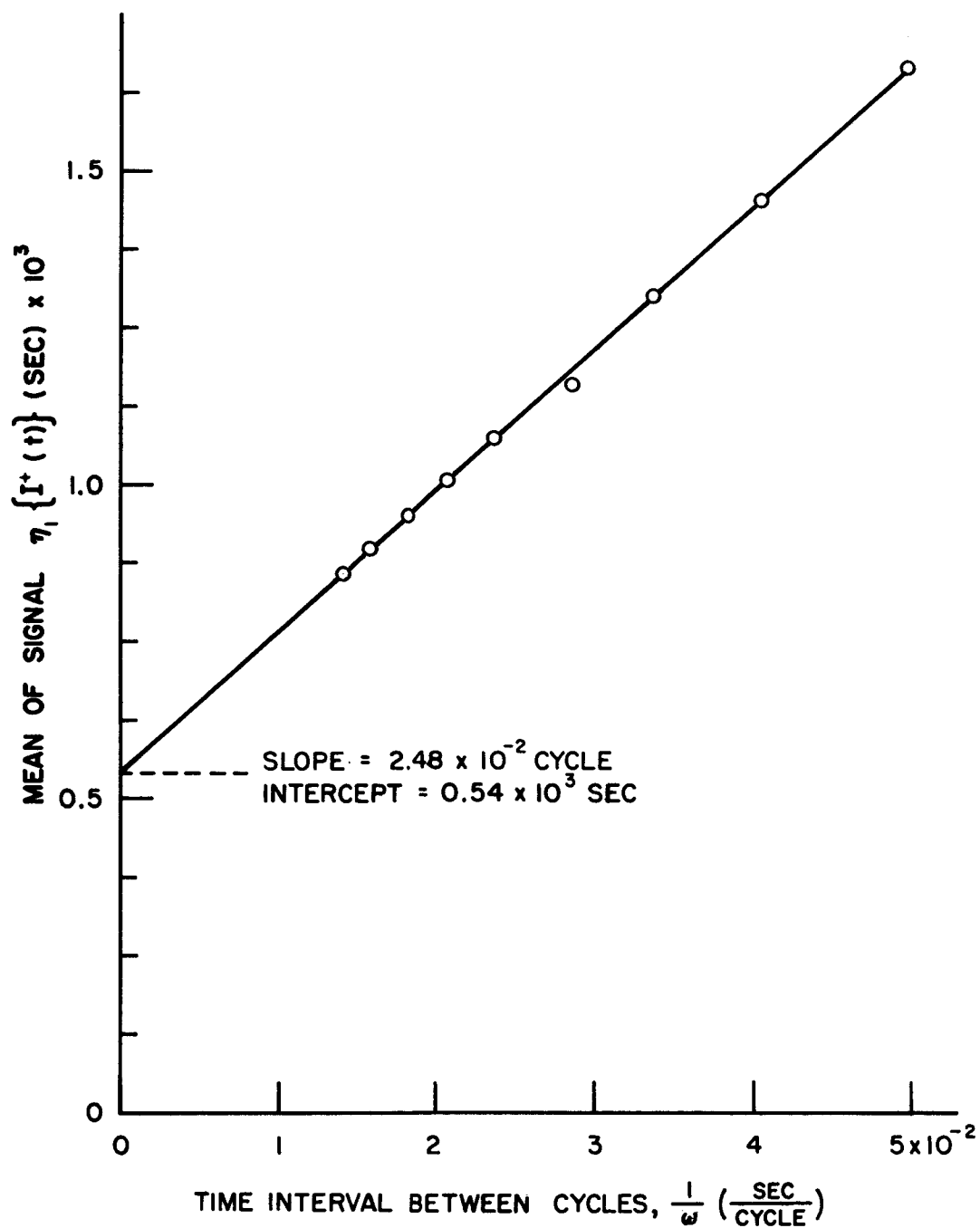
MEAN OF ION-CURRENT SIGNAL AS A FUNCTION OF
INVERSE CHOPPER FREQUENCY

FIGURE 4.6
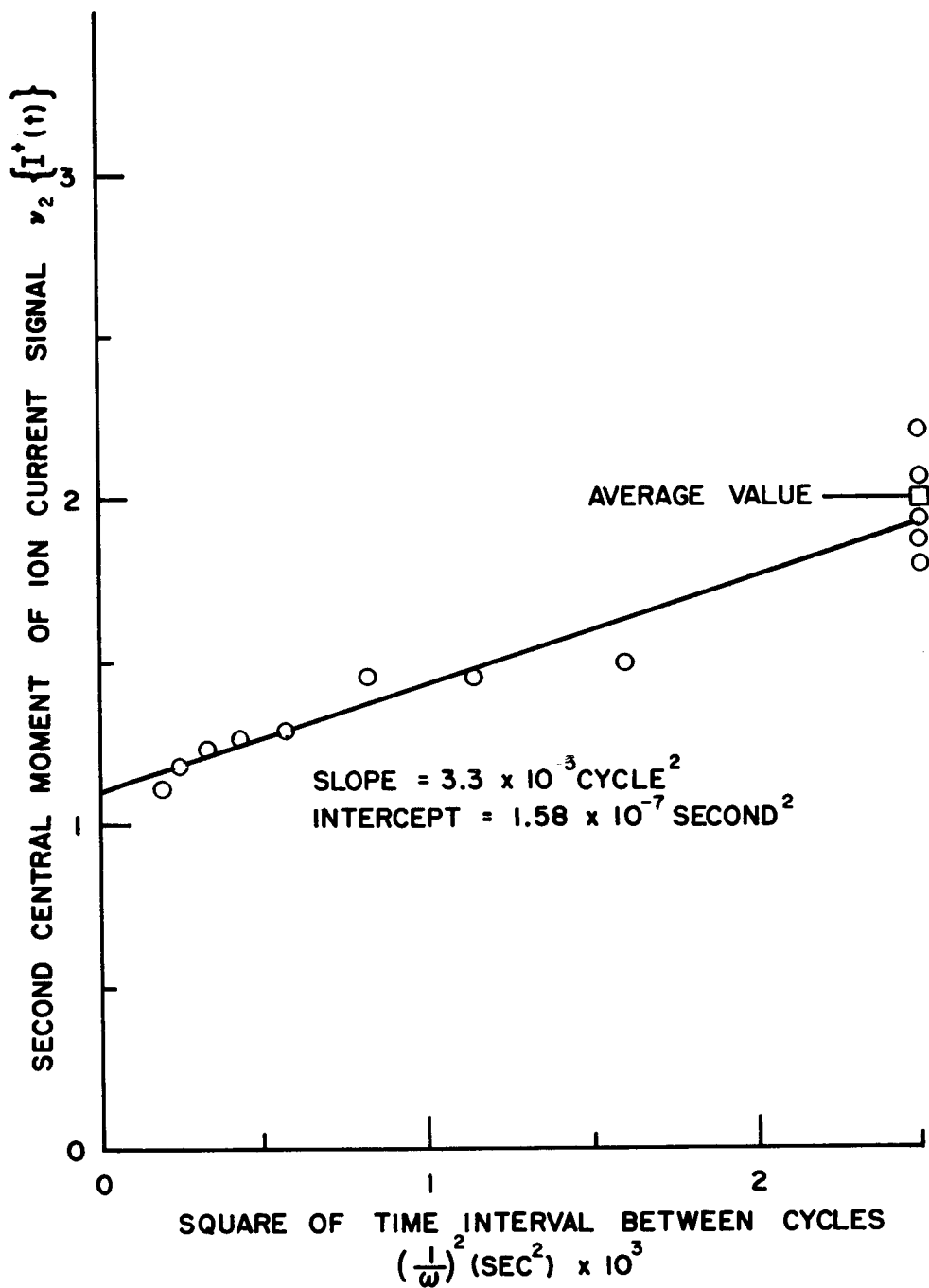
SECOND CENTRAL MOMENT OF ION-CURRENT SIGNAL AS A
FUNCTION OF SQUARE OF INVERSE CHOPPER FREQUENCY

FIGURE 4.7

$$\frac{1}{\omega} = 5 \times 10^{-2}\left(\frac{\text{SECOND}}{\text{CYCLE}}\right)$$

SLOPE $= 2.61 \times 10^{-21}$ $\dfrac{\text{COULOMB CM}^3}{\text{MOLECULE}}$

AREA UNDER SIGNAL, $\mu_o\left\{I^+(t)\right\}$ (COULOMB) $\times 10^{13}$

OVEN BEAM DENSITY, n_b $\left(\dfrac{\text{MOLEC.}}{\text{CM}^3}\right) \times 10^{-8}$
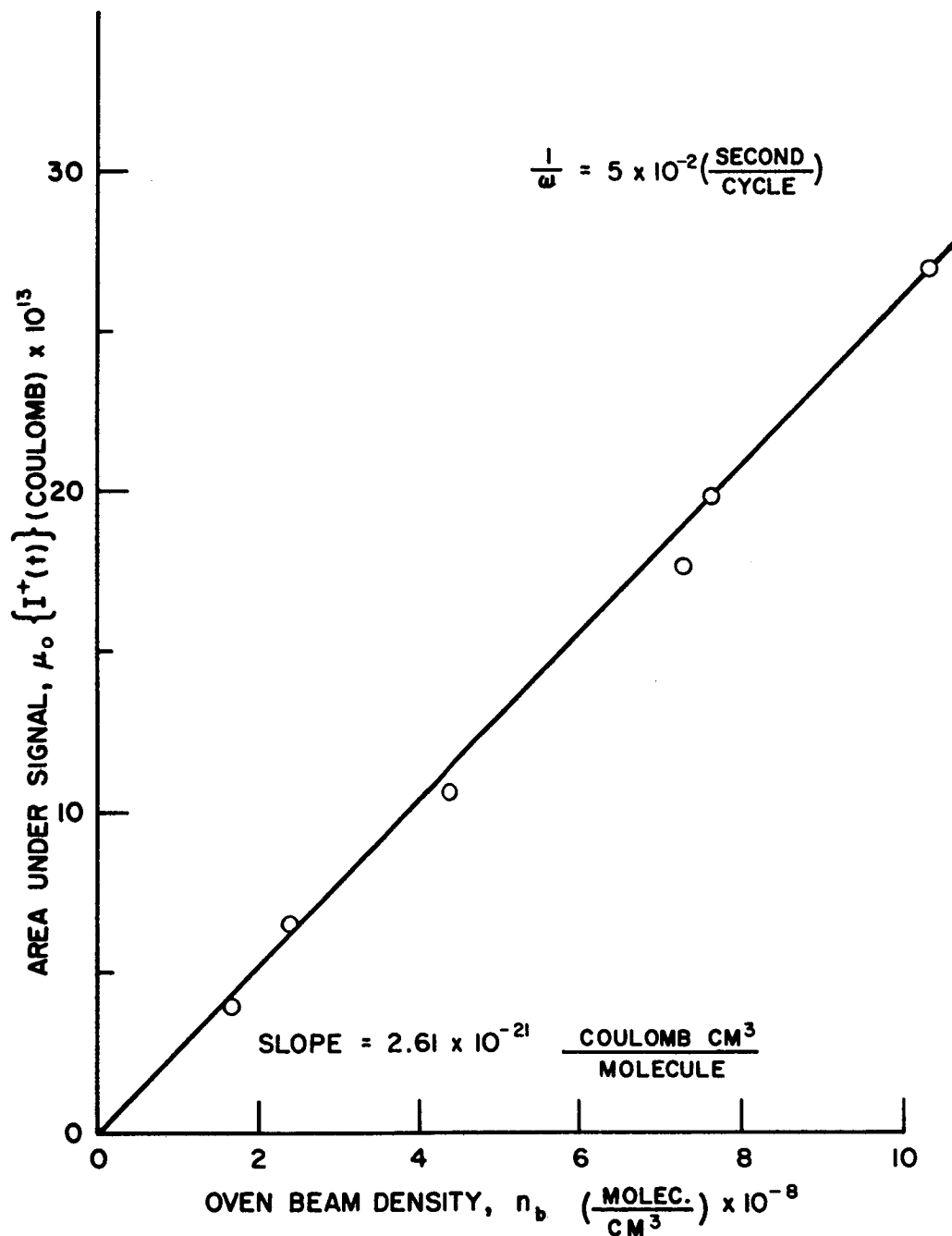
INTEGRAL OF ION-CURRENT SIGNAL AS A FUNCTION OF
BEAM DENSITY

FIGURE 4.8

TABLE 4.3

SLOPES AND INTERCEPTS OF FIGURES 4.5 TO 4.8 AND
RELATED CALCULATED QUANTITIES

Slope or Intercept	Measured Value	Equation	Calculated Quantity*
$\left[\dfrac{d\mu_o\{I^+(t)\}}{d(1/\omega)}\right]_{n_b}$	3.52×10^{-11} (amp)	4.32a	$\mu_o\{g_d(t)\} = 3.1 \times 10^{-22} \dfrac{coulomb}{molecule}$
$\left[\dfrac{d\mu_o\{I^+(t)\}}{dn_b}\right]_{\omega}$	$2.61 \times 10^{-21} \dfrac{coulomb}{molecule/cm^3}$	4.32a	$\mu_o\{g_d(t)\} = 3.35 \times 10^{-22} \dfrac{coulomb}{molecule}$
$\left[\dfrac{d\eta_1\{I^+(t)\}}{d(1/\omega)}\right]_{n_b}$	2.48×10^{-2} (cycle)	4.32b	slope = 2.34×10^{-2} (cycle)
$\eta_1\{I^+(t)\}\big]$ @ $1/\omega = 0$	5.4×10^{-4} (second)		$\eta_1\{g_d(t)\} = 3.1 \times 10^{-4}$ (sec)
$\left[\dfrac{d\nu_2\{I^+(t)\}}{d(1/\omega^2)}\right]_{n_b}$	3.3×10^{-5} (cycle)^2	4.32c	slope = 3.24×10^{-5} (cycle)^2
$\nu_2\{I^+(t)\}\big]$ @ $1/\omega = 0$	1.58×10^{-7} (second)^2		$\nu_2\{g_d(t)\} = 1.02 \times 10^{-7}$ (sec^2)

* Moments are calculated using listed slope or intercept and listed equation. Slopes are calculated using angles listed in Table E2.

with the value of the zeroth moment given above and τ given by the arithmetic average of the first moment and the square root of the second central moment of $g_d(t)$

$$\tau = 3.2 \times 10^{-4} \text{ second}$$

The through-flow ionization sensitivity, K, defined by Equation (4.6) is calculated from the following equation:

$$\mu_o\{g_d(t)\} = \tau K/V_d$$

where V_d, the volume of the ionization cavity, was 20 cm^3 for this design of the Orbitron. One finds

$$K = 2.0 \times 10^{-17} \text{amp}/(\text{molecule}/\text{cm}^3)$$

Since this Orbitron was operated at an emission current of 2.7×10^{-3} amperes and the ionization cross section for Argon is about 2.3×10^{-16} cm^2/atom, the mean electron-path length is:

$$\overline{\ell} = K/\sigma I^- = 44 \text{ cm}$$

Summary

In this chapter:

1. The dynamic characteristics of the detection process are analyzed and defined in terms of design and operational parameters.

2. The concepts "through-flow mode" and "non-through-flow mode" of operation are defined as idealized reference points in a continuous range of possible modes of operation.

3. The general class of linear detectors is defined in terms of linear operator theory (see Appendix B), and subclasses (such as equilibrium detector) are discussed.

4. Possible distortional effects of the signal processing gear are examined critically. It is concluded that such effects would be accounted for by a proper calibration procedure, and that the effect would be of no importance in interpretations relying only on measurement of the zeroth moment of $I^+(t)$.

5. The design considerations and characteristics of the Orbitron detector are presented and discussed.

6. The detector was calibrated by a novel procedure based on the analysis of linear detectors. Variation of the modulation frequency during calibration provided a method of determining the characteristic moments of the detector calibration function. The Orbitron was found to behave in a purely non-through-flow mode with a characteristic time of 3.2×10^{-4} second, a through-flow ionization sensitivity $K = 2.0 \times 10^{-17}$ amp/(molecule/cm^3) and a mean path length of ionizing electrons of 44 cm. The effective overall sensitivity of the Orbitron detector was (3.2 ± 0.2) $\times 10^{-22} \frac{coulomb}{molecule}$.

CHAPTER V
## RESULTS AND DISCUSSION OF RESULTS

Experimental Results

Spatial distributions of the flux of argon atoms scattered from various silver, mica and brass surfaces are presented in Figures 5.1 to 5.5. The units of the radial magnitude in these polar plots are arbitrary. They represent the zeroth moment (the area) of the ion current signal as measured from the x-y recordings of these signals. The zeroth moment of the ion-current pulse (see Equation 4.17) is proportional directly to the zeroth moment of the magnitude of the flux. The zeroth moment of the flux pulse is proportional directly to the total number of molecules in the pulse. Since the incident-beam pulse is a constant for measurements at all scattering angles, these polar plots represent the spatial distribution of the scattered-beam flux.

In order to indicate, for the silver target, the variation of the scattering distribution with the increase in time t since the end of the deposition period, one might wish to present this distribution for several values of t. However since only one detector was used, only one scattering angle could be monitored at any given t. Hence, cross plots were used. For a given value of the colatitude θ, a smooth curve was fitted through the several points on a plot of the zeroth moment of the recorded pulse versus t. See, e.g., Figure 5.6. From such plots for several values of θ, the scattering distributions for several values of t (e.g., Figures 5.1 and 5.2) were prepared. In order to study in greater detail the scattering between the surface normal and the incident beam, a series of measurements was made in which only this region was monitored (Figure 5.3).
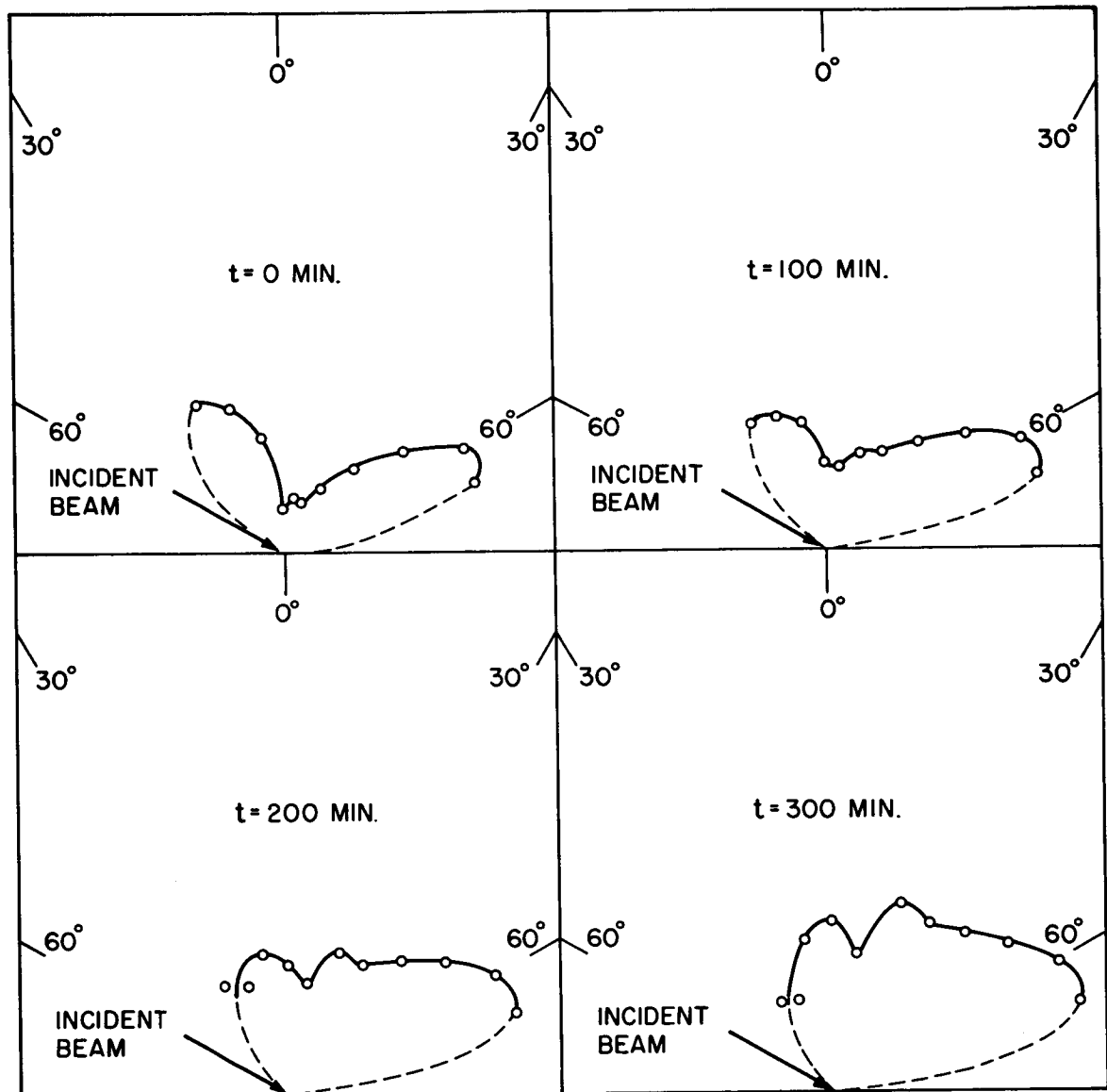
SCATTERING DISTRIBUTIONS FOR 1.0 EV ARGON BEAM
IMPINGING UPON SILVER SURFACE FOR SEVERAL
VALUES OF TIME SINCE END OF
SILVER-DEPOSITION PERIOD

FIGURE 5.1
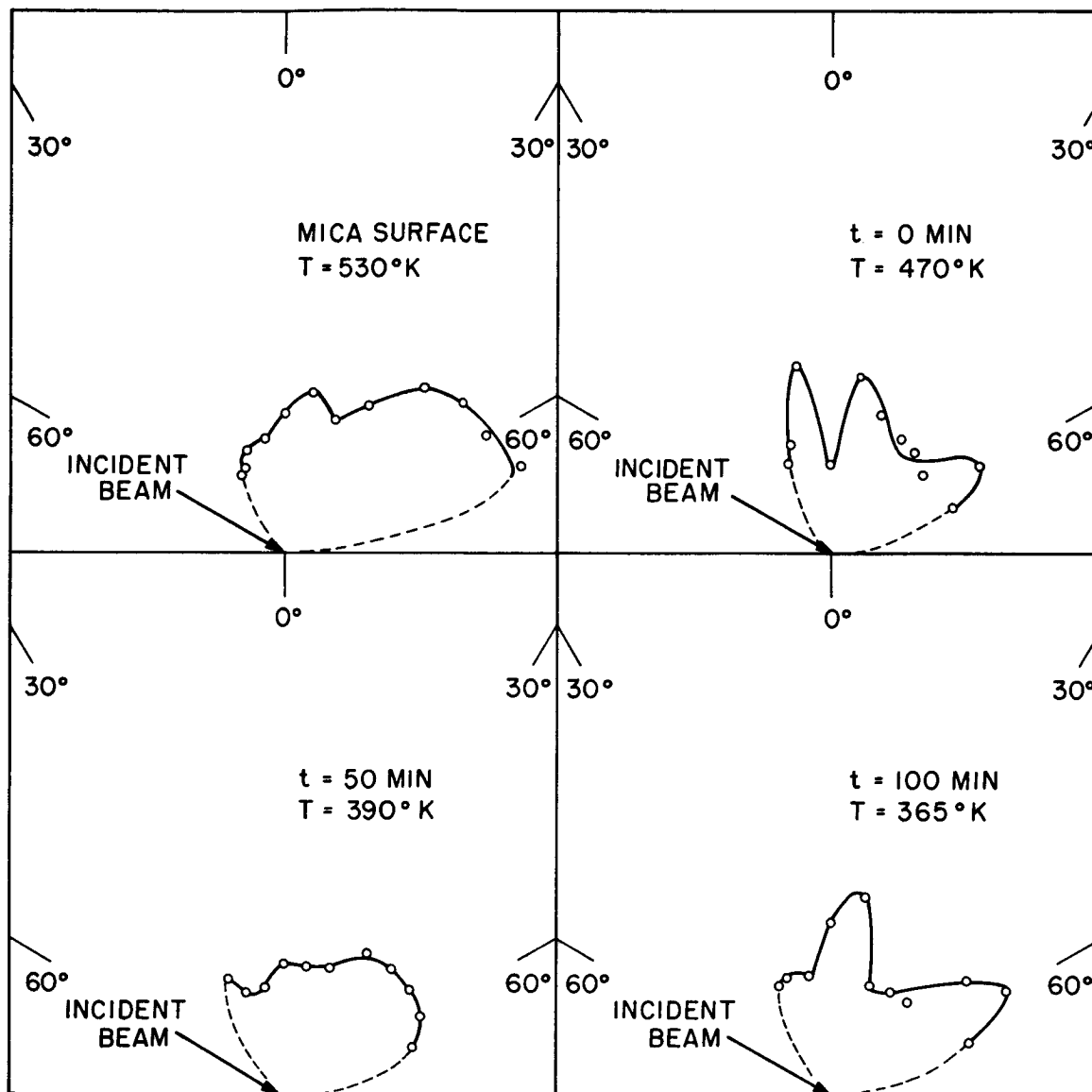

SCATTERING DISTRIBUTION FOR 1.2 EV ARGON BEAM
IMPINGING UPON MICA SURFACE AND UPON SILVER
SURFACE FOR SEVERAL VALUES OF TIME SINCE
END OF SILVER-DEPOSITION PERIOD

FIGURE 5.2
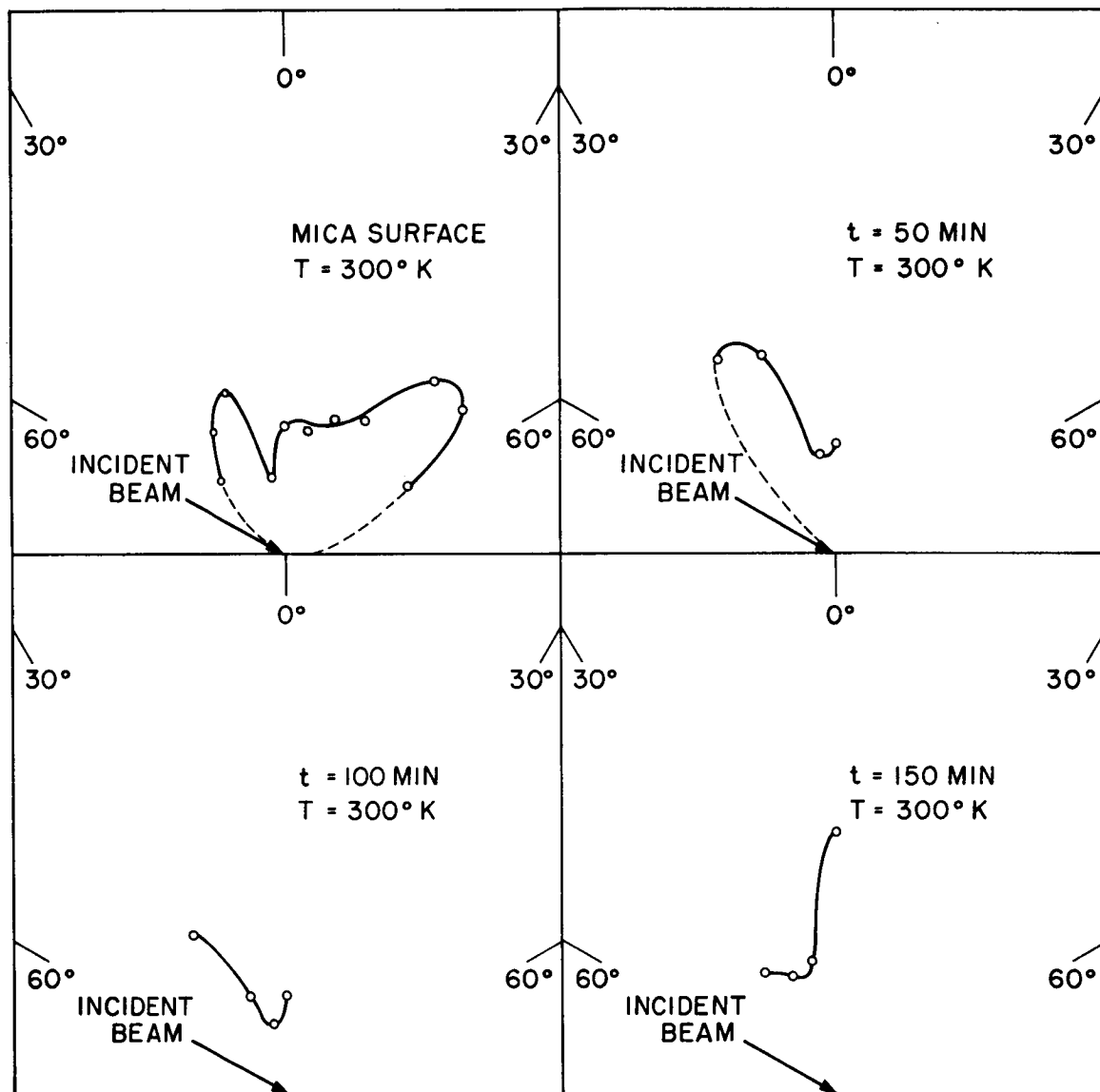
SCATTERING DISTRIBUTION FOR 1.2 EV ARGON BEAMS
IMPINGING UPON MICA SURFACE AND UPON SILVER
SURFACE FOR SEVERAL VALUES OF TIME SINCE
END OF SILVER-DEPOSITION PERIOD

FIGURE 5.3

0°

30°   30°

MICA SURFACE
T = 300° K

60°   60°

INCIDENT
BEAM
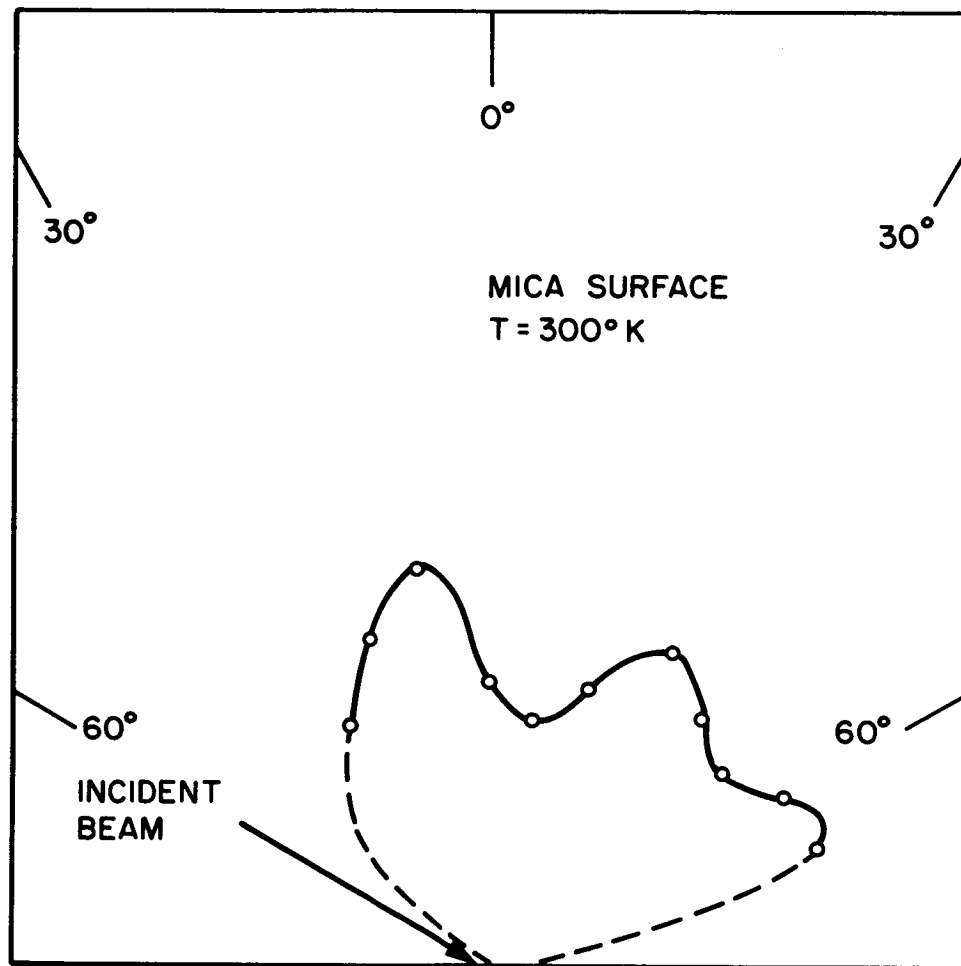
SCATTERING DISTRIBUTION FOR 1.2 EV ARGON BEAM
IMPINGING UPON MICA SURFACE AT 300°K

FIGURE 5.4
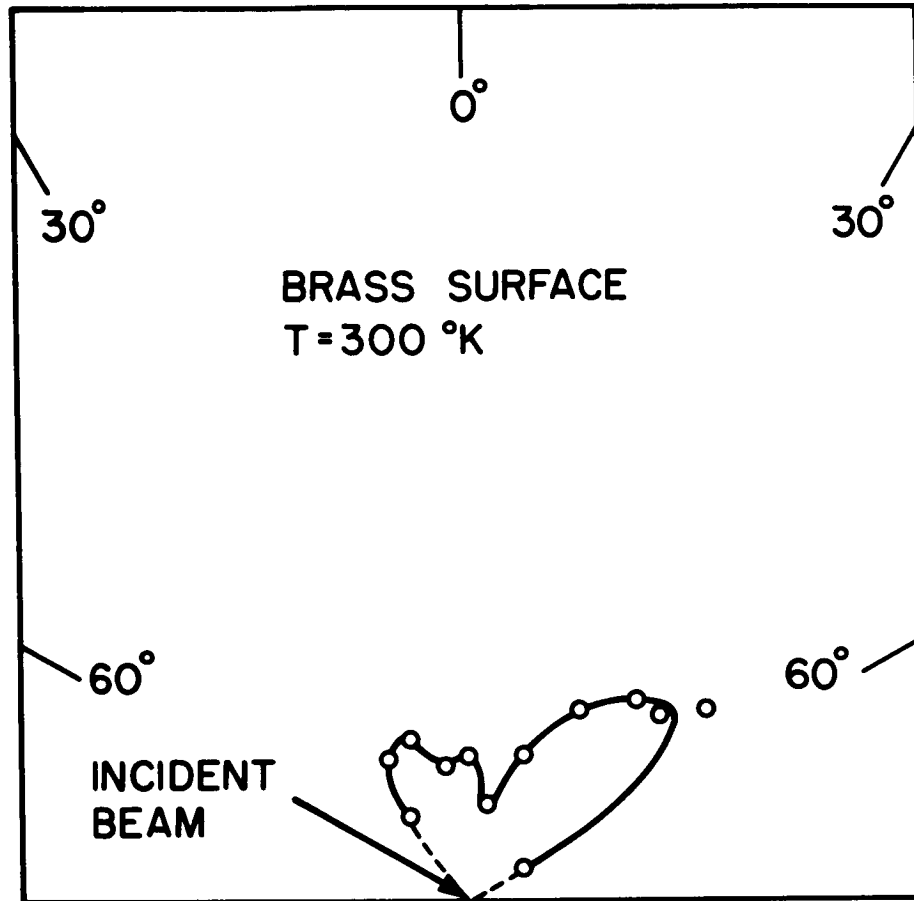
SCATTERING DISTRIBUTION FOR 0.6 EV ARGON BEAM
BRASS SURFACE

FIGURE 5.5

For comparison with the distributions of Figures 5.1 - 5.3 a distribution measured for the brass target is presented in Figure 5.5. The surface of this target was prepared (machined and polished) using standard shop techniques. No attempt was made to ensure a clean surface; the data were taken with the target at room temperature.

Measurements were made also for several values of ϕ and for two values (30° and 60°) of θ. See Figure 5.7.

The solid angle monitored by the detector was varied slightly by varying the distance from the target to the detector. For Figures 5.1, 5.2, 5.3, 5.5 and 5.7, the distances from the target to the detector were respectively 4.7, 3.0, 6.0, 3.8 and 3.5 cm. These variations are believed to affect negligibly the conclusions drawn here.

An examination of Figures 5.1 - 5.7 reveals:

a. The distributions are multiple-lobed for all targets investigated, even for the brass target. Within the accuracy of the present data, three lobes are observed. (For convenience, these three lobes will be called the back-scattering, the quasi-normal, and the quasi-specular lobes).

b. For mica at 530°K (Figure 5.2), $\eta \approx -10^{\circ}$ whereas for mica at 300°K (Figure 5.3) and brass at 300°K (Figure 5.5) $\eta \approx +15^{\circ}$, where η is the specular angle less the angle of the maximum of the quasi-specular lobe.

c. For the silver deposited at 525°K, (Figure 5.1), $\eta \approx -5^{\circ}$ whereas for the silver deposited at 500°K (Figure 5.2), $\eta \approx 0^{\circ}$.

d. For the silver, the strengths of the back-scattering and quasi-specular lobes decrease as t increases (Figures 5.1 and 5.2).
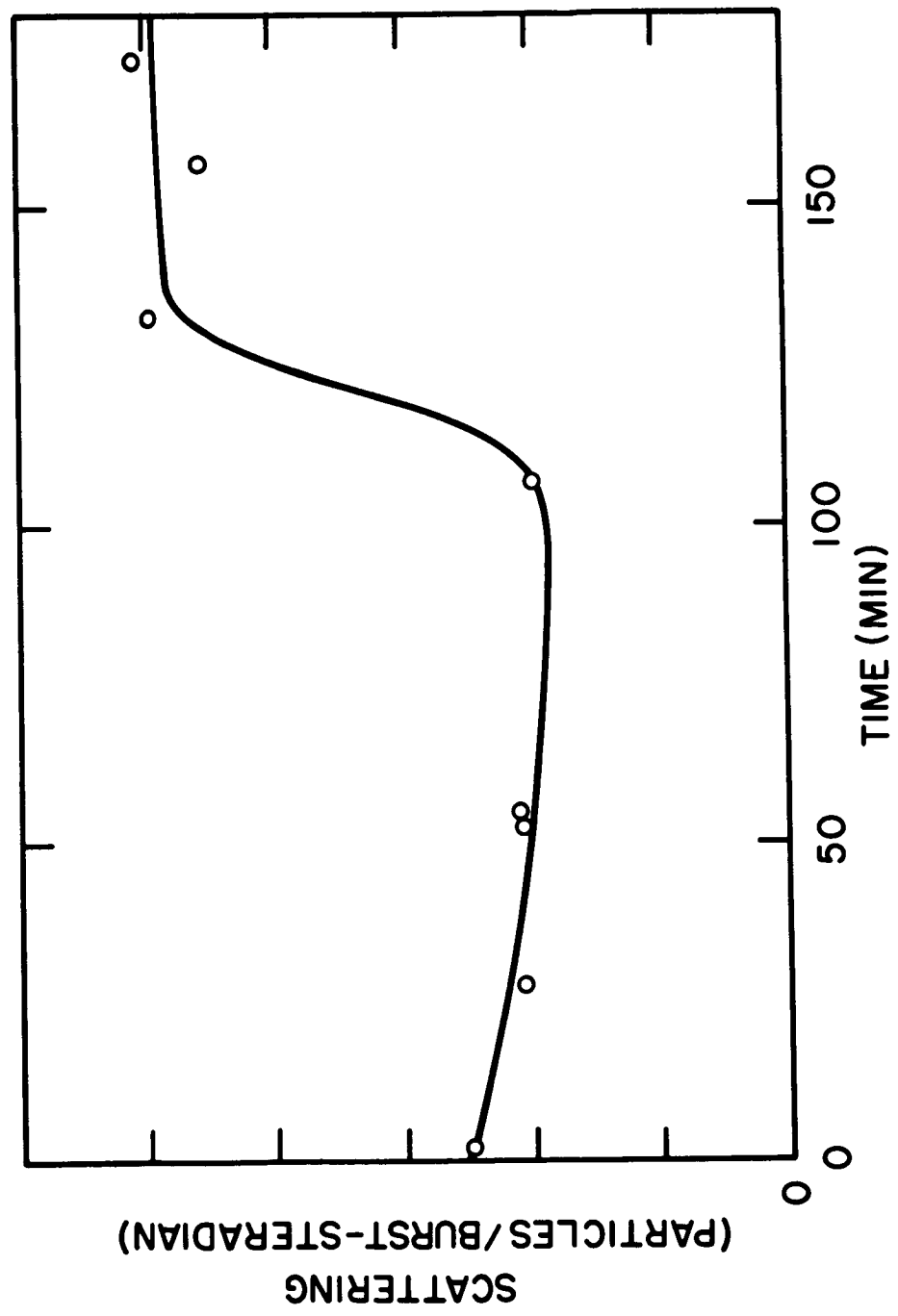
TYPICAL PLOT OF NUMBER OF PARTICLES SCATTERED PER
BURST INTO SOLID ANGLE SUBTENDED BY DETECTOR
VS TIME SINCE END OF SILVER-DEPOSITION PERIOD

FIGURE 5.6
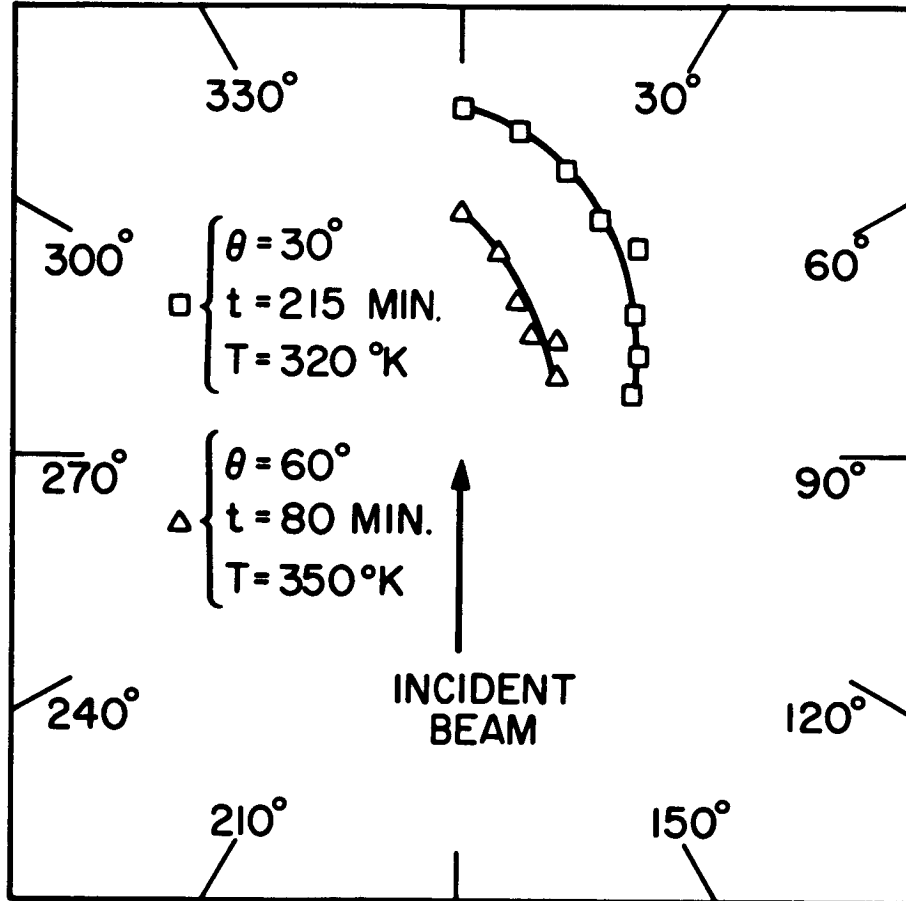
SCATTERING DISTRIBUTIONS FOR 1.2 EV ARGON BEAM
IMPINGING UPON SILVER SURFACE FOR TWO VALUES
OF THE COLATITUDE, θ

FIGURE 5.7

(Strength of a lobe is defined as the magnitude of the lobe maximum divided by the magnitude of the smaller of the two minimums). The strength of the quasi-normal lobe increases monotonically as t increases for the silver deposited at 525^OK (Figure 5.1), but decreases before it increases as t increases for the silver deposited at 500^OK (Figure 5.2).

e. As t increases, the back-scattering lobe moves toward the normal for silver deposited at 525^OK (Figure 5.1) and away from the normal for silver deposited at either 500^OK (Figure 5.2) or 300^OK (Figure 5.3).

f. Scattering in the quasi-specular lobe is concentrated near the $\phi = 0$ plane (Figure 5.7).

g. For silver, the number of particles scattered per burst in the hemispherical wedge defined by the origin and the area swept out by the entrance of the detector as its centerline moves in the $\phi = 0$ plane increases as t increases. See Figure 5.8, where integrals of the distribution curves of Figure 5.1 are plotted as a function of t. Table 5.1 summarizes some of the results.

For the purpose of ensuring that the multilobular pattern observed is not due to the detector characteristics, the exit orifice of the detector was closed. The characteristic time of the detector was increased. More importantly, all the molecules entering the ionization cavity had to suffer at least one collision with the detector walls before leaving the detector. The scattering pattern from mica at room temperature was not changed (Figure 5.4).

Discussion of Results

Examine Equations 2.2 and 2.3, keeping in mind that they are valid for the case when the incident beam is modulated. Since the
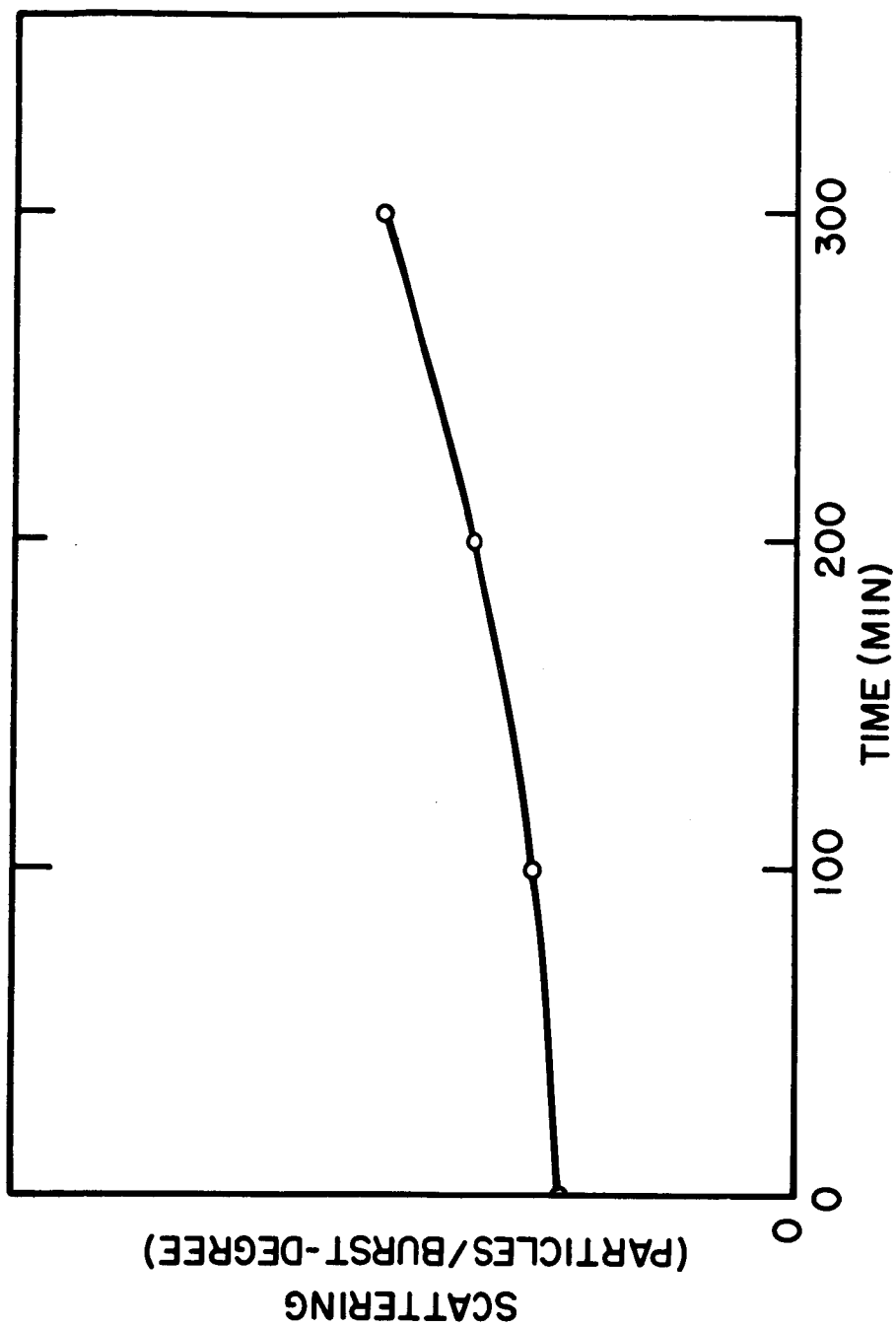
SCATTERING PER BURST NEAR $\phi = 0$ PLANE VS TIME
SINCE END OF SILVER-DEPOSITION PERIOD

FIGURE 5.8

TABLE 5.1

SUMMARY OF RESULTS OF SCATTERING EXPERIMENTS

Material	Temp. Depos. °K	Temp °K	Time min	Lobe No.	Maximum $\theta°$	$\phi°$	Minimum $\theta°$	$\phi°$	Lobe[b] Strength	Figure
Brass	—	300	—	1	45	0	10	0	2.98	11
				2	0	0			1.56	
				3	25	180	10	180	1.93	
Mica	—	530	—	1	70	0	20	0	2.5	7a
				2	10	0			1.7	
				3[a]	20	180	15	180	1.1	
Mica	—	300	—	1	45	0	15	0	2.8	8a
				2	5	0			1.45	
				3	20	180	10	180	2.1	
Silver			0	1	65	0	20	0	5.07	6a
				2	10	0			1.31	
				3	30	180	0	0	4.0	
Silver			100	1	65	0			2.87	6b
				2[c]			5	0		
	525			3	30	180			1.77	
Silver			200	1	65	0	30	0	2.24	6c
				2	20	0			1.36	
				3	15	180	10	0	1.30	
Silver			300	1	65	0	30	0	1.90	6d
				2	20	0			1.44	
				3	10	180	10	0		
Silver		470	0	1[d]	60	0	35	0	2.0	7b
				2	10	0			2.1	
				3	10	180	0	0	2.2	
Silver	500	390	50	1	50	0	15	0	1.6	7c
				2	0	0			1.3	
				3	25	180	15	180	1.3	
Silver		365	100	1	60	0	20	0	1.8	7d
				2	10	0			1.8	
				3	20	180	10	180	1.1	
Silver			50	3	30	180	10	180	2.42	8b
Silver	300	300	100	3	30	180	10	180	2.62	8c
Silver			150	2	0	0	15	180	2.14	8d
				3	30	180			1.15	

Notes: (a) This lobe is not well defined, probably due to lack of experimental points between $\theta = 10°$ and $\theta = 20°$.

(b) Lobe strength is defined as ratio of maximum intensity to intensity @ absolute minimum of polar plot.

(c) Second lobe is hardly noticeable.

(d) Peak is flat; θ_{max} is hard to determine.

incident beam is supersonic, the range of speeds is narrow, and it is reasonable to consider the operator g_{sc} to be linear, at least within the realized range of speeds.

Since the detector is non-through-flow, X_4 can be taken as the instantaneous molecular rate of incidence $dN_i(t)/dt$. The zeroth moment equation corresponding to Equation 2.2 is

$$\mu_o\{I^+(t, \vec{r})\} = \mu_o\{g_d(t)\}\, \mu_o\{g_{2tf}(t)\}\, \mu_o\{g_{sc}(t, \vec{r})\}\, \mu_o\{dN_i(t)/dt\} \quad (5.1)$$

Note that the zeroth moment of g_{2tf} is unity. Note also that the zeroth moment of the operator $g_{sc}(t)$ represents a fraction whose product with the number of particles in the incident burst yields the number of particles scattered along the vector $\vec{r}$. This is true as long as the surface is not a source (positive or negative) of particles. The source is negative (a sink) if some of the incident particles remain imbedded within the solid lattice. The surface is positive if some of the species from the surface separate and are counted in the scattered phase. This process is called sputtering or desorption, depending upon whether the sputtered species are characteristic of the lattice or of the environment.

The first-moment equation corresponding to II-2 is

$$\eta_1\{I^+_{sc}(t, \vec{r})\} = \eta_1\{g_d(t)\} + \eta_1\{g_{tf}[\,t, f_{sc}(t, \vec{v} \cdot \vec{r})\,]\}$$
$$+ \eta_1\{g_{sc}(t, \vec{r})\} + \eta_1\{dN_i(t)/dt\} \quad (5.2)$$

The incident rate $dN_i(t)/dt$ is sensed by means of the same ionization detector so that one can write

$$\eta_1\{I^+_i(t)\} = \eta_1\{g_d(t) + \eta_1\{dN_i(t)/dt\} \quad (5.3)$$

Combining Equations (5.2) and (5.3), one obtains

$$\eta_1\{I_{sc}^+(t,\vec{r})\} - \eta_1\{I_i^+(t)\} = \eta_1\{g_{tf}[\,t,f_{sc}\,(t,(\vec{v}\cdot\vec{r}))]\,\}$$

$$+ \eta_1\{g_{surf}(t,\vec{r})\} \qquad (5.4)$$

Define the symbol $\Delta\eta_1$

$$\Delta\eta_1 \triangleq \eta_1\{I_{sc}^+(t,\vec{r})\} - \eta_1\{I_i^+(t)\} \qquad (5.5)$$

Similarly one can write the second central moment equation

$$\Delta\nu_2 \triangleq \nu_2\{I_{sc}^+(t,\vec{r})\} - \nu_2\{I_i^+(t)\}$$

$$= \nu_2\{g_{tf}[\,t,f_{sc}(t,\vec{v}\cdot\vec{r})\,]\} + \nu_2\{g_{surf}(t,r)\} \qquad (5.6)$$

Consider now the case when

$$\eta_1\{g_{tf}\} \gg \eta_1\{g_{surf}\}$$

$$\nu_2\{g_{tf}\} \gg \nu_2\{g_{surf}\} \qquad (5.7)$$

where (for brevity) the functional dependence (brackets) of the g's are omitted. Further, assume that the speed distribution of particles in the direction determined by $\vec{r}$ is

$$f(s) = \frac{s^2 \exp - (s-S)^2}{\mu_o\{s^2 \exp - (s-S)^2\}} \qquad (5.8)$$

where

$$s = \frac{\vec{v}\cdot\vec{r}}{\gamma} \qquad (5.9)$$

and

γ = most probable speed due to random
kinetic motion.

S = ratio of the hydrodynamic (directed)
speed to the most probable speed γ.

Both γ and S depend implicitly on $\vec{r}$. Note that in the special case

of diffuse scattering the following relations apply:

a) $S = 0$ for all $\vec{r}$ (5.10)

b) $\gamma = (2kT/m)^{\frac{1}{2}}$ for all $\vec{r}$ (5.11)

c) T does not vary with $\vec{r}$ (5.12)

When the constraints (5.7) are satisfied and the speed distribution is given by (5.8), Equations (5.5) and (5.6) can be combined to give

$$\frac{\Delta \eta_1}{(\Delta \nu_2)^{\frac{1}{2}}} = \frac{\eta_1 \{g_{tf}\}}{\nu_2^{\frac{1}{2}} \{g_{tf}\}} \tag{5.13}$$

As shown in Chapter III, the right-hand side of Equation (5.13) is a function of S only (see Equation 3.26) so that

$$\frac{\Delta \eta_1}{(\Delta \nu_2)^{\frac{1}{2}}} = \frac{1}{\Omega^{\frac{1}{2}}(S)} \tag{5.14}$$

$\Omega(S)$ (see Figure 3.1) is a monotonically decreasing function of S. Therefore, $\dfrac{\Delta \eta_1}{(\Delta \nu_2)^{\frac{1}{2}}}$ is a monotonically increasing function of S. It approaches S for large values of S. Hence, a spatial distribution of the speed ratio of the scattered molecular field can be obtained by measuring the three first moments of the modulated scattered field.

Figure 5.9 is a polar plot of $\dfrac{\Delta \eta}{(\Delta \nu_2)^{\frac{1}{2}}}$ versus θ in the plane of incidence for scattering from a mica surface at $300^{\circ}K$. (The corresponding flux distribution is given in Figure 5.3).

From Figure 5.3 one might conclude that atoms scattered into solid angles centered around $\theta = 0^{\circ}$, 30°, and 60° suffer a smaller proportion of inelastic collisions than atoms scattered into other
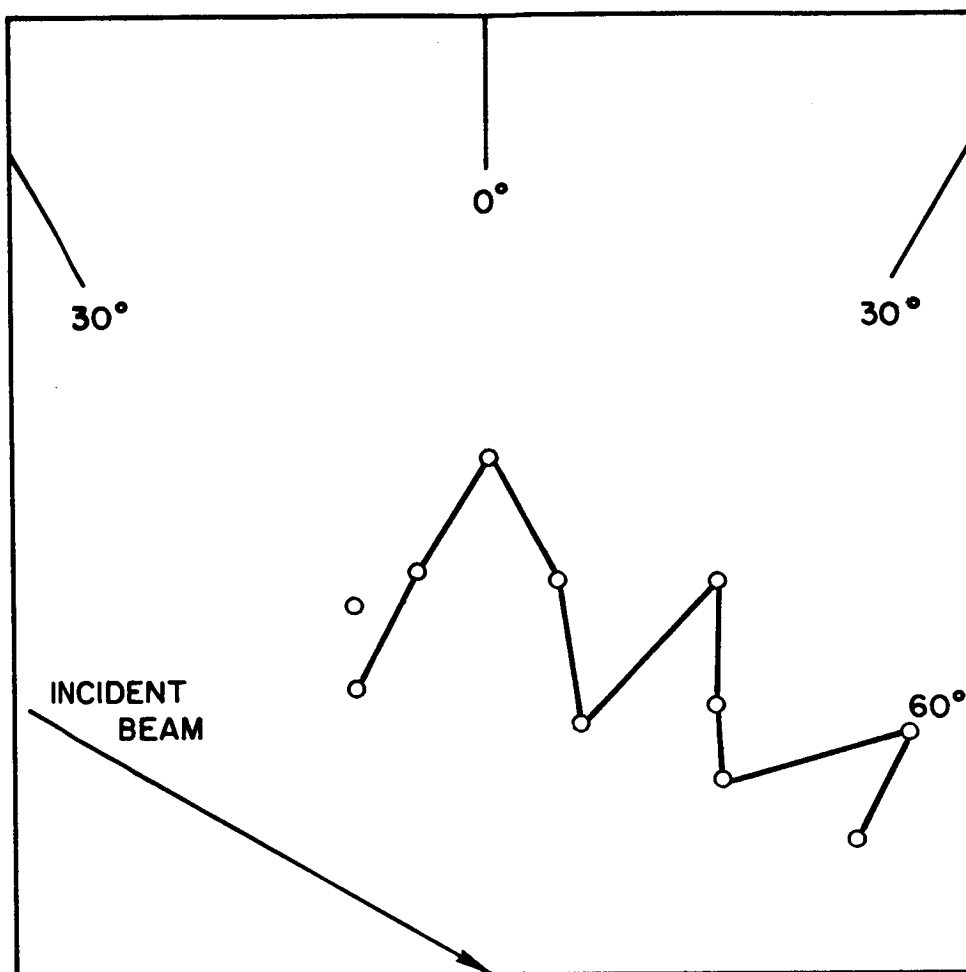
POLAR DISTRIBUTION OF HYDRODYNAMIC SPEED RATIO

FIGURE 5.9

solid angles. If one tries, however, to calculate the actual values of S from Equation (5.14), one finds that imaginary values of S are obtained. In fact, the minimum value of $\Omega^{-\frac{1}{2}}(S)$ corresponding to S = 0 (see Figure 3.1) is 1.92, while the values of $\Omega^{-\frac{1}{2}}(S)$ plotted in Figure 5.9 range from 0.68 to 1.35. Possible explanations for this are:

a) The detector characteristic time $\tau_d \doteq \eta_1\{g_d(t)\}$ is different when it is used to measure the scattered molecular field than when it is used to measure a collimated incident beam. In that case, a time difference $\Delta\tau_d \doteq \tau_{dsc} - \tau_{di}$ should be added to the right hand-side of the Equation (5.4). Also, since the characteristic function $g_d(t)$ of the detector was determined to be exponential, a quantity $(\Delta\tau_d)^2$ should be added to the right hand side of Equation (5.6). Equation (5.14) then should be modified as follows:

$$\frac{\Delta\eta_1 - \Delta\tau_d}{(\Delta\nu_2 - \Delta\tau_d^2)^{\frac{1}{2}}} = \frac{1}{\Omega^{\frac{1}{2}}(S)} \qquad (5.15)$$

If one substitutes into (5.15) a value of 1.92 for $\Omega^{-\frac{1}{2}}(S = 0)$ and the values of $\Delta\eta_1$ and $\Delta\nu_2$ corresponding to the smallest value of $\Delta\eta_1/(\Delta\tau_2)^{\frac{1}{2}}$ from Figure 5.9, then $\Delta\tau_d$ is larger than $\Delta\eta_1$. Since this does not make physical sense, it cannot be the complete explanation for the cited problem. In fact, an exponential residence time function of the surface (as suggested by Eucken's formula for the thermal accommodation coefficient, see Reference 8) with sufficiently large values of mean residence time $\eta_1\{g_{surf}(t)\} \doteq \tau_{surf}$ is also insufficient to explain the problem. (This is so because an exponential $g_{surf}(t)$ is indistinguishable mathematically from an exponential $g_d(t)$.) This leaves us with the only remaining alternative:

b)   The incident beam sputters some of the adsorbed species. When a flash desorption process accompanies surface scattering, the resulting characteristic function of the surface can be expressed as follows: (See Figure 5.10).

$$g_{surf} = g_{sc} + g_{des} \tag{5.16}$$

$$\mu_j\{g_{surf}(t)\} = \mu_j\{g_{sc}(t, \vec{r})\} + \mu_j\{g_{des}(t, \vec{r})\} \tag{5.17}$$

$$j = 0, 1, \ldots$$

Here $\mu_o\{g_{des}(t, \vec{r})\}$ is the differential desorption yield, i.e., the number of surface atoms desorbed into a differential solid angle at $\vec{r}$ per unit incident particle. The resulting instantaneous current is the sum of the two contributions:

$$I^+_{surf}(t, \vec{r}) = I^+_{sc}(t, \vec{r}) + I^+_{des}(t, \vec{r}) \tag{5.18}$$

The contribution to the current due to desorbed species can be displaced in phase from the contribution from the scattered atoms because of the following reasons:

a)   The mass of the desorbed species is larger than the mass of the incident (or scattered) atom.

b)   The mean energy of the desorbed species is smaller than that of the scattered atoms.

c)   The characteristic time of desorption (i.e., the time interval between the departure of the desorbed species and impulsive excitation of the adsorbed layer) is significantly larger than the residence time of the scattered atoms.

Evidence that flash desorption is indeed a substantial contributing factor to some of the signals (especially in the case of
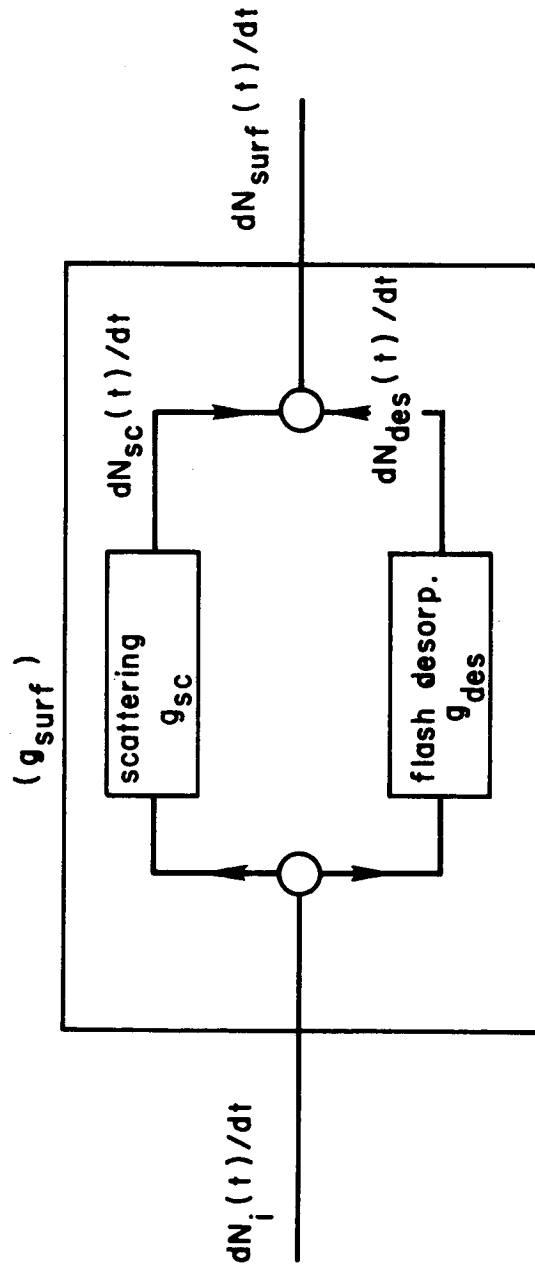
SIGNAL–FLOW DIAGRAM FOR THE COMBINED EFFECTS OF SCATTERING AND
FLASH DESORPTION ON A SURFACE

FIGURE 5.10

room-temperature surfaces) also is provided by the existence peaks in some of the signals.

If flash desorption is the answer to the dilemma raised above, can the multilobular patterns shown in Figures 5.1 to 5.5 also be attributed to this additive surface process? The answer to this question cannot be obtained in a conclusive fashion from the data presented here.

The distributions of scattering from silver deposited on cleaved mica (e.g., Figure 5.1) show, that the relative strengths of the back scattering and quasi-specular lobes decrease, whereas the strength of the quasi-normal lobe increases, as t, the time from the end of the silver deposition, increases. The scattering distribution appears to become more diffuse as t increases.

Distributions with multiple lobes have been observed by other investigators for diffractions of molecular beams from crystal surfaces (reviewed in Reference GR-VI), for sputtering of material from metal targets,[41] and for scattering of high-energy molecular beams from various surfaces.[6] Since a) the de Broglie wave length for a 1 ev Argon atom is two orders of magnitude smaller than the lattice constant for a silver crystal, b) all reported values of the sputtering threshold for argon impinging on silver are equal to or greater than 4 ev (Reference GR-VI, Table 10.3.1.1A) and c) the multiple lobes reported in Reference 6 coalesced into a single lobe as the beam energy was reduced to 100 ev, the multiple lobes reported here were not anticipated.

The strong quasi-specular lobe resembles in some respects the strongly non-diffuse single lobe reported for scattering of thermal-energy beams from relatively clean polycrystalline surfaces.[5, 18-19, 32-35] The location of the lobe maximum between

the specular direction and the target surface indicated in Figure 5.1 and in the upper left-hand quadrant of Figure 5.2 (a heated mica sur- face) also was observed for smooth polycrystalline surfaces[19] and for epitaxial surfaces.[33] A relatively simple (but physically appealing) collision model[26,27,37] also predicts such a displace- ment from the specular direction for relatively clean surfaces and sufficiently large values of the beam source temperature divided by the target surface temperature. The shift of the lobe maximum toward the surface normal indicated in the remaining three quadrants of Figure 5.2, the upper left-hand quadrant of Figure 5.3 (a room temperature mica surface) and Figure 5.5 (a room temperature brass surface) is also reported in References 33 and 19 for increases in roughness and/or contamination. However, for some of the polycrystalline and/or contaminated target surfaces here, com- pletely diffuse scattering should have been expected according to the reported results for thermal-energy beam scattering[5,17-19,33-35] instead of the strong quasi-specular lobes observed.

Note that three-lobed distributions cannot be obtained by adding two single lobed distributions. Hence at least one of these distributions would have to be multiple lobed. Either situation would be interesting and would warrant further study.

If a steady beam impinges on the target, the area of impact soon might be completely free of adsorbed species, particularly if the rate of desorption is higher than the rate of adsorption at the existing environmental conditions. In this case, use of a steady- state incident beam and modulation of the scattered field would provide uncoupled information about the scattered atoms alone. Application of the mass spectrometer, which was purchased recently by the laboratory, can provide a conclusive test of the desorption

hypothesis, and uncouple the flux distribution of scattered Argon atoms from other species.

CHAPTER VI
CONCLUSIONS AND RECOMMENDATIONS

Summary of Results

Scattering of modulated Argon atomic beams (with energies above 1 ev and hydrodynamic speed ratios of the order of 7) from cleaved mica and from vacuum-deposited silver on cleaved mica consistently showed a multilobular pattern on a polar flux diagram. Parameters varied during an extended series of experiments were a) surface temperature, b) time from deposition, and c) space coordinates. Both the incident-beam pulse and the scattered-beam pulse were detected and analyzed by novel methods. Expressions relating the recorded TOF signals to the speed distribution of the beam and the gate function of the chopper are derived and used to:

a) characterize the direct beam,

b) calibrate the detector by determining its dynamic characteristics.

c) analyze the signals of the scattered-beam pulse in terms of the incident-beam pulse, and

d) draw tentative conclusions about the target characteristics and their role in the scattering process.

Major contributions of this investigation are:

1) First measurements of scattering distributions for beams with energies between 1 and 10 ev.

2) Observations of multilobular distributions of scattered-beam flux.

3) Systematic analysis of the TOF speed distribution spectroscopy technique. Derivation of relations between

85

the central-moment expansions of the speed distribution, chopper gate function, and time-of-flight signal.

4) Application of the above analysis to a novel calibration concept of ionization detectors. This concept should be applicable also to calibration and standardization procedures for ion vacuum pumps.

5) Analysis of the dynamic properties of the chopper, detector, and target in scattering and flash-desorption experiments.

6) Demonstration of feasability of measuring (in addition to mean speeds and mean energies) the distribution of hydrodynamic speed ratios as a function of scattering angle.

Interpretation of these results would be facilitated if the contribution of desorbed species were known.

Conclusions

1. The quasi-specular lobes bear a close resemblance to those observed by other investigators who have scattered thermal-energy beams from various clean surfaces.

2. The quasi-specular lobes behave in some respects as predicted by one simplified collision model.

3. Careful analyses of the data indicate that the detected molecules may have consisted of both scattered Argon atoms and flash-desorbed unknown species from the surface. This hypothesis can be tested in TOF experiments with a mass filter (mass spectrometer) in series with the ionization detector.

4. A satisfactory explanation of the multilobular pattern
    of the measured flux distribution has not been found.
    If the flash-desorption hypothesis is correct, uncoupling
    of the contribution to the multilobular pattern by the
    desorbed species would require a mass-spectrometer.
    If such an investigation reveals a single-lobe contribution
    by the scattered particles, it is anticipated that this lobe
    would not be of the cosine-law type. This result would
    be of interest in studies of the adsorbed state on surfaces.

Recommendations for Future Work

The unexpected results obtained in this study need further
exploration. The complete investigation of the multilobular pattern
is important, not only because of its importance in characterizing
the processes at the surface, but also because of its immediate
practical importance in space applications. It is recommended that
the recently acquired mass spectrometer be used in the following
two consecutive experiments, which differ only in the location of the
chopper.

a) Modulate the incident beam in order to provide separate
flux distributions of the scattered and desorbed species. By varying
the density and composition of the background, this type of experi-
ment can provide also information on the kinetics of the adsorption
and desorption processes as well as information on the interatomic
potentials between background and surface atoms.

b) Modulate the scattered molecular field when a steady-state
beam is incident, in order to provide higher resolution of the TOF
signals of the scattered field. Therefore more accurate spatial
distributions of the mean speed, mean energy, and hydrodynamic
speed ratios of the scattered molecules can be obtained.

An increased density of the incident beam at the surface would compensate for the reduction of the detector sensitivity which accompanies an improvement in the TOF resolution of the scattered beam signals. The recent installation of an additional diffusion pump in the collimation chamber should increase this density significantly by reducing the background scattering. Also, the reduction of the overall distance between the skimmer orifice and the scattering surface should be considered; one might accept poorer collimation in order to reduce beam spreading.

Determinations of the first and second moments of the dynamic calibration function $g_d(t)$ in situ during actual measurements are recommended also. This is achieved (as suggested by Equations (4.31b,c) by recording the signals at a given spatial coordinate setting of the detector for different values of the chopper angular speed. The intercepts in plots of the moments vs. appropriate powers of the time intervals between signals give direct measures of the higher-than-zero moments of the calibration function. It is not necessary to assume a) that a detector behaves purely in through-flow fashion and b) that reactance perturbations introduced by the signal processing chain are negligible and/or independent of the location of the detector.

Possibilities for future studies involving the factorial permutation of parameters known or suspected to affect the scattering interactions between gaseous flow fields and condensed phases are obvious and the reader will not be burdened further with sententious recommendations.

GENERAL REFERENCES

GR I   Rarefied Gas Dynamics, Proceedings of the First International Symposium at Nice, France, Ed. F.M. Devienne, London: Pergamon Press (1960).

GR II   Rarefied Gas Dynamics, Proceedings of the Second International Symposium at Berkeley, Ed. L. Talbot, New York: Academic Press (1961).

GR III   Rarefied Gas Dynamics, Proceedings of the Third International Symposium at Paris (1962), Ed. J.A. Laurmann, New York: Academic Press (1963).

GR IV   Rarefied Gas Dynamics, Proceedings of the Fourth International Symposium at Toronto (1964), Ed. J.H. de Leeuw, New York: Academic Press (1966).

GR V   Rarefied Gas Dynamics, Proceedings of the Fifth International Symposium at Oxford (1966), Ed. C.L. Brundin, New York: Academic Press (1967).

GR VI   Massey, H.S.W. and Burhop, E.M.S., Electronic and Ionic Impact Phenomena, Oxford: Oxford University Press (1952).

GR VII   Kaminsky, M., Atomic and Ionic Impact Phenomena on Metal Surfaces, New York: Academic Press (1965).

GR VIII   Bates, D.R. and Estermann, I., Eds., Advances in Atomic and Molecular Physics, New York: Academic Press (1965).

GR IX   Symposium on "Fundamentals of Gas-Surface Interactions," Dec. 14-16 (1966), San Diego, California. Proceedings to be published.

REFERENCES

1. Alcalay, J.A. and Knuth, E.L., "Experimental Study of Scattering in Particle-Surface Collisions with Particle Energies of the Order of 1 ev.," Appears in GR V.

2. Anderson, J.B., Andres, R.P. and Fenn, J.B., Appears in GR VIII.

3. Cabrera, N., "The Structure of Crystal Surfaces," Disc. Faraday Soc. 28:16-22, (1959).

3a. Callinan, J.P., "A Method of Determining the Velocity Distribution in a Reflected Molecular Beam," Department of Engineering M.S. Thesis, University of California, Los Angeles, (June 1961).

4. Kinzer, E.T., and Chambers, C.M., "On the Collision of Atoms With Crystal Surfaces," Surface Science 3:261-279, (July 1965).

5. Datz, S., Moore, G.E. and Taylor, E.H., Appears in GR III.

6. Devienne, F.M., Souquet, J. and Roustan, J.C., Appears in GR IV.

7. Ehrlich, G., "Atomic Processes at Solid Surfaces," Annual Review of Physical Chemistry 17:295-322, (1966).

8. Eucken, A. and Bertram, A., "Die Ermittlung der Molwärme einiger Gase bei tiefen Temperaturen nach der Warmeleitfahigkeitsmethode," Z. Physik. Chem. B 31: 361, (1936).

9. French, J.B., AIAA Journal 3:993-1000, (June 1965).

10. Gilbey, D.M., "A Simple Model for Gas-Solid Energy Exchange," Appears in GR V.

11. Gilbey, D.M., "A Re-examination of Thermal Accommodation Coefficient Theory," J. Phys. Chem. Solids 23:1453-1461, (1962).

REFERENCES (Cont.)

12. Goodman, F.O., "Preliminary Results of a Three-Dimensional Hard-Sphere Theory of Scattering of Gas Atoms From a Solid Surface," Appears in GR V.

13. Goodman, F.O., "On the Theory of Accommodation Coefficients," J. Phys. Chem. Solids 26:85-105 (1965).

14. Goodman, F.O., "Response Functions and Thermal Motions of a Simple n-Dimensional Lattice Model," Surface Science 3:386-414 (1965).

15. Goodman, F.O., "On the Theory of Accommodation Coefficients," J. of Phys. and Chem. of Solids 24:1451-1466 (1963), also in GR IV.

16. Goodman, F.O., "The Dynamics of Simple Cubic Lattices," J. of Phys. and Chem. of Solids 23:1491-1502 (1962), also ibid 23:1269-1290 (1962).

17. Hinchen, J.J. and E.S. Malloy, "Velocity of Molecular Beam Molecules Scattered by Platinum Surfaces," Appears in GR IX.

18. Hinchen, J.J. and Shepherd, E.F., "Scattering of Molecular Beams by Surfaces of Platinum and Tantalum," Appears in GR V.

19. Hinchen, J.J. and Foley, W.M., "Scattering of Molecular Beams by Metallic Surfaces," Appears in GR IV.

20. Hurlbut, F.C., "On the Molecular Interactions Between Gases and Solids," University of California I.E.R. Technical Report, HE 150-208, (November 15, 1962).

21. Jaeger, H. Mercer, P.D. and Sherwood, G.G., "The Structure of Silver Films Deposited on Mica Substrates in Ultra-High Vacuum," Surface Science 6:309-322 (1967).

22. Knuth, E.L., "Supersonic Molecular Beams," Applied Mechanics Review 17:751-762, (October 1964).

REFERENCES (Cont.)

23. Knuth, E.L., "Second Status Report on Development and Application of an Intermediate-Energy, High-Intensity Molecular Beam," University of California, Los Angeles, Dept. of Engr. Report No. 66-19, (April 1966).

24. Kuluva, N.M., "An Analytic and Experimental Study of the Performance of an Arc-Heated, Supersonic, 1 ev Molecular Beam and its Applications to Molecule-Molecule Collision Studies," University of California, Los Angeles, Dept. of Engr. Report No. 67-11 (1967).

25. Leonas, V.B., Soviet Physics Uspekhi 7:121-144, (1964).

26. Logan, R.M., Keck, J.C. and Stickney, R.E., "Simple Classical Model for the Scattering of Gas Atoms From a Solid Surface," Appears in GR V.

27. Logan, R.M., and Stickney, R.E., "Simple Classical Model for the Scattering of Gas Atoms from a Solid Surface," J. Chem. Phys. 44:195-201, (January 1, 1966).

28.. McCarrol, B. and Ehrlich, G., "Trapping and Energy Transfer in Atomic Collisions with a Crystal Surface," J. Chem. Phys. 38 (1963).

29. Mourad, W.G., Pauly, T. and Herb, R.G., "Orbitron Ionization Gauge," Rev. of Sci. Instr. 35:661-665 (1964).

30. Oman, R.A., Bogan, A. and Li, C.H., "Research on Molecule-Surface Interaction; Part I - Theoretical Prediction of Momentum and Energy Accommodation for Hypervelocity Gas Particles on an Ideal Crystal Surface," Appears in GR IV.

31. Oman, R.A., "Calculations of the Interactions of Diatomic Molecules with Solid Surfaces," Appears in GR V.

32. Smith, J.N., "Molecular Beam Scattering from Solid Surfaces," Appears in GR IX.

33. Smith, J.N. and Saltsburg, H., "Scattering of Molecular Beams of He, D_2, and H_2 from the (111) Plane of Ag," Appears in GR V.

REFERENCES (Cont.)

34. Smith, J.N. and Saltsburg, H., "Recent Studies of Molecular Beam Scattering from Continuously Deposited Gold Film," Appears in GR IV.

35. Smith, J.N., "Scattering of Atomic Beams by Polycrystalline Nickel," J. Chem. Phys. 40:3585-3591 (1964).

36. Smith, J.N. and Fite, W.L., "Recent Investigations of Gas-Surface Interactions Using Modulated-Atomic-Beam Techniques," Appears in GR III.

37. Stickney, R.E., Logan, R.M., Yamamoto, S. and Keck, J.C., "Simple Classical Model for the Scattering of Gas Atoms from a Solid Surface," Appears in GR IX.

38. Trilling, L., "Theory of Gas Surface Interaction," Appears in GR IX.

39. Trilling, L., "A Theory of Energy Accommodation," Journal de Mecanique 3:214-234, (1964).

40. Wachman, Harold Y., "The Thermal Accommodation Coefficient: A Critical Survey," ARS Journal 32:2-12 (1962).

41. Wehner, G.K. and D. Rosenberg, J. Applied Physics 31: 177-179 (1960).

42. Winicur, D. and Knuth, E.L., "Measurement of Excitation and Ionization in an Arc-Heated Supersonic Argon Beam," J. Chem. Phys. 46 (June 1, 1967).

43. Zwanzig, R.W., "Collisions of a Gas Atom with a Cold Surface," J. Chem. Phys. 40:1173-1177 (1964).

APPENDIX A

A CLASS OF SPEED DISTRIBUTION FUNCTIONS, THE CORRESPONDING TOF FUNCTIONS, AND RELATED MOMENTS

A1. INTRODUCTION

Many problems in kinetic theory and rarefied gas dynamics involve the evaluation of the moments of speed distribution functions of the form

$$F_n(s) = s^n \exp - (s-S)^2 \qquad (A1.1)$$

Thus the zeroth moment $\mu_0\{F_n(s)\}$ represents the inverse of the normalizing factor of this function, so that the normalized speed distribution is given by

$$f_n(s) = C_n \, s^n \exp - (s-S)^2$$

$$= \frac{F_n(s)}{\mu_0\{F_n(s)\}} \qquad (A1.2)$$

The first moment $\eta_1\{F_n(s)\}$ represents the mean speed of the particles and is useful directly in calculating the mean energy of the particles.

In modulated molecular beam experiments one often measures the time-of-flight distributions $\rho(t)$ and $\phi(t)$ to a distance L, which are related directly to the speed distribution, $f_n(s)$, and the flux distribution, $J_n(s) = \gamma s f_n(s)$, respectively.

In this appendix the Laplace transform of the speed distribution is derived first and used then as a moment-generating function to derive the moments of $F_n(s)$. The moments of $\rho_n(t)$ and $\phi_n(t)$ are related directly then to the moments of $F_n(s)$. Useful recursion

94

formulas are derived and graphs of the various moments for selected values of n are displayed.

A2. DEFINITIONS AND SOME BASIC RELATIONSHIPS

Laplace Transform:

$$L\{F_n(s)\} \doteq \int_0^\infty F_n(s) \exp(-ps) ds \qquad (A2.1)$$

Derivatives of Laplace Transform:

$$(-d/dp)^n L\{F(t)\} = L\{t^n F(t)\} = (-1)^n F_n(p) \qquad (A2.2)$$

Moments of a function $f(t)$:

a. The m'th non-normalized moment of $f(t)$:

$$\mu_m\{f(t)\} \doteq \int_0^\infty t^m f(t) dt \qquad m = 0, 1, \ldots \qquad (A2.3)$$

b. The m'th normalized moment of $f(t)$:

$$\eta_m\{f(t)\} = \frac{\mu_m\{f(t)\}}{\mu_0\{f(t)\}} \qquad (A2.4)$$

$\eta_1\{f(t)\}$ is often referred to as the mean value of $f(t)$.

c. The m'th central moment (or moment about the mean):

$$\nu_m\{f(t)\} \doteq \left[\mu_0\{f(t)\}\right]^{-1} \int_0^\infty \left[(t - \eta_1\{f(t)\}\right]^m f(t) dt$$

$$m = 1, 2, \ldots \qquad (A2.5)$$

In particular, for $m = 2$,

$$\nu_2\{f(t)\} = \eta_2\{f(t)\} - \eta_1^2\{f(t)\} \qquad (A2.6)$$

is referred to as the variance of $f(t)$.

$$\text{erf } y \overset{\bullet}{=} (2/\sqrt{\pi}) \int_0^y \exp(-x^2)dx \qquad \text{(A1.7)}$$

$$\text{erfc } y \overset{\bullet}{=} 1 - \text{erf } y \qquad \text{(A1.8)}$$

A3. THE LAPLACE TRANSFORMS OF $F_n(s) = s^n \exp\text{-}(s\text{-}S)^2$

From tabulated transforms we find

$$L\{2(a/\pi)^{\frac{1}{2}} \exp(-at^2)\} = \exp(p^2/4a) \text{ erfc}\left(p/2(a)^{\frac{1}{2}}\right) \qquad \text{(A3.1)}$$

One of the shifting theorems states

$$L[\exp(-at)f(t)] = L[f(t)]_{p\to p+a} \qquad \text{(A3.2)}$$

Applying (A3.1) and (A3.2) to $F_o(s) = \exp\text{-}(s\text{-}S)^2$, we find

$$F_o(p) = (\sqrt{\pi}/2) \exp(-S^2) \exp\left(\frac{1}{4}(p-2S)^2\right)\text{erfc}\left(\frac{1}{2}(p-2S)\right) \qquad \text{(A3.3)}$$

Applying (A2.2) with n=1, one obtains

$$F_1(p) = \frac{1}{2}(p-2S) F_o(p) - \frac{1}{2}\exp(-S)^2 \qquad \text{(A3.4)}$$

By successive applications of (A2.2), the following recursion equation is derived:

$$F_n(p) = \frac{1}{2}(n-1) F_{n-2}(p) + \frac{1}{2}(p-2S) F_{n-1}(p) \qquad \text{(A3.5)}$$

where n is an interger ≥ 2.

By successive applications, $F_n(p)$ can be expressed in polynomial form

$$F_n(p) = F_o(p) \sum_{i=0}^{n/2} a_n^{2i}\xi^{n-2i} - \frac{1}{2}\exp\text{-}(S^2) \sum_{i=0}^{n/2} a_n^{2i+1}\xi^{n-2i-1} \qquad \text{(A3.6)}$$

where
$$\xi \overset{\bullet}{=} \frac{1}{2}(p-2S)$$

and the coefficients a_n^j are defined by

$$a_n^o = 1 \quad \text{for all} \quad n \geq 0$$

$$a_n^1 = 1 \quad \text{for all} \quad n > 0 \qquad a_n^1 = 0 \quad \text{for} \quad n = 0$$

$$a_n^j = a_{n-1}^j + \frac{n-1}{2} a_{n-2}^{i-2}$$

$$a_n^2 = \frac{n(n-1)}{4} \qquad a_n^3 = \frac{(n+1)(n-2)}{4} \tag{A3.7}$$

Some of the a_n^j are displayed in Table A.1.

A4. THE ZEROTH MOMENT $F_n(s)$

The Laplace transform of $F_n(s)$ can be considered as a moment-generating function. It follows from (A2.1), (A2.2), and (A2.3) that

$$\lim_{p \to o} \{d/dp\}^m F_n(p) = (-1)^{m+n} \mu_m \{F_n(s)\} \tag{A4.1}$$

Applying (A4.1) to (A3.5) for the case $m=0$, one obtains the recursion formula for $\mu_0\{F_n(s)\}$

$$\mu_0\{F_n(s)\} = \frac{1}{2}(n-1)\,\mu_0\{F_{n-2}(s)\} + S\,\mu_0\{F_{n-1}(s)\} \tag{A4.2}$$

The zeroth moment can be expressed also in a polynomial form

$$\mu_0\{F_n(s)\} = \phi \sum_{i=0}^{n/2} a_n^{2i} S^{n-2i} + \psi \sum a_n^{2i+1} S^{n-2i-1} \tag{A4.3}$$

where

$$\phi \doteq \frac{1}{2}(\pi)^{\frac{1}{2}}(1 + \text{erf } S)$$

$$\psi \doteq \frac{1}{2}\exp(-S^2)$$

and the coefficients a_n^i obey the relationships (A3.7)

TABLE A.1

COEFFICIENTS a_j^n IN THE SERIAL EXPANSION OF THE LAPLACE TRANSFORM AND
ZEROTH MOMENTS OF THE SPEED DISTRIBUTIONS $F_n(s)$

n \ j	0	1	2	3	4	5	6	7	8
0	1	0	0	0	0	0	0	0	0
1	1	1	0	0	0	0	0	0	0
2	1	1	1/2	0	0	0	0	0	0
3	1	1	3/2	1	0	0	0	0	0
4	1	1	3	5/2	3/4	0	0	0	0
5	1	1	5	9/2	15/4	2	0	0	0
6	1	1	15/2	7	45/4	33/4	15/8	0	0
7	1	1	21/2	10	105/4	87/4	105/8	6	0

Table A.2 gives the expressions for $\mu_o\{F_n(s)\}$ for $0 \leq n \leq 5$. Figure A.1 is a plot of the zeroth moment as a function of the hydrodynamic speed ratio, S.

A5. HIGHER NORMALIZED MOMENTS

In view of the definition of $F_n(s)$ (Equation A1.1) and the definitions of $\mu_j\{F_n(s)\}$ (Equation A2.3) one can write

$$\mu_j\{F_n(s)\} = \mu_{j\pm k}\{F_{n\mp k}(s)\} \quad k=0,1,2,\ldots,j \tag{A5.1}$$

so that, in particular, for $k=j$, we have

$$\mu_j\{F_n(s)\} = \mu_o\{F_{n+j}(s)\} \tag{A5.2}$$

Applying this result to the definition of $\eta_j\{f_n(s)\}$ (Equation A2.4), one obtains

$$\eta_j\{F_n(s)\} = \mu_o\{F_{n+j}(s)\} / \mu_o\{F_n(s)\} \tag{A5.3}$$

Consider the case for $j=1$, i.e., the first normalized moment

$$\eta_1\{F_n(s)\} = \mu_o\{F_{n+1}(s)\} / \mu_o\{F_n(s)\} \tag{A5.4}$$
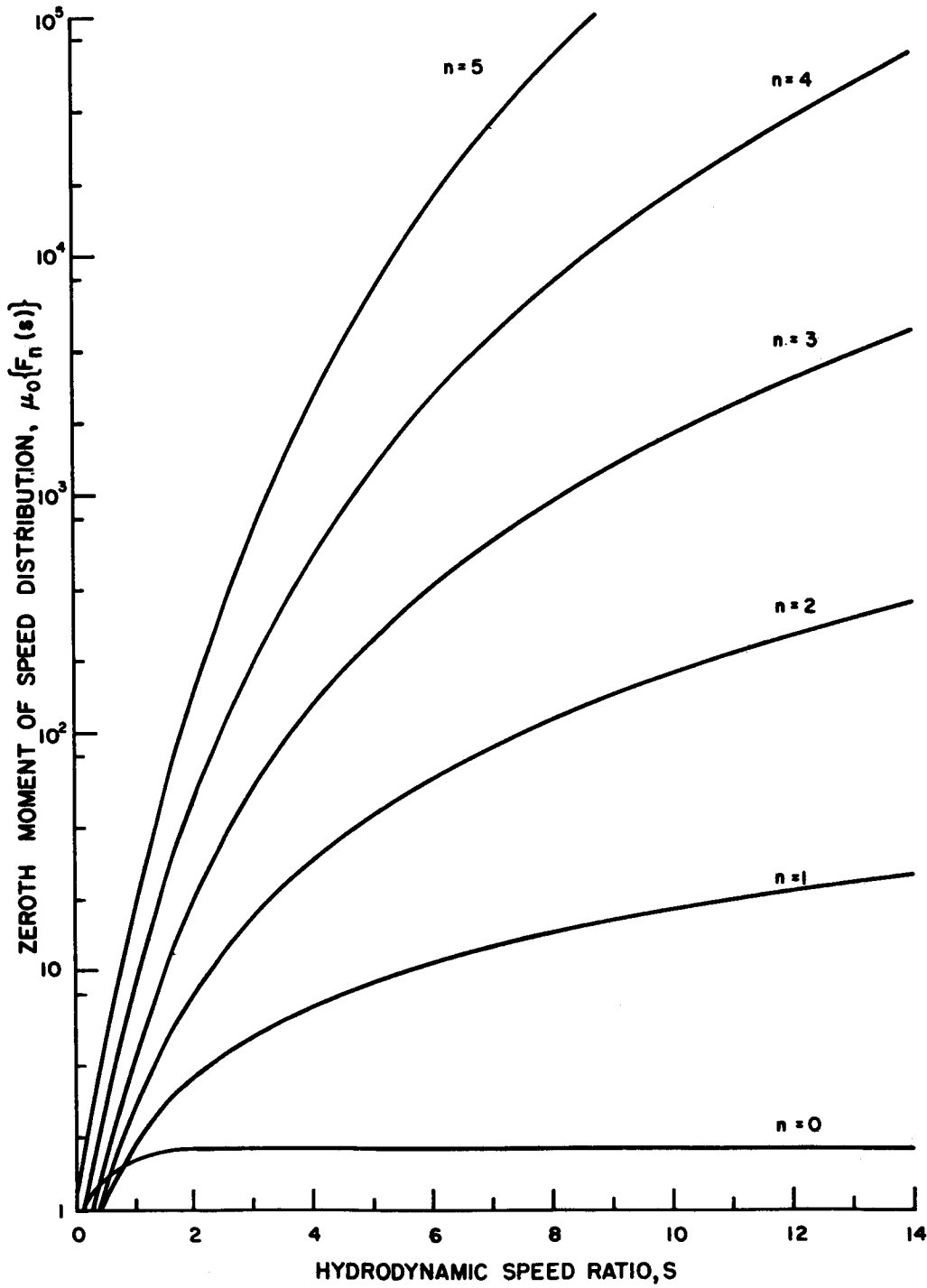
Substitute for $\mu_o\{F_{n+1}(s)\}$ from Equation (A4.2)

$$\eta_1\{F_n(s) = \left(\frac{1}{2} n \, \mu_o\{F_{n-1}(s)\} / \mu_o\{F_n(s)\} \right) + S \tag{A5.5}$$

Substituting from the definition of $\eta_1\{F_{n-1}(s)\}$, we obtain the recursion formula for the first moment

$$\eta_1\{F_n(s)\} = \frac{1}{2} n \left[\eta\{F_{n-1}(s)\} \right]^{-1} + S \tag{A5.6}$$

Combining (A5.3) and (A4.2) we obtain the generalized recursion formula

$$\eta_j\{F_n(s)\} = \frac{1}{2} (n+j-1) \, \eta_{j-2}\{F_n(s)\} + S\eta_{j-1}\{F_n(s)\} \tag{A5.7}$$

ZEROTH MOMENT OF THE SPEED DISTRIBUTIONS
$F_n(S)$ FOR SEVERAL VALUES OF n

FIGURE A1

TABLE A.2

ZEROTH MOMENT $\mu_o\{F_n(s)\}$ FOR SEVERAL VALUES OF n

N	For all values of S	For S = 0	For $\phi S >> \psi$	For S >> 1
0	ϕ	$\dfrac{\sqrt{\pi}}{2}$	ϕ	$\sqrt{\pi}$
1	$\phi S + \psi$	$1/2$	ϕS	$\sqrt{\pi}\,S$
2	$\phi(S^2 + \frac{1}{2}) + \psi S$	$\dfrac{\sqrt{\pi}}{4}$	$\phi(S^2 + \frac{1}{2})$	$\sqrt{\pi}\,(S^2 + \frac{1}{2})$
3	$\phi(S^3 + \frac{3}{2}S) + \psi(S^2 + 1)$	$1/2$	$\phi(S^3 + \frac{3}{2}S)$	$\sqrt{\pi}\,(S^3 + \frac{3}{2}S)$
4	$\phi(S^4 + 3S^2 + \frac{3}{4}) + \psi(S^3 + \frac{5}{2}S)$	$\dfrac{3}{8}\sqrt{\pi}$	$\phi(S^4 + 3S^2 + 3/4)$	$\sqrt{\pi}\,(S^4 + 3S^2 + 3/4)$
5	$\phi(S^5 + 5S^3 + \frac{15}{4})\,\psi(S^4 + \frac{9}{2}S^2 + 2)$	1	$\phi(S^5 + 5S^3 + \frac{15}{4}S)$	$\sqrt{\pi}\,(S^5 + 5S^3 + \frac{15}{4}S)$

valid for $j \geq 0$. Note that, combining (A5.2) and (A5.3), one obtains, in general,

$$\eta_{-1}\{F_n(s)\} = \left[\eta_j\{F_{n-j}(s)\}\right]^{-1} \tag{A5.8}$$

where j is a positive integer.

Tables A.3 and A.4 give expressions for η_1 and η_2 for values of n from 0 to 4. Figures A.2 and A.3 are graphical representations of Tables A.3 and A.4.

In view of (A1.2), note that

$$\mu_0\{f_n(s)\} = 1 \tag{A5.9}$$

and that

$$\eta_j\{F_n(s)\} = \eta_j\{f_n(s)\} \, \mu_j\{f_n(s)\} \tag{A5.10}$$

A6. RELATION BETWEEN THE MOMENTS OF $\rho_n(t)$, $\phi_n(t)$ AND $f_n(s)$

The time-domain analogues of the speed distribution function $f_n(s)$ and of the flux $J_n(s)$ are defined as follows:

$$\rho_n(t) = f_n(s) \, \frac{ds}{dt} = \frac{F_n(s)}{\mu_0\{F_n(s)\}} \, \frac{ds}{dt} \tag{A3.6}$$

$$\phi_n(t) = sf_n(s) \, \frac{ds}{dt} = \frac{sF_n(s)}{\mu_0\{F_n(s)\}} \, \frac{ds}{dt} \tag{A3.7}$$

The zeroth moments are: (see Equation A2.3)

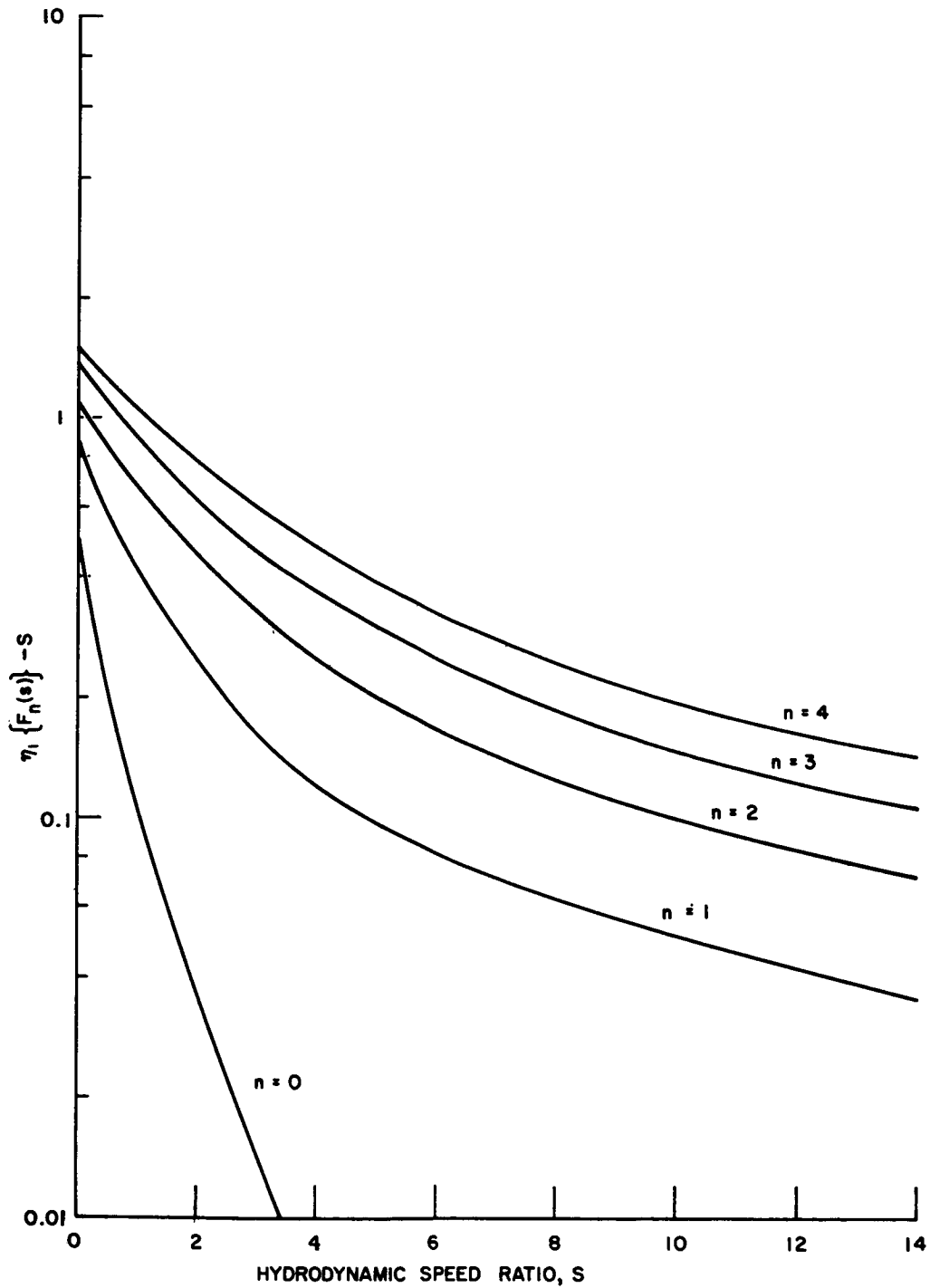$$\mu_0\{\rho_n(t)\} = \int_0^\infty f_n(s) \, \frac{ds}{dt} \, dt = 1 \tag{A6.1}$$

$$\tag{A6.2}$$

TABLE A.3

DEVIATION OF THE MEAN SPEED RATIO (FIRST MOMENT) FROM THE HYDRODYNAMIC SPEED RATIO S FOR SEVERAL VALUES OF n

$$\eta_1\{F_n(s)\} - S$$

| n	For all values of S	For $S/r \gg 1$	For $S = 0$
0	$\left[(1 + \text{erf } S)\,\sqrt{\pi}\,\exp(S^2)\right]^{-1} \equiv \frac{\dot{\psi}}{\dot{\phi}} \equiv \dot{r} \equiv r$	0	$1/\sqrt{\pi}$
1	$\dfrac{1}{2(S + r)}$	$\dfrac{1}{2S}$	$\dfrac{\sqrt{\pi}}{2}$
2	$\dfrac{2(S + r)}{2S\,(S+r)+1} =$	$\dfrac{1}{S} - \dfrac{1}{S(2S^2 + 1)}$	$\dfrac{2}{\sqrt{\pi}}$
3	$\dfrac{3[\,2S(S+r) + 1\,]}{2[\,2(S^2 +1)\,(S+r) + S\,]}$	$\dfrac{3}{2S} - \dfrac{3}{S(2S^2 + 3)}$	$\dfrac{3\sqrt{\pi}}{4}$
4	$\dfrac{4[\,2(S^2 + 1)\,(S+r) + S\,]}{2S(2S^2 + 5)\,(S+r) + 2S^2 + 3}$	$\dfrac{2}{s} - \dfrac{6(2S^2 + 1)}{4S^5 + 12S^3 + 3S}$	$\dfrac{8}{3\sqrt{\pi}}$

TABLE A.4

DEVIATION OF THE SECOND MOMENT FROM THE SQUARE OF THE HYDRODYNAMIC SPEED RATIO S FOR SEVERAL VALUES OF n

$$\eta_2\{F_n(s)\} - S^2$$

n	For all values of S	For $S/r \gg 1$	For $S = 0$
0	$\dfrac{1}{2} + rS$	$rS + \dfrac{1}{2}$	$1/2$
1	$1 + \dfrac{S}{2(S+r)}$	$3/2$	1
2	$\dfrac{2}{3} + \dfrac{2S(S+r)}{2S(S+r)+1}$	$\dfrac{5}{2} - \dfrac{1}{2S^2+1}$	$\dfrac{3}{2}$
3	$2 + \dfrac{3[2S^2(S+r)+S]}{2[2(S^2+1)(S+r)+S]}$	$\dfrac{7}{2} - \dfrac{3}{2S^2+3}$	2
4	$\dfrac{5}{2} + \dfrac{4S[2(S^2+1)(S+r)+S]}{2S(2S^2+5)(S+r)\,2S^2+3}$	$\dfrac{9}{2} - \dfrac{6(2S^2+1)}{4S^4+12S^2+3}$	$\dfrac{5}{2}$

DEVIATION OF THE MEAN SPEED RATIO (FIRST MOMENT)
FROM THE HYDRODYNAMIC SPEED RATIO S FOR
SEVERAL VALUES OF n

FIGURE A2
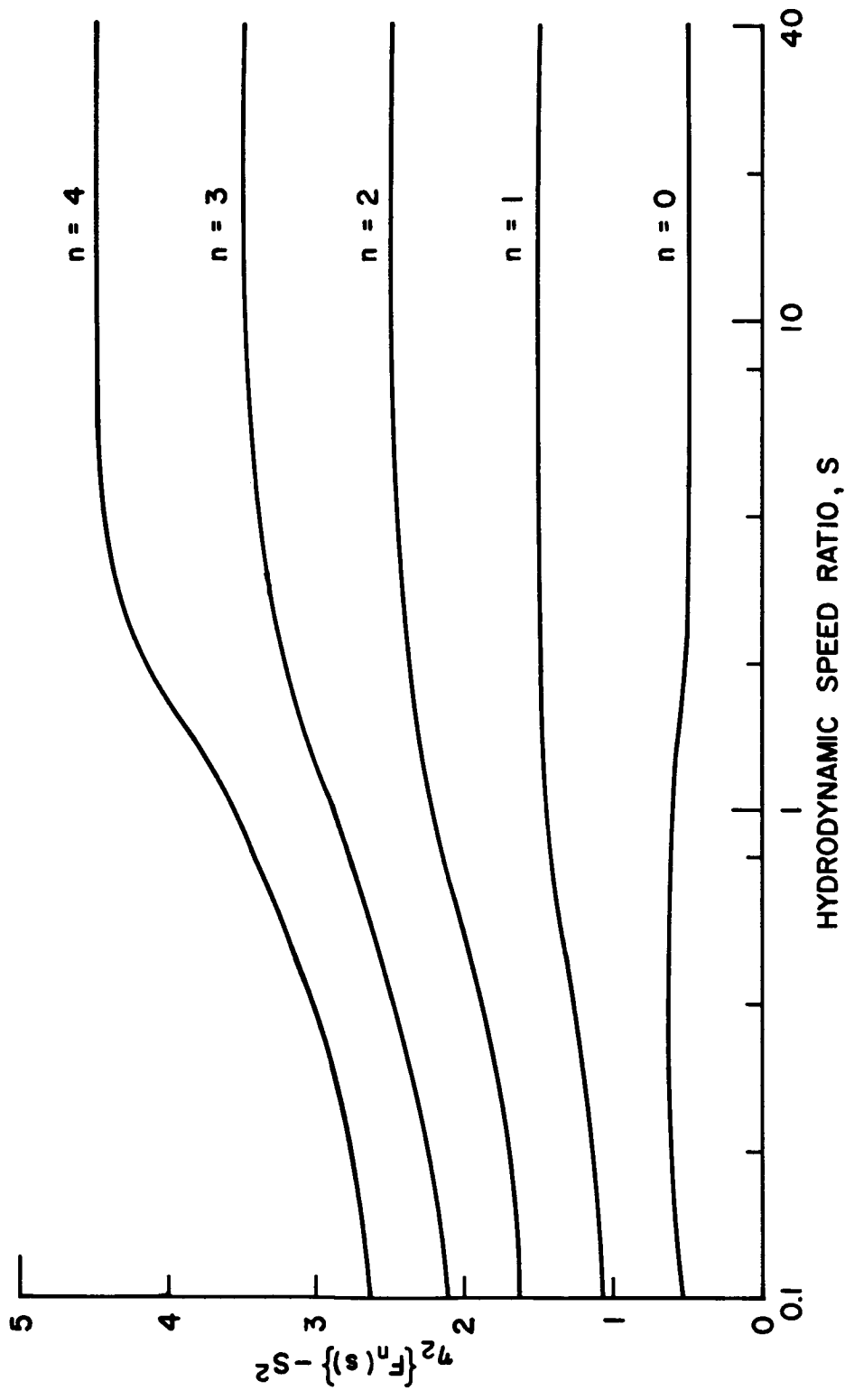
DEVIATION OF THE SECOND MOMENT FROM THE SQUARE
OF THE HYDRODYNAMIC SPEED RATIO

FIGURE A3

$$\mu_o\{\phi_n(t)\} = \int_0^\infty sfn(s) \frac{ds}{dt}\, dt$$

$$= \mu_1\{f_n(s)\} = \eta_1\{f_n(s)\} \tag{A6.2}$$

The j'th moment of $\rho_n(t)$ is by definition

$$\mu_j\{\rho_n(t)\} = \int_0^\infty t^j f_n(s) \frac{ds}{dt}\, dt$$

But, in view of Equation (A6.1) and the relation for t,

$$t = \frac{L}{\gamma s}$$

we may write

$$\eta_j\{\rho_n(t)\} = \left(\frac{L}{\gamma}\right)^j \eta_{-j}\{f_n(s)\} \tag{A6.3}$$

where

$$\eta_{-j}\{f_n(s)\} = \frac{1}{\eta_j\{f_{n-j}(s)\}} \tag{A6.4}$$

Similarly, one derives the j'th moment of $\phi_n(t)$

$$\eta_j\{\phi_n(t)\} = \left(\frac{L}{\gamma}\right)^j \eta_{-j}\{f_{n+1}(s)\} \tag{A6.5}$$

By algebraic manipulation of Equations (A6.3), (A6.4), (A5.1), (A5.3) and (A5.10) one obtains the following recursion relations.

$$\eta_j\{\rho_n(t)\} = \eta_k\{\rho_n(t)\}\, \eta_{n-k}\{\rho_{n-k}(t)\} \tag{A6.6}$$

$$\eta_j\{\phi_n(t)\} = \eta_k\{\phi_n(t)\}\, \eta_{j-k}\{\phi_{n-k}(t)\} \tag{A6.7}$$

For the special case j = 2 and k = 1

$$\eta_2\{\rho_n(t)\} = \eta_1\{\rho_n(t)\}\, \eta_1\{\rho_{n-1}(t)\} \tag{A6.8}$$

$$\eta_2\{\phi_n(t)\} = \eta_1\{\phi_n(t)\}\, \eta_1\{\phi_{n-1}(t)\} \tag{A6.9}$$

Combining (A6.8), (A6.9) and (A6.3), (A6.5) one obtains

$$\frac{\eta_2\{\rho_n(t)\}}{\eta_1^2\{\rho_n(t)\}} = \frac{\eta_1}{\eta_2} \frac{\{f_{n-1}(s)\}}{\{f_{n-2}(s)\}} \overset{\bullet}{=} \Omega_{n-1}(S) + 1 \qquad (A6.10)$$

$$\frac{\eta_2\{\phi_n(t)\}}{\eta_2^2\{\phi_n(t)\}} = \frac{\eta_1}{\eta_2} \frac{\{f_n(s)\}}{\{f_{n-1}(s)\}} \overset{\bullet}{=} \Omega_n(S) + 1 \qquad (A6.11)$$

These last expressions are valuable because they relate moments of time-of-flight distribution functions to functions of only the speed ratio S (i.e., they are independent of the ratio L/γ).

APPENDIX B

THE ALGEBRA OF LINEAR OPERATORS AND CERTAIN RELATIONSHIPS BETWEEN THE MOMENTS OF THEIR SUMS AND PRODUCTS

B1. INTRODUCTION

In this Appendix, basic concepts from the theory of linear operators are used to derive certain relationships used in Chapters II - V. The customary non-mathematicians' escape clause is adopted by the author in order to protect the domain of rigor and elegance reserved to bona fide mathematicians. Proofs are not offered in all cases.

B2. DEFINITION

Let X_1 and X_2 be two abstract vectors in vector space representing two fields. Let g be an operator such that X_2 is obtained when g acts on X_1

$$X_2 = g X_1 \tag{B.1}$$

The operator g is linear if the relationship B.1 is linear. The sum of abstract operators is associative and commutative. The product is associative, distributive and in general not commutative. If g is linear, then the product is also commutative. (This last statement is not necessarily true in Hermitian space, but is true for the restricted applications of interest here.) The identity operator I is defined in the usual fashion

$$X \overset{\cdot}{=} I X \tag{B.2}$$

B3. REPRESENTATIONS OF THE LINEAR OPERATORS

In the complex-domain representation (represented by the Laplace variable p and its functions) the product and sum of linear

operators remain identical in form. The identity operator represent-
ation is unity.

In the time-domain representation (related to the complex-
plane representation by means of the linear Laplace transformation
expressed by Equation A2.1) the product takes the form of a con-
volution integral; the sum remains identical in form to the sum in
the abstract space. The time-domain representation of the identity
operator is the $\delta(t)$ (Dirac) function.

In the signal-flow diagram representation (where the operator
g is represented by a box between two directed lines which represent
the vectors X) a product is given by boxes in series and a sum is
represented by operator boxes in parallel. The identity operator is
represented by the absence of a box and an uninterrupted directed
vector line.

Note that the vectors X_i belong to the same space as the opera-
tors g and all algebraic operations true for g apply also to operations
between X's and g's.

B4.　RELATIONSHIP BETWEEN THE MOMENTS OF LINEAR OPERATOR PRODUCTS AND SUMS

a)　Sums

Let $g_1(t)$, $g_2(t)$ and g(t) be the time representation of two
linear operators, g_1 and g_2, and their sum g.

$$g(t) = g_1(t) + g_2(t) \tag{B.3}$$

Then we can write

$$\int_0^\infty t^j g(t)dt = \int_0^\infty t^j g_1(t)dt + \int_0^\infty t^j g_2(t)dt \tag{B.4}$$

if the integrals are "well behaved." Hence, in general, the following

relationships apply

$$\mu_j\{g(t)\} = \sum_k \mu_j\{g_k(t)\} \qquad j = 1, 2, \ldots$$

when

$$g(t) = \sum_k g_k(t) \tag{B.5}$$

b) **Products**

Let $g(p)$ be the product of $g_1(p)$ and $g_2(p)$ in the complex p-domain representation.

$$g(p) = g_1(p) \; g_2(p) \tag{B.6}$$

and the corresponding representation in the time domain

$$g(t) = \int_0^t g_1(x) \; g_2(t-x)dx \tag{B.7}$$

The first logarithmic derivative with respect to p of Equation (B.) gives

$$\frac{g'(p)}{g(p)} = \frac{g_1'(p)}{g_1(p)} + \frac{g_2'(p)}{g_2(p)} \tag{B.8}$$

where

$$g'(p) \stackrel{\bullet}{=} \frac{dg(p)}{dp} \tag{B.9}$$

Taking the second derivative of (B.6), dividing both sides by $g(p)$ and subtracting from the resulting equation the square of Equation (B.8), one obtains

$$\frac{g''(p)}{g(p)} - \left[\frac{g'(p)}{g(p)}\right]^2 = \frac{g_1''(p)}{g_1(p)} - \left[\frac{g_1'(p)}{g_1(p)}\right]^2 + \frac{g_2''(p)}{g_2(p)} - \left[\frac{g_2'(p)}{g_2(p)}\right]^2 \tag{B.10}$$

Recall (Equation A4.4) that the limit of the n'th derivative of a Laplace transform as p tends toward zero gives the n'th moment of the function in the time domain.

$$\lim_{p \to 0} g^{(n)}(p) = (-1)^n \int_0^\infty t^n f(t)dt = (-1)^n \mu_n\{f(t)\} \qquad (B.11)$$

One may apply this limiting process to (B.6), (B.8) and (B.10); in view of the definitions of the moments (Equations A2.4, A2.5), one obtains the following relations

$$\mu_0\{g(t)\} = \mu_0\{g_1(t)\} \, \mu_0\{g_2(t)\} \qquad (B.12)$$

$$\eta_1\{g(t)\} = \eta_1\{g_1(t)\} + \eta_1\{g_2(t)\} \qquad (B.13)$$

$$\nu_2\{g(t)\} = \nu_2\{g_1(t)\} + \nu_2\{g_2(t)\} \qquad (B.14)$$

Equation (B.14) can be generalized by induction to give

$$\nu_j\{g(t)\} = \sum_k \nu_j\{g_k(t)\} \quad \text{for all k} \quad j=2,3,\ldots \,, \qquad (B.15)$$

if $g(p) = \prod_k g_k(p)$ Equations (B.5), (B.12) to (B.15) and the associative, commutative and distributive rules of linear operators establish the algebraic set of operations on linear operators and their moment expansions.

APPENDIX C

SOLUTION OF EQUATIONS (3.8) AND (3.9) WHEN
$$A(t) = A[\kappa(t) - \kappa(t-T)]$$

In general one can write

$$\int_0^t f(t-\lambda) \, [\, \kappa(\lambda) - \kappa(\lambda - T)] \, d\lambda = \int_{t-T}^t f(\lambda) \, d\lambda \qquad (C.1)$$

Applying (C.1) to Equations (3.8) and (3.9), one obtains

$$\frac{dN(t)}{dt} = \gamma nA \int_{t-T}^t \phi(\lambda) d\lambda \qquad (C.2)$$

$$\frac{dN(t)}{dx} = nA \int_{t-T}^t \rho(\lambda) \, d\lambda \qquad (C.3)$$

Substituting for $\phi(\lambda)$ and $\rho(\lambda)$ from Equations (3.8) and (3.9), and for the speed distribution f(s) from Equation (27), we can write

$$\frac{dN(t)}{dt} = \frac{\gamma nA}{\mu_o \{F_2(s)\}} \int_{t-T}^t s^3 \exp{-(s-S)^2} ds \qquad (C.4)$$

$$\frac{dN(t)}{dx} = \frac{nA}{\mu_o \{F_2(s)\}} \int_{t-T}^t s^2 \exp{-(s-S)^2} ds \qquad (C.5)$$

The integrals in Equations (C.4) and (C.5) are solved by introducing a change of variables y = s - S and integrating by parts, with the result

$$\frac{dN(t)}{dt} = \frac{\gamma nA}{\mu_o \{F_2(s)\}} \left\{ \frac{\exp{-(s-S)^2}}{2} [(s-S)^2 + 3S(s-S) + 3S^2 + 1] \right.$$

$$- \frac{\exp{-(\sigma-S)^2}}{2} [(\sigma-S)^2 + 3S(\sigma-S) + 3S^2 + 1]$$

$$\left. - \frac{\sqrt{\pi}}{2} (S^3 + 3/2 \, S) [\mathrm{erf}(s-S) - \mathrm{erf}(\sigma-S)] \right\} \qquad (C.6)$$

113

and

$$\frac{dN(t)}{dx} = \frac{nA}{\mu_o\{F_2(s)\}} \quad \frac{\exp-(s-S)^2}{2}(s-S) - \frac{\exp-(\sigma-S)^2}{2}(\sigma+S)$$

$$- \frac{\sqrt{\pi}}{2}(S^2+1/2)[erf(s-S) - erf(\sigma-S)] \qquad (C.7)$$

where

$$\sigma = \frac{L}{\gamma(t-T)} \qquad (C.8)$$

$$\mu_o\{F_2(s)\} \frac{\sqrt{\pi}}{2}(1 + erf\, S)(S^2+1/2) + \frac{S \exp(-S^2)}{2} \qquad (C.9)$$

In the case when

$$\frac{T}{t} \ll 1 \qquad (C.10)$$

and

$$T \ll \frac{\gamma^2 t^3}{2L^2} \quad \frac{1}{1 - S\gamma t/L} \qquad (C.11)$$

it is possible to show that Equations (C.6) and (C.7) reduce to

$$\frac{dN(t)}{dt} = \frac{\gamma nA}{\mu_o F_2(s)\}}(L/\gamma)^4(T/t^5)\exp-(L/\gamma t -S)^2$$

$$= \gamma nAT\phi(t) \qquad (C.12)$$

$$\frac{dN(t)}{dx} = \frac{nA}{\mu_o\{F_2(s)\}}(L/\gamma)^3(T/t^4)\exp-(L/\gamma t -S)^2$$

$$= nAT\rho(t) \qquad (C.13)$$

In the special case when $S \to 0$, Equations (C.6) and (C.7) become

$$\frac{dN(t)}{dt} = (2\gamma nA/\sqrt{\pi})\{(s^2+1)\exp(-s^2)$$

$$- (\sigma^2+1)\exp(-\sigma^2)\} \qquad (C.14)$$

$$\frac{dN(t)}{dx} = (2nA/\sqrt{\pi}\,)\left\{s\,\exp(-s^2) - \sigma\,\exp-(\sigma^2)\right\}$$

$$- nA\left\{erf(s) - erf(\sigma)\right\} \tag{C.15}$$

Note that $1/A\{dN(t)/dx\}$ represents the instantaneous density of the beam at a distance $L_{CD} = s\gamma t$ downstream of the chopper, while $1/A\{dN(t)/dt\}$ represents the instantaneous flux crossing a plane at L_{CD}.

Note also that Equations (C.12) and (C.13) are identical to the Equations (3.31) and (3.32) which were derived for an impulse gate function since in the case of a rectangular pulse

$$\mu_o\{A(t)\} = AT \tag{C.16}$$